

**FABRICATION AND CHARACTERIZATION OF GROUP IV ALLOY
SEMICONDUCTOR DEVICES**

by

Kenny Sangcheol Kim

A dissertation submitted to the Faculty of the University of Delaware in partial
fulfillment of the requirements for the degree of Doctor of Philosophy in Electrical
and Computer Engineering

Fall 2015

Copyright 2015 Kenny Sangcheol Kim
All Rights Reserved

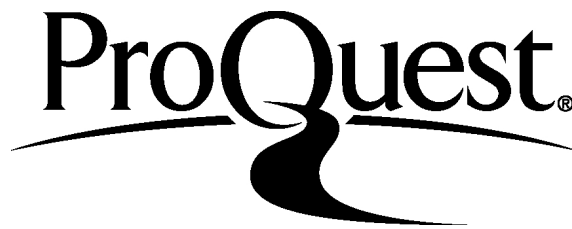
ProQuest Number: 10014752

All rights reserved

INFORMATION TO ALL USERS

The quality of this reproduction is dependent upon the quality of the copy submitted.

In the unlikely event that the author did not send a complete manuscript and there are missing pages, these will be noted. Also, if material had to be removed, a note will indicate the deletion.



ProQuest 10014752

Published by ProQuest LLC (2016). Copyright of the Dissertation is held by the Author.

All rights reserved.

This work is protected against unauthorized copying under Title 17, United States Code
Microform Edition © ProQuest LLC.

ProQuest LLC.
789 East Eisenhower Parkway
P.O. Box 1346
Ann Arbor, MI 48106 - 1346

**FABRICATION AND CHARACTERIZATION OF GROUP IV ALLOY
SEMICONDUCTOR DEVICES**

by

Kenny Sangcheol Kim

Approved: _____

Kenneth E. Barner, Ph.D.
Chair of the Department of Electrical Engineering

Approved: _____

Babatunde A. Ogunnaike, Ph.D.
Dean of the College of Engineering

Approved: _____

James G. Richards, Ph.D.
Vice Provost for Graduate and Professional Education

I certify that I have read this dissertation and that in my opinion it meets the academic and professional standard required by the University as a dissertation for the degree of Doctor of Philosophy.

Signed:

James S. Kolodzey, Ph.D.
Professor in charge of dissertation

I certify that I have read this dissertation and that in my opinion it meets the academic and professional standard required by the University as a dissertation for the degree of Doctor of Philosophy.

Signed:

Keith W. Goossen, Ph.D.
Member of dissertation committee

I certify that I have read this dissertation and that in my opinion it meets the academic and professional standard required by the University as a dissertation for the degree of Doctor of Philosophy.

Signed:

John Q. Xiao, Ph.D.
Member of dissertation committee

I certify that I have read this dissertation and that in my opinion it meets the academic and professional standard required by the University as a dissertation for the degree of Doctor of Philosophy.

Signed:

Fouad Kiamilev, Ph.D.
Member of dissertation committee

ACKNOWLEDGMENTS

I am extremely thankful to the many people who supported and assisted me through the course of my doctoral research.

Firstly, I would never have been able to finish my dissertation without the guidance of my advisor, Dr. James Kolodzey. I would like to express my deepest gratitude to him for his excellent guidance, caring, patience, and providing me with an excellent atmosphere for doing research. I would also like to thank my dissertation committee members, Dr. Keith Goossen, John Xiao, and Fouad Kiamilev, for their time, guidance and innumerable meaningful discussions during my doctoral research.

Secondly, I would like to thank my family for their immense support and patience. Their unconditional love and support motivated me at every point to pursue my dream of Ph.D. I would like to especially thank my parents, my wife, Jumryang Yoo, and my three kids for being there during the course of my entire research at University of Delaware.

I would like to thank my fellow graduate students for their assistance: Dr. Guangchi Xuan, Dr. Nupur Bhargava, Dr. Jay Gupta, Dr. Thomas Adam, Dr. Pengcheng Lv, Dr. Matthew Coppinger, Dr. Nathan Sustersic, Dr. Ralph Troeger, Xin Zhang, Dr. Xin Fan, Suddhasatwa Ghosh, Ramsey Hazbun, John LaRocco, Ranjan Santra and John Hart. I would like to extend my special thanks to Dr. Nupur Bhargava, and Dr. Jay Gupta during the final few months of my Ph.D. completion. I also thank Kjeld Krag Jensen for his help with clean room facilities, and thank Debbie

Whitesel, Kathy Forwood, Debbie Nelson, Karen Stefano and Wendy Scott, ,Heather Roscoe and Michele Jennings for all the help in the department.

This research was in part funded by AFOSR under grant number: FA9550-09-1-0688, Voltaix Corporation under grant number: 12A01464, Department of Energy under grant number DE-FG02-07ER46374 and gifts from IBM corporation, IR labs, and Voltaix Corporation

Kenny Sangcheol Kim

University of Delaware

Department of Electrical and Computer Engineering

140 Evans Hall, Newark, Delaware 19716

*This dissertation
is dedicated to
my loving parents, wife, Jamie, and children, Todd, Christine, and Paul*

TABLE OF CONTENTS

LIST OF TABLES	x
LIST OF FIGURES	xi
ABSTRACT	xvii

Chapter

1	INTRODUCTION AND MOTIVATION.....	1
1.1	Introduction	1
1.2	Growth and Device Characterization $\text{Ge}_{1-x}\text{Sn}_x$ Alloys.....	1
1.3	Novel Method of Reactive Ion Etching.....	3
1.4	Magnetic Tunnel Junction Based Phase Detection Device	3
1.5	Dissertation Summary	4
1.6	Publication from This Dissertation and Graduate Study.....	5
2	DEVICE CHARACTERIZATION AND FABRICATION METHODS	8
2.1	Introduction	8
2.2	Advanced Fourier Transform Infrared Spectroscopy Techniques	8
2.2.1	Michelson Interferometer	9
2.2.2	Interferogram	10
2.2.3	Beam Splitter and Detector Selection.....	13
2.2.4	High-Resolution FTIR Spectroscopy	14
2.3	Photocurrent Measurements of Detectors	15
2.3.1	Modifications for Photocurrent Measurements	15
2.4	Molecular Beam Epitaxy.....	18
2.5	MBE System for GeSn Growth.....	21
2.6	Substrate Materials Preparation.....	24
2.7	Source Materials Preparation	26
2.8	Substrate Loading and Growth Preparation	28
2.9	Device Fabrication.....	29

2.10	Current-Voltage Measurement	32
2.11	Rutherford Backscattering Spectrometry (RBS)	34
2.12	Secondary Ion Mass Spectrometry	36
3	GeSn HETEROJUNCTION DIODE	37
3.1	Introduction	37
3.2	GeSn Alloy Growth and Device Fabrication	37
3.2.1	Device Fabrication.....	45
3.3	Device Characterization	49
3.4	Conclusion.....	57
4	GeSn PHOTORESPONSE.....	58
4.1	Introduction	58
4.2	Experimental Detail	58
4.3	Results and Discussion	61
4.4	Conclusion.....	66
5	NOVEL METHOD OF REACTIVE ION ETCHING	67
5.1	Introduction	67
5.2	Plasma Etching	68
5.3	System Description: Plasma-Therm 790	70
5.4	Novel Reactive Ion Etching	73
5.4.1	Anisotropic Vertical Etching: Step 1.....	74
5.4.2	Isotropic Undercutting: Step 2.....	78
5.5	Conclusions	85
6	MAGNETIC TUNNEL JUNCTIONS	86
6.1	Introduction	86
6.2	Motivation	91
6.3	Device Fabrication.....	92
6.4	Conclusion.....	100

7	DETERMINATION OF SPECTRAL RESPONSIVITY OF GESN PHOTO DETECTORS USING FACTORY CALIBRATED GE AND DTGS REFERENCE DETECTORS.....	101
	7.1 Introduction	101
	7.2 Background.....	101
	7.3 Responsivity Calibration	102
	7.3.1 FTIR Set-up	102
	7.4 Conclusion.....	110
8	SUMMARY AND FUTURE WORK.....	111
	8.1 Summary.....	111
	8.2 Future Work.....	112
	REFERENCES	113
	Appendix	
	PERMISSION LETTERS	126

LIST OF TABLES

Table 2.1	Beamsplitter and Detector Operational Spectral Ranges for the ThermoNicolet Nexus 870.	14
Table 3.1	MBE Growth parameters of GeSn samples	45
Table 3.2	Extracted diodes parameters as derived	53
Table 5.1	Reactive ion etching parameters used to fabricate the microdisks in Figure 5.8. The anisotropic etching process of the left column produces vertical cylinders. The isotropic etching of the right column produces undercutting of the cylinders to create a microdisk. The insets show two subsequent processes(Step 1, and Step 2) to form the microcylinder and microdisk respectively.	84

LIST OF FIGURES

Figure 2.1	On the left: Michelson's interferometer. Light entering from the left side of the figure, is split by beamsplitter (B), reflected at fixed (m_F) and movable (m_M) mirrors and then exits downwards. On the right: Example of an interferogram – amplitude of signal versus the of mirror position	10
Figure 2.2	Schematic of the FTIR optical paths, based on a Michelson interferometer and its basic components such as an IR light source, parabolic mirrors, a beamsplitter, a fixed mirror, a moving mirror, and a detector.	12
Figure 2.3	Schematic diagram of Photocurrent measurement FTIR setup. The off-axis parabolic mirror focuses the radiation on the sample under test, which acts as a detector and is biased by a small reference voltage. Also shown in the figure is the radiation beam path to the sample with respective mirror positions. The radiation is chopped, amplified and sent to the FTIR electrical signal input port to obtain the interferogram. The whole setup is enclosed in a compartment and purged with N ₂ to avoid any water vapor absorption..	17
Figure 2.4	Schematic illustrations of the surface processes occurring during film growth in MBE	18
Figure 2.5	Schematic of MBD system used for GeSn alloy growth described in this chapter	22
Figure 2.6	Schematic diagram of an effusion cell. The source material is placed in a crucible which is heated by a filament. The chilled water cools the surfaces around the cell and process control are provided by a shutter and a thermocouple.....	23
Figure 2.7	Karl Suss MJB-3 Mask Aligner used for GeSn devices fabrication	31
Figure 2.8	The top image shows I-V measurement data, and bottom image shows the I-V measurement setup components such as Keithley 2400 source meter, alignment microscope and the Lab View interface.	33

Figure 3.1	Image of the MBE system at University of Delaware (DuPont 242) used to grow GeSn p-n junction diodes. The MBE system is located inside a Class 1000 clean room to avoid any external contamination and for maintaining good quality growth environment	39
Figure 3.2	SIMS measurement of 600 nm p-doped $\text{Ge}_{0.946}\text{Sn}_{0.054}$ /n-Ge [Courtesy Dr. T. Adams] showing profiles of B, P, Sn, Ge , C and O.	41
Figure 3.3	RBS random, aligned data along with the simulation of the random data which gave the Sn composition of 5.4%, showing good reduction in scattering yield for both Sn and Ge, which is an indication of high amount(>90%) of substitutional Sn	43
Figure 3.4	ω -2 θ XRD measurements of p-doped $\text{Ge}_{1-x}\text{Sn}_x$ /n-Ge with x varying from as 2.5%, 5.4% and 8%	46
Figure 3.5	An illustration of the individual steps involved in the photolithography process used to deposit the topside contacts. In numerical order, the steps involved: p-GeSn/n-Ge layer growth (step 2), photoresist spin (step 3), UV exposure (step 4) using the device mask (step 4), photoresist development (step 5).....	47
Figure 3.6	Top view of the device showing the Al meshes with two Au wire bonded	48
Figure 3.7	Dark current measurements of p-GeSn/n-Ge heterojunction diodes at room temperature. The inset shows I-V measurements of Samples with different Sn contents (A [9%], B [5.4%], C [2.4%], and D [0 %]).	50
Figure 3.8	The manipulated dark I-V characteristics for the p-GeSn/n-Ge heterojunction diodes (Sample A). (a) plot of the derivative dI/dV_a against V_a to obtain G; (b) plot of dV_a/dI_{corr} against $1/I_{\text{corr}}$ to obtain η and R_s	52
Figure 3.9	Current-voltage characteristics of the n-Ge/p-GeSn heterojunction at different temperatures for Sample A (9% Sn). Inset shows the Arrhenius Plot for the calculation of activation energy of the reverse saturation current (extracted from the diode equation)	55

Figure 3.10	Dark reverse biased current-voltage characteristics at various temperatures for Sample A. The breakdown voltage was about 1.75V at 297K, as indicated by the straight lines along the current branches.....	56
Figure 4.1	(a) Schematic of the experimental setup for photocurrent spectroscopy using an IR source (Globar) and optical chopper. The $\text{Ge}_{1-x}\text{Sn}_x$ device is held at temperature T on a cryostat. A lock-in amplifier and Thermo-Nicolet 870 FTIR were used to measure the spectral response. (b) Diagram of the $\text{Ge}_{1-x}\text{Sn}_x$ / n-Ge heterojunction device structure showing top and bottom metal contacts.....	60
Figure 4.2	Photocurrent response of a $\text{Ge}_{0.902}\text{Sn}_{0.098}$ / n-Ge heterojunction device at 100K (sample F, with 9.8%Sn): Increasing reverse-biased voltage resulted in larger amplitude of photocurrent that saturated at higher reverse voltages. The inset shows the dark current-voltage characteristics of several $\text{Ge}_{1-x}\text{Sn}_x$ devices with different Sn compositions.	63
Figure 4.3	Spectral photoresponse in mid-IR regime of $\text{Ge}_{1-x}\text{Sn}_x$ / n-Ge heterojunction devices, with different Sn compositions, at 100K. The response peaks lie at 0.619eV (sample G 12% Sn) , 0.681eV(sample F 9.8% Sn), 0.765eV(sample E 4% Sn), and 0.872eV(pure Ge sample H, 0% Sn) respectively.....	65
Figure 5.1	Basic RIE system, and typical parameters such as RF power, frequency, pressure, and etc.	69
Figure 5.2	Plasma-Therm 790 system used in this dissertation.....	71
Figure 5.3	Graphic User Interface (GUI) of Plasma-Therm 790 to control a process, showing a process chamber with pressure (here, less than 1mTorr), two green disks for two pumps of turbo, and mechanical rotary, and pumping lines of roughing, and foreline.	72
Figure 5.4	A depiction of the result of two major steps of our all-dry undercutting etching process. Step 1(anisotropic vertical etching) and Step 2(isotropic undercutting) to fabricate a microdisk. In Step 1, the perimeter of the upper disk structure was formed. A supporting pedestal was created by isotropic etching that removed substrate material under the disk in Step 2.....	75

Figure 5.5	A detailed depiction of cyclic dry reactive ion etching process to form a microdisk: (a) phosphorus doped bulk silicon (001) starting wafer, (b) A microcylinder formed in Step 1 using the three cyclic sub-steps of anisotropic, (c) In preparation for etching Step2, SiO ₂ was grown, (d) SiO ₂ is removed on bottom, and top by reactive ion etching (e) A supporting structure of pedestal was fabricated in Step 2. using isotropic undercutting etch. (f) A microdisk was formed	77
Figure 5.6	Isotropic silicon etch rate versus RF power for a gas mixture of 10sccm/20sccm; SF ₆ /He at a chamber pressure of 200mTorr. This condition was used during Step 2 of the undercutting process.	80
Figure 5.7	Silicon isotropic etch rate (μm/cycle), measured by the extent of undercutting versus pressure for a 10sccm/20sccm; SF ₆ /He with RF power of 50 Watts.	81
Figure 5.8	SEM micrographs of microdisks fabricated using novel method of reactive-ion etching process reported here. (a) shows cylinders: diameter: 150μm, and height: 15μm. In (b), the cylinders from (a) were undercut showing microdisk arrays	83
Figure 6.1	First observations of giant magnetoresistance. (a) On Fe/Cr(001) multilayers (Baibich 1988). (b) On Fe/Cr/Fe trilayers (Binash 1989). (c) Schematic of the mechanism of the GMR. In the parallel magnetic configuration (bottom), the electrons of one of the spin channels can go easily through all the magnetic layers and the short-circuit through this channel leads to a small resistance. In the antiparallel configuration (top), the electrons of each channel are slowed down every second magnetic layer and the resistance is high. The current is horizontal on the figure and it is carried by electrons having velocities in all the possible directions with different proportion of rightward and leftward orientations	87
Figure 6.2	Schematic of MTJ, which has a very thin insulating layer between ferromagnetic layers so that electrons can tunnel through quantum mechanically through the insulating barrier	88

Figure 6.3	Schematic of the TMR effect in an MTJ. During tunneling, electron spin orientation is preserved, i.e. an electron can only tunnel to the spin subband of the same spin orientation, and the conductance is proportional to the product of the Fermi level DOS values of the two electrodes of the same spin orientation. (a) shows parallel magnetization configuration, which means more tunneling conductance of electron. (b) shows antiparallel configuration for less tunneling conductance.....	90
Figure 6.4	(a) Experiment setup of the MTJ based microwave relative phase detection, showing test equipments of VNA, microwave splitter, function generator, phase shifter, lock-in amplifier, and MTJ device under test on CPWs. (b) Circuit for microwave phase detection. The MTJ is placed on the common short line of the two CPWs (left, and right CPW).....	93
Figure 6.5	(a) Relative phase dependence of the microwave induced voltage. (b) Two microwaves are fed into one structure, producing a response corresponding to the black curve in (a). (c) One microwave is fed into detection structure, while the other microwave is fed into an identical adjacent structure. In this case the microwave in the circuit is the same with the ones in (b). But the induced voltage response is only due to one of the microwave input, corresponding to the red and green curves in (a).	96
Figure 6.6	HFSS simulation of the surface magnetic field distribution of the structure used in the experiment. The microwave is fed in from the left side. At the common short, there is a non-uniform distribution of the microwave magnetic field.	98
Figure 7.1	Spectral response characteristics of various infrared detectors, indicating that the Pyroelectric detector shows flat response over wavelength from 1.5 μ m to 18 μ m [90].	103
Figure 7.2	Absolute spectral responsivity (A/W) of various detectors from Newport[91]. The pink line shows the absolute spectral responsivity of the Ge detector 818-IR, which is used in this calibration procedure. The inset shows the photograph of Newport Ge detector assembly with the active detector mounted in a black cylindrical holder, and a cable with DB-15 type electrical connector... ..	104

Figure 7.3	Schematic of the experimental setup for photocurrent spectroscopy using an infrared source (Globar) and an optical chopper. A lock-in amplifier and the Thermo-Nicolet 870 FTIR were used to measure the spectral response of the detector that is being tested.....	105
Figure 7.4	Extracted $T(\lambda)$ shows the range between 0.2~0.3. The inset shows $F_{\text{Ge-Factory}}(\lambda)$ in Eqn (1), which is the ratio of $M_{\text{Ge-Factory}}(\lambda)$ to $M_{\text{DTGS}}(\lambda)$	107
Figure 7.5	The responsivity of GeSn detector determined at the wavelength range of 1,250nm to 1,950nm. The inset (a) shows the ratio $M_{\text{GeSn}}(\lambda)$ to $M_{\text{DTGS}}(\lambda)$, and the inset (b) shows the responsivity of GeSn detector before considering the size of detector area.	109

ABSTRACT

The germanium-tin (GeSn) alloys comprise a non-equilibrium solid solution of two group IV elements. Their compatibility with integrated circuit processing makes them very useful for monolithic integration on silicon wafers. They have the important optical characteristic of an energy bandgap transition from indirect to direct in k-space with sufficient Sn content (above about 7 atomic % Sn). The Sn incorporation into Ge is limited, however, due to thermodynamic instability and also the difficulties of material growth. Nevertheless, non-equilibrium growth techniques have been used to prepare high quality GeSn alloys, which can be fabricated into optoelectronic devices. In this work, GeSn is grown up to 12% Sn by Molecular Beam Epitaxy, fabricated into devices using Clean Room processing, and characterized optically and electrically.

This dissertation presents work on the electrical and optical characterization of GeSn/Ge heterojunction devices. P-N heterojunction diodes were fabricated from layers of boron doped p-type GeSn grown by MBE on n-type Ge-substrates. GeSn pn diodes with varying Sn content were studied to extract diode electrical parameters. The Photoresponse of GeSn/n-Ge heterojunction devices was investigated with different Sn contents.

Electrical and optical devices sometimes use high profile structures including microdisks and resonators that are fabricated by methods such as deep etching. A simple fabrication method to achieve the deep undercutting required by microdisks by employing dry-processing reactive-ion etching (RIE) is investigated. The effects of key RIE parameters such as chamber pressure, and radio frequency (RF) power on the etch rates are reported for a

cyclic method that can achieve very deep structures. This cyclic RIE technique can be used for many materials such as Si, Ge, and GaAs, which would use a variety of different gas chemistries

The last section of this dissertation describes the fabrication and characterization of magnetic tunnel junction (MTJ) for microwave applications, which have been extensively investigated. In this work, a MTJ was designed, fabricated and tested for use as microwave phase detectors so that they can be used for microwave imaging, etc.

Chapter 1

INTRODUCTION AND MOTIVATION

1.1 Introduction

In this dissertation, work has been done on following projects: (1) fabrication and characterization of GeSn diode grown by Molecular Beam Epitaxy (MBE), (2) fabrication and characterization of GeSn photodetectors grown by MBE, (3) fabrication of Si-based micro-disks with all dry-etching technique, (4) fabrication and characterization of Magnetic Tunnel Junction (MTJ) devices. The MBE growths were performed by Dr. Nupur Bhargava in our group. The major portion of this dissertation describes the fabrication and device characterization of $\text{Ge}_{1-x}\text{Sn}_x$ alloys. The Silicon dry etching project was performed for P, and B-doped Si Terahertz emitters. The MTJ project was collaborative work with the Physics Department of University of Delaware (Prof. John Xiao's group). In the following sections, the main motivation behind the research work is discussed

1.2 Growth and Device Characterization $\text{Ge}_{1-x}\text{Sn}_x$ Alloys

Group IV based optoelectronic devices are very attractive because they can be easily incorporated with conventional Silicon based integrated circuits technology [1,2] Compared to Group III-V materials, however, Group IV materials have lower mobility and typically have a bandgap that is indirect in k-space which has been a limiting factor for optoelectronic application[3]. In recent years, $\text{Ge}_{1-x}\text{Sn}_x$ alloys have drawn lots of interest on their electrical and optical characteristics due to their possible direct bandgap crossover for sufficient Sn

about 7 atomic percent[4,5], the predicted higher carrier mobility [6], and an increase of lattice constant that enables strain engineering for Ge-based devices. Furthermore, GeSn alloys, which are compatible with group IV material processing, can be grown on Si wafers, enabling more applications with the monolithic integration of photonic devices.

Integrated silicon optoelectronic devices are useful for data communication in the near-IR wavelength (0.75–1.4 μ m) region, and their potential applications in the Mid-IR region (3–8 μ m) has gained research interests in the past few years. Recently, efficient optical emission devices [7-9] and photo detectors based on tensile-strained germanium have been reported [10, 11]. While alterations in the band structure of bulk Ge that mimic direct bandgap behavior can be induced through strain, the formation of a direct bandgap by composition through the alloying of group IV materials would be a method of band engineering that is compatible with the conventional materials processing techniques used in CMOS device fabrication.

Recently, there has been interest in the development of $\text{Ge}_{1-x}\text{Sn}_x$ alloys due to their predicted properties of indirect-to-direct band gap crossover at Sn contents near 6 % [1], and their compatibility with silicon technology [1, 2]. Recent interest in GeSn has motivated researchers to studies electrical and optical devices based on GeSn. The properties of p-i-n photodetectors as well as the infrared emission from GeSn diodes have been reported with up to 4% Sn content [15-18]. The electrical and optical characteristics of GeSn diodes need further investigation, however, with higher Sn contents as described in this dissertation.

In this study, we report the electrical and optical measurements of heterojunction diodes fabricated from epitaxial layers of boron doped p-type $\text{Ge}_{1-x}\text{Sn}_x$ grown by MBE on n-type Ge-substrates with up to 12% Sn, and some of their characteristics and limitations.

1.3 Novel Method of Reactive Ion Etching

For micro-electromechanical systems (MEMS) applications, the etching of silicon is required to relatively large depths (tens of microns) with high aspect ratios (depth of trench versus lateral opening). In this dissertation, a new all-dry processing method for the fabrication of suspended silicon micro-structures based on reactive ion etching is presented. This method was developed as an alternative to the combined dry, wet, and selective etching that was often used for undercutting structures such as cylinders to form microdisk resonators on pedestals. The goal of research is to report a simple fabrication method to achieve deep undercutting by employing dry-only reactive-ion etching (RIE), and report the effects of key RIE parameters such as chamber pressure, and radio frequency (RF) power.

1.4 Magnetic Tunnel Junction Based Phase Detection Device

Magnetic tunnel junctions (MTJs) are thin film spintronic devices which are composed of two ferromagnetic electrodes separated by a thin insulating barrier layer. When a voltage is applied across the top and bottom of this structure, classical physics does not allow a current to flow. If the insulating layer (also referred to as the “tunneling barrier layer”) is sufficiently thin, however, electrons can flow by quantum mechanical tunneling through it. Microwave detection devices using this magnetic tunnel junction (MTJ) have been extensively

investigated in recent years [20-24]. In this dissertation, a microwave phase detector using a MTJ, which is placed on a common short of two coplanar waveguides (CPW) is presented.

1.5 Dissertation Summary

The primary themes of this dissertation are the characterization of GeSn devices, the description of the novel silicon dry etching technique, and finally a presentation of the microwave phase detection device using MTJ.

Chapter 2 describes the methods to fabricate and characterize GeSn devices including Advanced Fourier Transform Infrared Spectroscopy techniques for measurement of optical properties of the devices, and Molecular Beam Epitaxy technique to grow GeSn devices.

Chapter 3 investigates the electrical properties of p-GeSn/n-Ge diodes with different Sn contents. Diode parameters are extracted from forward and reverse bias measurements over different Sn contents.

Chapter 4 reports the optical properties of GeSn/n-Ge heterojunction devices grown by MBE using electrical and photocurrent measurements.

Chapter 5 describes a novel simple all dry silicon etching methods using Reactive Ion Etching (RIE). This is an alternative method to the combined dry, wet, and selective etching that were typically required for undercutting structures to produce waveguides and microdisks, but with less cost, and simpler processing using the described technique.

Chapter 6 presents a novel phase detection device using the spintronic MTJ device principles.

Chapter 7 presents a method used to determine the spectral responsivity of the $\text{Ge}_{1-x}\text{Sn}_x$ / n-Ge heterojunction detector using a factory calibrated Ge detector and a DTGS pyroelectric detector with a flat spectral response is presented.

1.6 Publications from This Dissertation and Graduate Study

Below is the list of first author published papers:

- **Sangcheol Kim**, J. Gupta, N. Bhargava, M. Coppinger and James Kolodzey” Current-Voltage Characteristics of Ge/Sn Heterojunction Diodes Grown by Molecular Beam Epitaxy”, IEEE Elect. Dev. Lett., 34, 1217,(2013).
- **Sangcheol Kim**, N. Bhargava, J.P. Gupta, M. Coppinger, and James Kolodzey “Infrared photoresponse of GeSn/n-Ge heterojunctions grown by molecular beam epitaxy” , Optics Express, 22, 11029 -11034 (2014).

Below is the list of 2nd author published papers:

- Xin. Fan, **Sangcheol Kim**, Xiaoming. Kou, James Kolodzey, Huaiwu Zhang, and John Q. Xiao “Microwave phase detection with a magnetic tunnel junction” Appl. Phys. Lett, v. 97, 212501(2010).
- T.N. Adam, **Sangcheol Kim**, P. Lv, S.K. Ray, R.T. Troeger, D. Prather, and J. Kolodzey , “Cyclic deep reactive ion etching with mask replenishment,” J. of Micromechanics and Microengineering, v. 17, 1773-1780(2007) .

- G. Xuan, **Sangcheol Kim**, M. Coppinger, N. Sustersic, J. Kolodzey, and P.-C Lv, "Increasing the operating temperature of boron doped silicon terahertz electroluminescence devices," Appl. Phys. Lett, v. 91, 061109(2007).

And other papers as a co-author below:

- P.-C. Lv, R.T. Troeger, T.N. Adam, **Sangcheol Kim**, J. Kolodzey, I. N. Yassievich, M. A. Odnoblyudov, and M. S. Kagan, "Electroluminescence at 7 terahertz from phosphorus donors in silicon," Appl. Phys. Lett., v. 85 (1),22-24a(2004) .
- P.-C. Lv, R.T. Troeger, **Sangcheol Kim**, S.K. Ray, K.W. Goossen, and J. Kolodzey, I. N. Yassievich, M. A. Odnoblyudov, and M. S. Kagan, "Terahertz emission from electrically pumped gallium doped silicon devices," Appl. Phys. Lett., v. 85 (17), 3660-3662(2004).
- R. T. Troeger, T.N. Adam, S.K, Ray, P.-C. Lv, **Sangcheol Kim**, and J. Kolodzey, "Temperature dependence of terahertz emission from silicon devices doped with boron," International Journal of High Speed Electronics and Systems, v.14, No. 3, 670-675(2004).
- L.R. Shah, N. Bhargava, **Sangcheol Kim**, R. Stearrett, X. Kou, X. Sun, S. Sun, J. Kolodzey, E.R. Nowak, and J.Q. Xiao, "Magnetic tunneling junction based magnetic field sensors: Role of shape anisotropy versus free layer thickness," J. Appl. Phys., v. 109, 07C731(2011).
- M. Coppinger, J. Hart, N. Bhargava, **Sangcheol Kim**, and J. Kolodzey, "Photoconductivity of germanium tin alloys grown by molecular beam epitaxy," Appl. Phys. Lett., v. 102 (14), 141101(2013) .

- J.P. Gupta, N. Bhargava, **Sangcheol Kim**, T.N. Adam, and J. Kolodzey, “Infrared electroluminescence from GeSn heterojunction diodes grown by molecular beam epitaxy,” Appl. Phys. Lett., v. 102 (25), 251117(2013).

Chapter 2

DEVICE CHARACTERIZATION AND FABRICATION METHODS

2.1 Introduction

This chapter describes the fabrication techniques and various characterization methods used for the optoelectronic and spintronic devices described in this dissertation. The Fourier Transform Infrared (FTIR) Spectrometry technique used for photocurrent measurement on GeSn devices is explained, and the Molecular Beam Epitaxy technique used for GeSn growth is described. Lastly some other device measurement techniques such as Current-Voltage characterization, alloy concentration measurement techniques of Secondary Ion Mass Spectrometry (SIMS), Rutherford Back Scattering (RBS), and fabrication techniques such as photolithography are presented in later sections.

2.2 Advanced Fourier Transform Infrared Spectroscopy Techniques

Fourier Transform Infrared (FTIR) Spectrometry is a technique extensively used to measure transmission, absorption, reflection, and emission spectra in many different applications. Especially FTIR has been the essential technique in finding various information of materials such as semiconductors, organic, and inorganic solids. In this dissertation, the ThermoNicolet Nexus 870[25] FTIR spectrometer was used to characterize the devices. FTIR principles, advanced measurement techniques are explained in below sections

2.2.1 Michelson Interferometer

An interferometer is a device that introduces an optical path between two beams that are coming from the same source. A Fourier Transform Spectrometer is based on this interferometer, where the incident light is divided into two beams by a beamsplitter, creating an optical path difference causing the two beams to interfere when they combine later generating an interferogram as shown in Fig. 2.1. The Most common type of Fourier-Transform spectrometer is based on Michelson's interferometer as shown in Fig. 2.1. Incoming light from the source is partly transmitted and partly reflected by the beamsplitter.

As shown in Fig. 2.2 of FTIR, a radiation source is first collimated by a parabolic mirror, and then the collimated beam travels to the beamsplitter, where the beam is separated into two beams path, one is transmitted to a moving mirror, and the other is reflected to a fixed mirror. Light is reflected back from the respective mirrors, and eventually interfere at the beamsplitter. The detector measures the variation in beam intensity as a function of the optical path difference. The signal measured is called interferogram which has the unique property that every data point (a function of the moving mirror position) which makes up the signal has information about every infrared frequency which comes from the source. In order to obtain a frequency spectrum, a mathematical technique of the Fourier transformation is required.

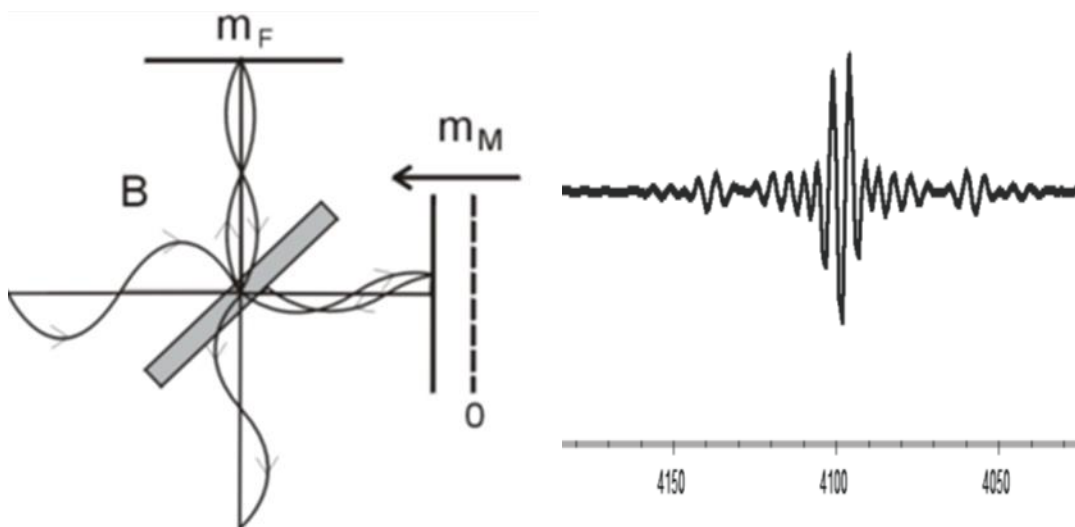


Figure 2.1: On the left: Michelson's interferometer. Light entering from the left side of the figure, is split by beamsplitter (**B**), reflected at fixed (m_F) and movable (m_M) mirrors and then exits downwards. On the right: Example of an interferogram – amplitude of signal versus the of mirror position

2.2.2 Interferogram

In order to understand the spectrometric measurements in an ideal FTIR using the notation of Griffiths and de Hasleth[26], the intensity at the detector as a function of optical path difference, δ , can be written for a monochromatic source with wavelength of radiation, λ (wavenumber: ν ($1/\lambda$)) as:

$$I(\delta) = \frac{1}{2} I_0(v)(1 + \cos(2\pi v\delta)) \quad (2.1)$$

where I_0 is the intensity of the monochromatic source. For a perfect monochromatic light source, the recombined beams will produce some interference, which can be constructive or destructive depending on the optical path differences as in equation 2.1. As the mirror moves and δ changes, Equation 2.1 contains both a modulated (AC) component and a constant (DC) component. When the DC component of Equation 2.1 is removed, the remaining modulated component for a monochromatic source can be expressed as,

$$I(\delta) = \frac{1}{2} I_0(v) \cos(2\pi v\delta) \quad (2.2)$$

where $I(\delta)$ is the interferogram.

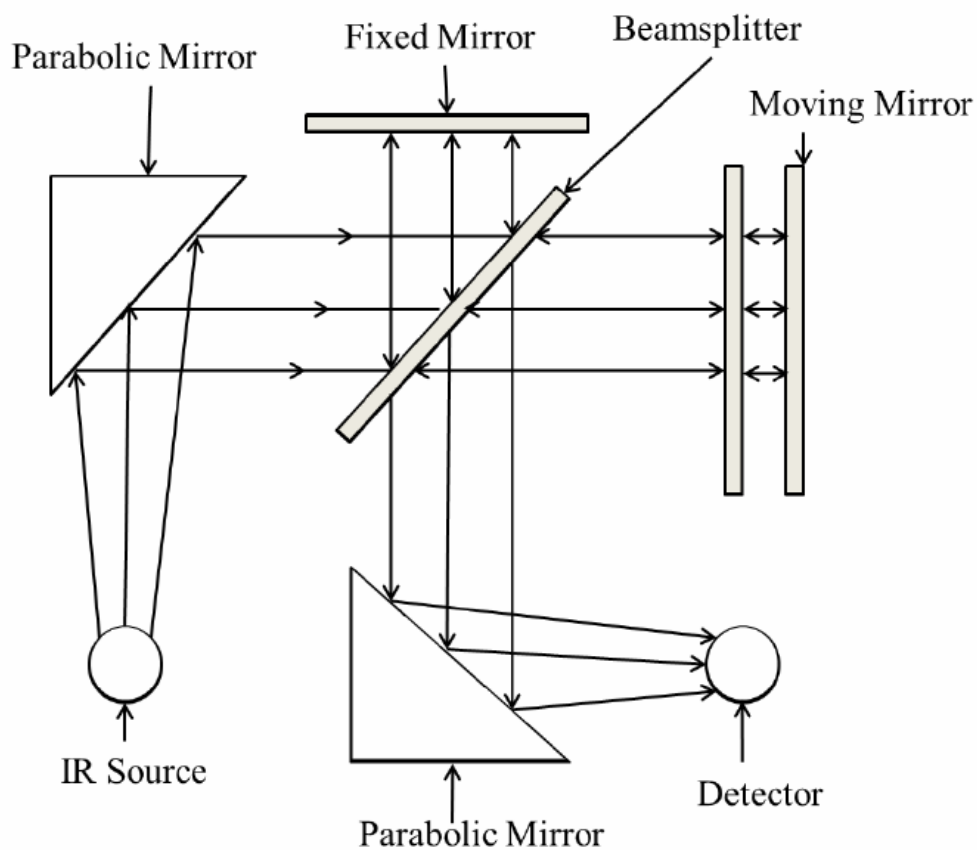


Figure 2.2: Schematic of the FTIR optical paths, based on a Michelson interferometer and its basic components such as an IR light source, parabolic mirrors, a beamsplitter, a fixed mirror, a moving mirror, and a detector.

During practical spectrometry, some variations from ideal conditions should be considered such as detector response, the beamsplitter efficiency, etc. Therefore, we can define a wavenumber dependent correction factor, $B(\nu)$ to describe the spectral intensity as following equation:

$$I(\delta) = B(\nu) \cos(2\pi\nu\delta) \quad (2.3)$$

where the interferogram, $I(\delta)$, is the cosine Fourier transform of the spectral intensity, $B(\nu)$. If we expand this to a broadband source from monochrome source,

$$I(\delta) = \int_{-\infty}^{+\infty} B(\nu) \cos(2\pi\nu\delta) d\nu \quad (2.4)$$

where the interferogram, $I(\delta)$, is now taken as an integral over all wavenumbers. However, in practice the spectral data that can be obtainable are limited due to the beamsplitter, the source, and the detector's limited capability to cover the range.

2.2.3 Beam Splitter and Detector Selection

The Thermo Nicolet Nexus 870, the FTIR model used in this dissertation, is equipped with four detectors, three beamsplitters, and two broadband sources that allow the operation at wavenumber ($1/\lambda$) from 10 cm^{-1} to $32,000 \text{ cm}^{-1}$. The first broadband source, a Globar is a silicon carbide infrared heated resistor that mimics the spectral emittance of an 1140°C

blackbody source [27]. The useful wavenumber range for this source is from 9000 cm^{-1} to 20 cm^{-1} . A white light source, heated Tungsten-Halogen filament is used for wavenumbers above 9000 cm^{-1} , and with a blue filter this source can be extended to record data up to 32,000 cm^{-1} .

The operational spectral ranges for compatible beamsplitter and detector combinations are listed in Table 2.1. A quartz beamsplitter was used for visible and near IR measurements while potassium bromide (KBr) and silicon beamsplitters were used for mid-wavelength IR and far IR measurements, respectively. Detectors included silicon and indium gallium arsenide (InGaAs) photodiodes, a thermoelectrically cooled (TEC) deuterated triglycine sulfate (DTGS) pyro-electric detector, a DTGS pyro-electric detector with a polyethylene (PE) window. To achieve maximum signal to noise ratio, suitable detector/beamsplitter combination have to be used for the wavelength range of interest.

Table 2.1: Beamsplitter and Detector Operational Spectral Ranges for the ThermoNicolet Nexus

Beamsplitter	Detector	Spectral Range (cm^{-1})	Wavelength (μm)
Quartz	Silicon	32,000 – 8,600	0.313 – 1.16
	InGaAs	12,000 – 3,800	0.833 – 2.63
	DTGS TEC	7,400 – 2,800	1.35 – 3.57
KBr	InGaAs	11,000 – 3,800	0.909 – 2.63
	DTGS TEC	11,000 – 350	0.909 – 28.57
Silicon	DTGS PE	600 – 150	16.67 – 66.67
	Silicon Bolometer	600 – 20	16.67 – 500

2.2.4 High-Resolution FTIR Spectroscopy

Compared to a conventional grating spectrometer technique, there are two advantages of FTIR spectrometers. First, spectral information from every frequency is recorded

simultaneously. This multiplexing ability, known as Fellgett's advantage, suggests that the signal-to-noise ratio (SNR) for identical spectra measured on an FTIR spectrometer exceeds that of a grating spectrometer. Second, Jacquinot's advantage describes the increase in SNR obtained from the optical throughput of the FTIR in comparison to a grating spectrometer. If the system optics are not changed for identical measurements using a grating spectrometer and an FTIR, according to Jacquinot's advantage the SNR ratio for the FTIR increases with the square of the measured wavenumber. The combination of Fellgett's and Jacquinot's advantages indicates that the theoretical sensitivity of an FTIR taking measurements at a resolution of 4cm^{-1} can be 2000 times greater than that of a grating spectrometer.

The FTIR spectral data recorded for this dissertation were obtained via the application of a fast Fourier transform (FFT) to the interferogram from the interferometric measurements.

2.3 Photocurrent Measurements of Detectors

For thin films, photocurrent spectroscopy is a useful technique for identifying spectral absorption characteristics that are too faint to see using reflection and transmission spectroscopy. Following sections explain the methods to measure photocurrent used in this dissertation

2.3.1 Modifications for Photocurrent Measurements

For photocurrent measurement, the device under test is used as the FTIR detector. The Nexus 870 FTIR has a built-in detection port, capable of directing the combined Interfered(IR) light from the beamsplitter to a path outside the FTIR mainframe unit. The schematic of the FTIR for photocurrent measurements is shown in Fig. 2.3. An off-axis parabolic mirror is

used to focus light onto the sample, which is placed in a vacuum closed-loop He cryostat (ARS, Inc. DE-204SF) for cryogenic cooling (excluding the mirror and chopper). The cryostat was equipped with a low-vibration bellows to isolate the samples and FTIR components from external motion. To allow operation at cryogenic temperatures, the cryostat was evacuated to sub-millitorr pressures using a molecular drag pump. The samples under test are electrically biased with a small voltage to produce a photocurrent. The FTIR internal source (globar) radiation, as shown in Fig. 2.3 is directed with the help of an off-axis parabolic mirror to fall directly on the sample under test. The incident source radiation may cause some of the confined carriers to be lifted from a ground state to a conduction continuum or to higher levels or generate electron-hole pairs by interband absorption; resulting in a change in photocurrent. The resulting current is amplified by a low- noise amplifier and returned to the external input of the FTIR to obtain the interferogram. The interferogram is Fourier transformed by computer software performing a fast Fourier transform to obtain the photocurrent spectra that contains the response specific to the materials properties of the device under test. Because of a very small change in the observed photocurrent due to the impinging radiation, the step scan technique has been most suitable for photocurrent measurements, to remove any ambient background interference and to improve the signal to noise ratio. To eliminate any contribution of the ambient background of light, electrical pickups, mechanical vibration, etc. an optomechanical chopper was placed in the beam path to produce an ac signal that can be synchronously detected by a lock-in amplifier, and the data were recorded in step scan mode. To ensure that atmospheric attenuation would not adversely affect any measurements, a nitrogen purge with a pressure regulator set at 30 standard cubic feet per hour was installed for

the sample compartment shown in Fig. 2.3 to remove moisture and CO₂ that can absorb in the infrared.

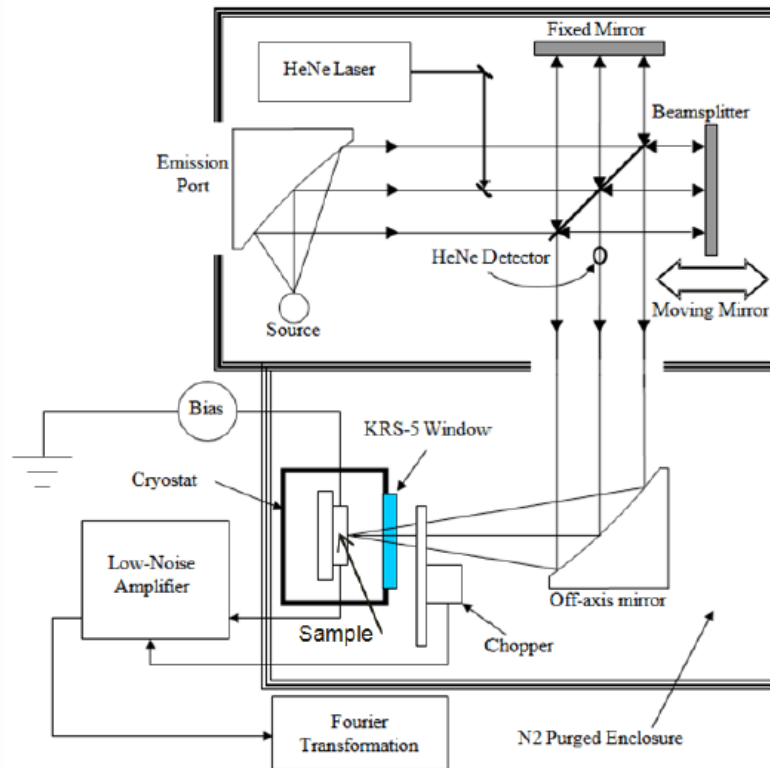


Figure 2.3: Schematic diagram of Photocurrent measurement FTIR setup. The off-axis parabolic mirror focuses the radiation on the sample under test, which acts as a detector and is biased by a small reference voltage. Also shown in the figure is the radiation beam path to the sample with respective mirror positions. The radiation is chopped, amplified and sent to the FTIR electrical signal input port to obtain the interferogram. The whole setup is enclosed in a compartment and purged with N₂ to avoid any water vapor absorption.

2.4 Molecular Beam Epitaxy

For the growth of epitaxial layers of material, Molecular Beam Epitaxy (MBE) has been a versatile technique due to its great precision and purity. It is characterized by a low growth rate, and has the capability to grow a single atomic layer of material. The primary advantage is to form high-quality epitaxial layers of material with precise control over chemical composition, thickness, and doping concentrations [29]. The epitaxial growth of MBE is achieved by the impingement of the constituent molecular or atomic beams onto a heated substrate in an ultra-high vacuum (UHV) chamber. Fig. 2.4 shows a schematic illustration of the processes occurring during film growth in a typical MBE system.

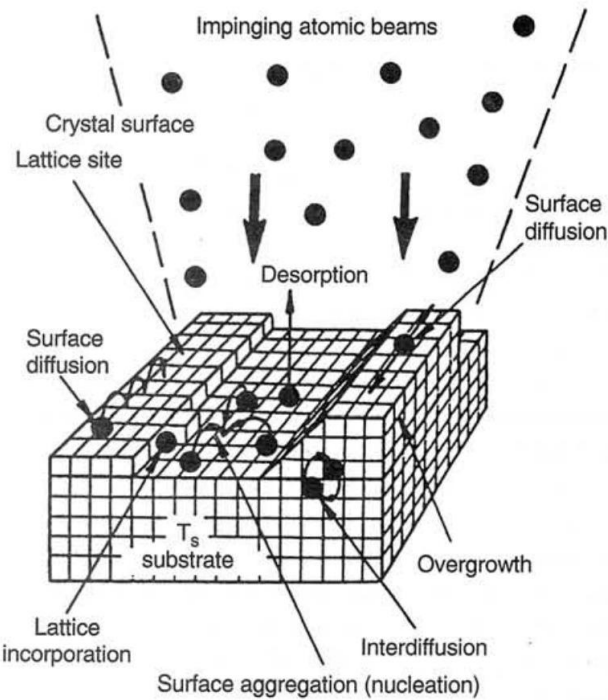


Figure 2.4: Schematic illustrations of the surface processes occurring during film growth in MBE[30]

A heated substrate can serve as a seed crystal, while constituent molecular or atomic beams impinge on the surface, therefore the temperature of the substrate is a source of the kinetic energy to the molecular or atomic beams for both dissociation and surface migration to suitable growth sites.

During the MBE film growth, both chemical and physical processes occur on the surface. The most important processes for epitaxial growth are adsorption of the impinging atoms or molecules, surface migration and dissociation of adsorbed molecules, incorporations of constituent atoms at step edges, and thermal desorption of excess species [31]. The kinetic energy supplied by the substrate temperature mainly controls those growth processes rates.

There are two types of adsorption in the growth of MBE, physical adsorption and chemical adsorption. For physical adsorption, also called physisorption, the van der Waals forces bind the adatom or molecule to the surface without any electron transfer between the adsorbate and the surface. This adsorption is accompanied by the surface migration of the adsorbate strongly. The other type of adsorption, which is chemisorption, involves a chemical reaction between the adsorbate and the surface, with electron transfer, which is leading to the formation of chemical bonds.

MBE is an ultrahigh vacuum process. The typical growth pressure for MBE is 10^{-10} Torr. At such a low pressure, fewer collisions occur due to the mean free path of the molecule being quite large. The thermal source provides molecules with thermal energy to propagate to the substrate. Due to fewer or negligible molecular collision, these molecules do not scatter. Hence they form a molecular or atomic beam which is incident on the substrate. These molecules adsorb onto the crystalline surface and they stay on the surface and reposition to

lattice sites due the energy provided by the heated substrate and form an epitaxial film. Before forming the film, these molecules make a large number of site changes. Due to the low pressure, MBE can be governed by this kinetics of the surface processes. The mean free path of a molecule (L) is inversely proportional to the pressure (p) and directly proportional to the temperature (T).

$$L = \frac{1}{\sqrt{2}\pi d^2} \quad (2.6)$$

$$n = \frac{p}{k_B T} \quad (2.7)$$

where d is the molecular diameter, n is the concentration of gas molecules and k_B is the Boltzmann constant[32].

On the crystal surface, these atoms/molecules become incorporated into a lattice after a characteristic dwell time. The characteristic surface diffusion length l_s and the thermally activated surface diffusivity D_s are related as follows:

$$l_s = \sqrt{2D_s\tau_s} \quad (2.8)$$

$$D_s = D_0 \exp\left(\frac{-E_D}{k_B T}\right) \quad (2.9)$$

where τ_s is the mean residence time of adatoms on the surface and E_D is the energy barrier of site interchange. τ_s can be approximated to be the time for atom to find the lattice site.

The above kinetic relationships help in growing metastable epitaxial structures. Large D_s gives adatoms enough energy to attain a thermodynamically stable structure [32, 33]. Whereas small D_s can allow kinetic stabilization of a nonequilibrium configuration. MBE is a non-equilibrium process and hence can synthesize alloys which are not in equilibrium state [34]. The non-equilibrium state is achieved by lowering the growth temperatures.

The low pressure (in the growth chamber) helps to reduce the impurity incorporation in the film (such as H₂O vapor, O₂, and CO), grow films as thin as a few monolayers and also make doping profiles and interfaces abrupt. If the partial pressure of residual gases is several orders of magnitude lower than the vapor pressure of the source (material to be grown) molecules, a high purity epitaxial film is formed.

2.5 MBE System for GeSn Growth

Figure 2.5 shows a schematic diagram of the custom EPI-620 MBE system used for GeSn alloys growth. The system has two chambers, a growth chamber and a sample introduction chamber separated by a pneumatically activated gate valve. The sample is being transferred between the two chambers with a magnetically coupled sample transfer rod.

In order to generate molecular or atomic beams from each constituent element, the EPI-620 system utilizes effusion cells with pneumatically controlled shutters. The effusion cell contains a crucible made of pyrolytic boron nitride (pBN), heating filaments, and water cooling system, heat shields and orifice shutter shown in Figure 2.6.

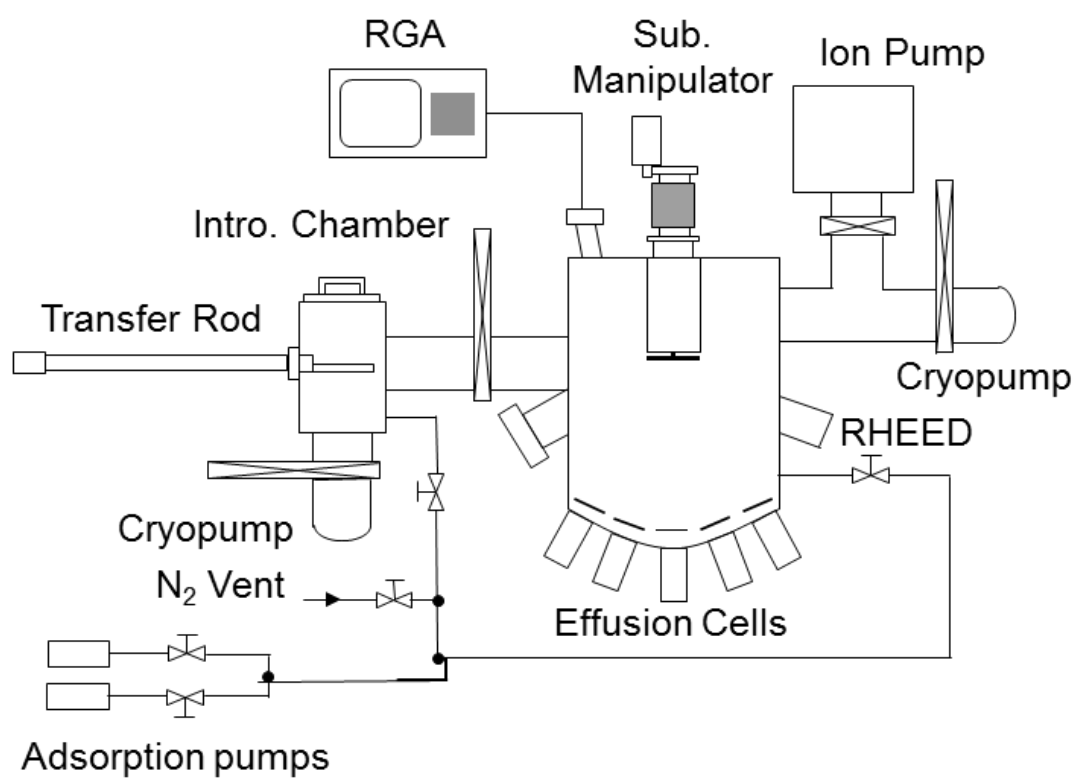


Figure 2.5: Schematic of MBD system used for GeSn alloy growth described in this chapter.

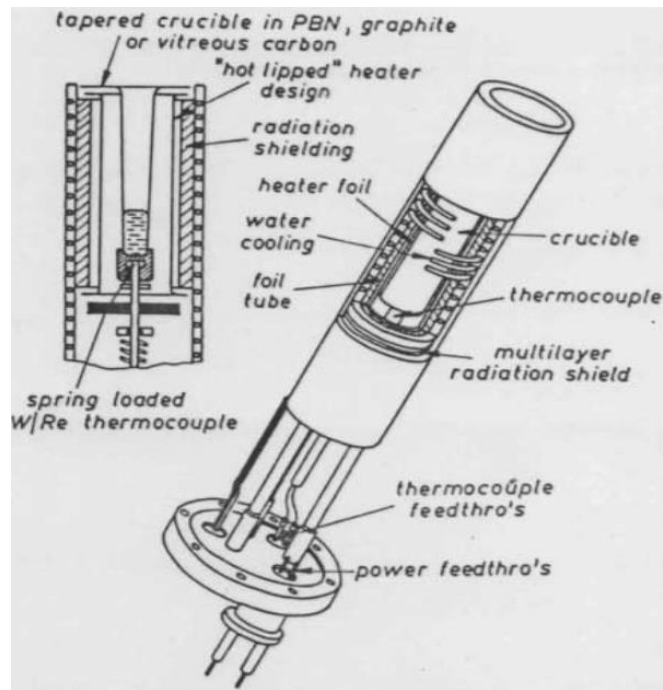


Figure 2.6: Schematic diagram of an effusion cell. The source material is placed in a crucible which is heated by a filament. The chilled water cools the surfaces around the cell and process control are provided by a shutter and a thermocouple [35]

The effusion cells are the source of the molecular beams and are each typically heated independently from resistive heating wire. By varying the cell temperature, the vapor pressure can be controlled such that the proper variations in growth rate and composition are achieved. All the molecular beams from the each effusion cell are controlled by pneumatically actuated linear motion shutters so that the molecular beams can reach the substrate only when shuttered are opened. A detailed description of the EPI 620 MBE system, its components, control software and safety interlocks can be found in Brad Orner's Master's thesis and Ph.D. dissertation [34].

For n-type doping of the GeSn alloys, a custom effusion cell for phosphorus evaporation from a solid source of GaP having a pBN crucible is used. GaP is heated above 670 °C so that GaP is decomposed, P is evaporated, and Ga is trapped by a PNB baffle screen. For p-type doping, a boron effusion cell with a pyrolytic graphite (PG) crucible with a tungsten liner was used. Due to boron's low vapor pressure, the cell was heated to very high temperature (~ 1500°C).

2.6 Substrate Materials Preparation

The Ge substrate wafers were prepared for epitaxy by following procedure [36].

- (1) DI water rinse under running DI water
- (2) Methanol rinse to remove DI water left on substrate after the DI rinse
- (3) Solvent cleaning (in Pyrex beakers)
 - Boil in TCE(Trichloroethylene) for 5 minutes
 - Boil in Acetone for 5 minutes

- DI water rinse (submerging in fresh DI water in a cleaned beaker)

(4) Particulate removal (in Pyrex beakers)

- Boil in H_2O : FL-70(Detergent) with a ratio of 1:12 for 10 minutes
- DI water rinse twice
- DI water rinse boiled for 10 minutes.
- DI water rinse twice
- Keep the Ge substrate in DI water of a quartz beaker

(5) Oxidation and Etch

- Dip in HF: H_2O with a ratio of 1:10 for 10 seconds (in Teflon beaker)
- DI water rinse under running DI water
- Dip in H_2O_2 : H_2O with a ratio of 1:10 for 15 seconds (in Quartz beaker)
- Running DI water rinse
- Repeat above HF: H_2O / H_2O_2 : H_2O steps 4 times
- DI water rinse
- Dip in HF: H_2O with a ratio of 1:10 for 10 seconds (in new solution)
- Dip in H_2O_2 : H_2O with a ratio of 1:10 for 15 seconds(in new solution)
- Running DI water rinse
- DI water rinse
- Blow dry with N_2 till no water droplet on the substrate

2.7 Source Materials Preparation

In order to grow $\text{Ge}_{1-x}\text{Sn}_x$ alloys, Ge and Sn source materials were prepared and installed in the crucibles of EPI-620 MBE system. Before inserting the source materials, Pyrolytic Boron Nitride (pBN) crucibles were typically chemically cleaned and blow-dried. For the outgassing of PBN crucibles, the temperature is increased to 1500°C where it is held for a couple of minutes to prevent decomposition. The crucible is then cooled down to 1400°C where it is held for one hour for outgassing, and then is cooled to 1200°C for outgassing overnight. The crucible is cooled to room temperature before the charging the source material.

Following are the procedure to clean Ge and Sn source

Ge source

- Degrease Ge source materials by boiling in the following solvents in Pyrex beakers
 - Trichloroethylene for 5 minutes
 - Acetone for 5 minutes
 - Methanol for 5 minutes
- Etch charge material in HNA solution for 5 minutes: $\text{HF}:\text{HNO}_3:\text{CH}_3\text{COOH}$ solution with ratio of 1:15:5 (etch rate $\sim 5 \mu\text{m}/\text{min}$). This etch removed several microns ($\sim 25 \mu\text{m}$) of source material.
- Dip in 10% HF solution, to remove residual oxide.
- Etch in a second HNA solution for 3 minutes, ratio of 5:15:7 with higher etch rate
- Dip in 10% HF solution
- Blow dry with N_2

Sn source

- Sn granules in Teflon basket.
- Rinse with DI water, in a Pyrex beaker
- 20 seconds DI water rinse (running DI water)
- Degrease by boiling in solvents in Pyrex beaker:
 - Trichloroethylene for 5 minutes
 - Acetone for 5 minutes
 - Methanol for 5 minutes
- Transfer Sn granules to a DI water filled quartz beaker
- Turn on heater of ultrasonic bath and fill with water
- Etch Sn granules in a quartz beaker with etchant solution – HCl(32%):Methanol with a ratio 1:24
- Place beaker in ultrasonic bath for 3 minutes.
- 20 seconds DI water rinse (running DI water)
- DI water rinse in Pyrex beaker
- Dry source material with filtered high purity N₂ gas flow

The cleaned Sn granules were placed in a pBN crucible and then loaded in to the MBE growth chamber. The growth chamber was rough pumped to 10^{-4} Torr using the two sorption pumps, and then pumped using the cryopump. At pressure of 10^{-9} Torr, the gate valve between ion pump and the growth chamber was opened. The temperature of the Sn effusion cell was increased at increments of 25°C, pausing at each temperature for 15 min, to a temperature of 200°C. At 200°C, the Sn source was outgassed for 12 hours. To melt the Sn source material

($T_m = 232^\circ\text{C}$) , the temperature of Sn effusion cell was increased from 200°C to 250°C in increments of 3°C and then to 300°C in increments of 10°C , pausing at each step for 15 min. The abovementioned gradual outgassing ensured no residual impurities were incorporated in the Sn source [37]. The pBN is performed with maximum outgassing temperature for Ge = 1300°C , for Sn = 950°C , for GaP = 825°C and B = 1850°C .

2.8 Substrate Loading and Epitaxial Growth

The Ge substrate is loaded immediately into the introduction chamber of the EPI-620 MBE system right after the wafer preparation step. During the Ge substrate loading, the introduction chamber is purged with N_2 . After loading the substrate, the introduction chamber is pumped by the sorption pumps to below 1×10^{-4} Torr, then the cryopump gate valve is opened and the pressure of the introduction chamber is cryo-pumped overnight to less than 10^{-8} torr. When the load chamber pressure is sufficiently low, the substrate is transferred into the main growth chamber.

The outgassing procedure at elevated temperatures for the Ge substrate is described as following. First, Ge substrate is heated to 150°C and outgassed for 15 minutes, and the substrate is then heated to 200°C and to 350°C and held for 15 minutes at each temperature. In order to desorb the Ge oxides formed during the last step of the Ge substrate preparation described in the previous section, the substrate is heated to 530°C . The RHEED pattern is checked to confirm the (2x1) surface reconstruction for (100) Ge substrates.

As performed by Dr. Nupur Bhargava from our group, following epitaxial growth was prepared[82]. The vapor pressure of the source materials defines the flux of the evaporant

species arriving the substrate [32]. Growth rates were calibrated by ex-situ characterization techniques. To calibrate growth rates, SiGe samples on Si (100) substrates and GeSn samples on Ge (100) substrates were grown. Using X-ray diffraction, concentration of Ge in SiGe samples was determined. From which the Si and Ge growth rates were extracted. Thickness of GeSn alloys was also determined using X-Ray and stylus profilometry. Knowing the growth rate of Ge, the growth rate of Sn was calculated. RBS measurements were used to determine the composition of Sn in GeSn alloys.

Calibration samples consisted of various Ge and Sn cell temperatures and various Si e-beam emission currents. The samples were of high epitaxial quality. These samples were characterized with X-ray diffraction. ω -2 Θ rocking curves were scanned for (004) reflection of the Si and Ge substrate. From the growth rate of Ge and the thickness of GeSn alloys (from interference fringes in the ω -2 Θ rocking curve) and the Sn cell temperature, the Sn growth rate was calculated. The Sn growth rate was found to be 0.80 Å/min at the Sn effusion cell temperature of 950°C. And boron dopant flux and phosphorous dopant flux were also obtained for p-type and n-type doping respectively [82].

2.9 Device Fabrication

In order to fabricate optoelectronics device such as IR emitters and detectors from the MBE grown GeSn alloy, standard photolithography was used. The samples were cleaned using rinsing in a series of solvents: Acetone, Methanol, and Isopropanol, 30 seconds each, to remove any oil residue or fine particles. The wafers were then blown dry with N₂. Next, a 2 μm film of negative resist (Futurrex NR7-1500PY) was applied to the wafer by spin coating at

3000 rpm for 40 seconds, and the wafer was soft-baked at 150 °C for 60 seconds. The individual wafer was then loaded into the mask aligner (Karl Suss MJB-3, Fig. 2.7), where the pattern was transferred into the photoresist in contact with the custom topside mask plate with 365 nm UV light for about 10 -13 seconds. The photoresist is post baked at 100 °C for 60 seconds. After exposure the resist is developed using developer (Futurrex, Inc. RD6) for 10 - 12 seconds. After photoresist development, the wafers were loaded into a dual e-beam source, high-vacuum metal evaporator. 3000 Å of Al was deposited using an e-beam source to form the metal contact of the GeSn P-N junction. A metal deposition of Ti/Au (30/300 nm) was performed to form the bottom contact. Finally, metalized wafers were diced into chips with top surface areas of 2 x 2 mm² and 1 x 1mm² prior to electrical measurements. Au wires were bonded on top of the Aluminum electrodes. In order to electrically isolate the samples, insulating epoxy was used to affix the samples to a copper heat sink mount. Samples were then cooled using a closed-loop liquid He cryostat (ARS, Inc. DE-204SF) equipped with a thallium bromide-iodide (KRS-5) optical window

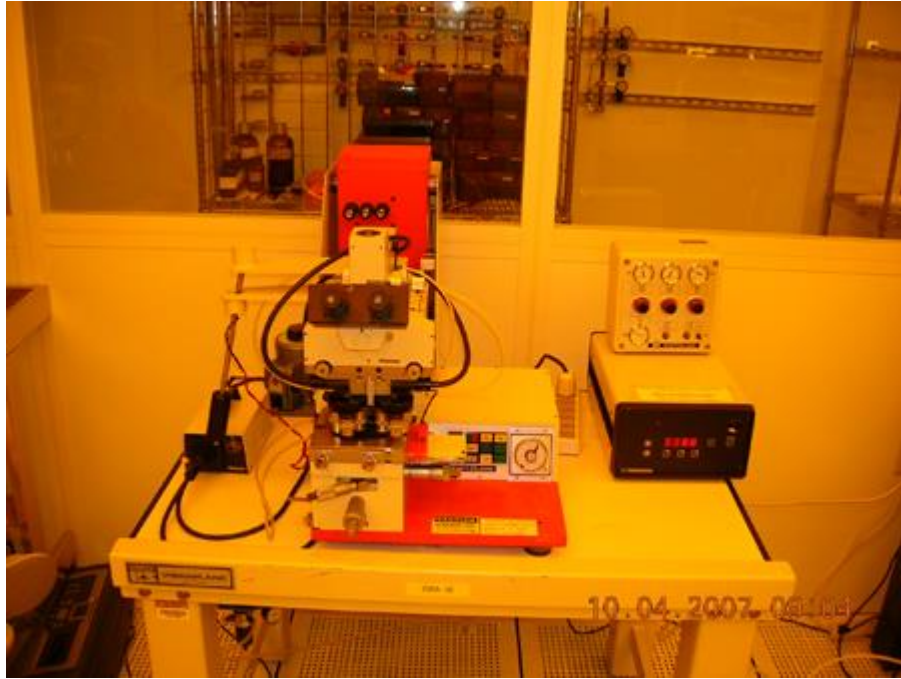
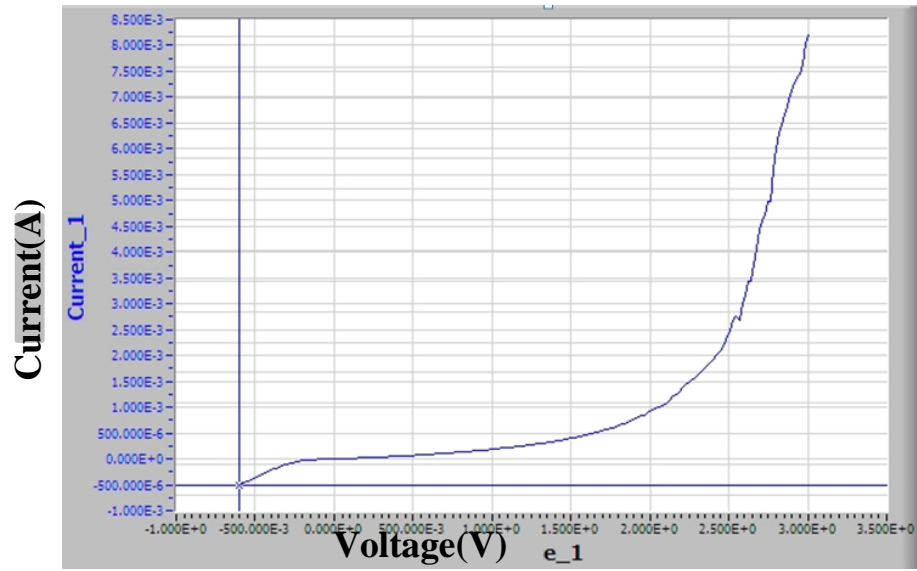


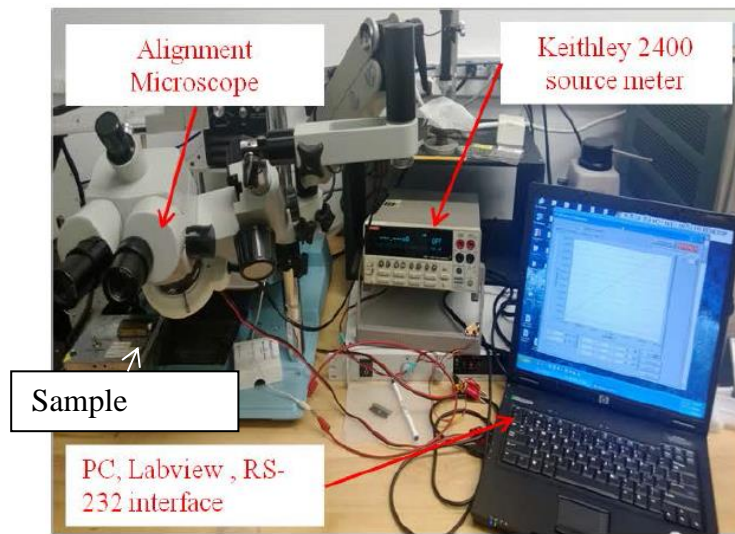
Figure 2.7: Karl Suss MJB-3 Mask Aligner used for GeSn devices fabrication

2.10 Current-Voltage Measurement

In order to characterize the electrical properties of the diodes fabricated in this chapter, current-voltage measurements were performed with a Keithley 2400. All data acquisitions were carried out through a data and signal interface (RS-232) controlled by LabVIEW software. All the measurements were performed in the dark with no illumination, the measurement apparatus and an example of measurement data are shown in Fig. 2.8



(a)



(b)

Figure 2.8: The top image shows I-V measurement data, and bottom image shows the I-V measurement setup components such as Keithley 2400 source meter, alignment microscope and the Lab View interface.

2.11 Rutherford Backscattering Spectrometry (RBS)

RBS is an analytical technique that can help determine the structure and composition of the materials. It measures the backscattering (number and energy) of a beam with high energy (number and energy) after it collides with atoms in the near surface region of the sample it was impinged upon. The RBS consists of a source of helium ion, an accelerator to convert them into high energy alpha particles and a detector to measure the energies of backscattered ions. In this dissertation, Sn composition was measured by RBS measurements which were performed at Rutgers University Tandem Accelerator. The RBS system vacuum chamber pressure was $\sim 10^{-4}$ Pa, and the probe beam consisted of 2 MeV He^{++} ions with a 10-20 nA beam current incident on the sample with a beam spot diameter of about 2mm. A Si surface-barrier detector set at a 163° scattering angle with an energy resolution of about 12 keV was used. The error in RBS measurement was obtained from the 20 nm depth resolution of the RBS set up which has a detector energy resolution $\sim 12\text{keV}$ and plus RBS has an error of about 3% related to current integration.

RBS channeling is used to determine the structure of single crystal samples. During channeling, the rows of atoms are aligned parallel to the incident beam. These rows shield the atoms after the first few monolayers by the surface atoms. The backscatter is only from the first few monolayers which can give information about the crystal structure, such as crystal orientation and crystal perfection.

Angle dependent RBS channeling and random alignments were used to evaluate the crystalline quality and the amount of substitutional Sn in the alloys. Backscattered spectral data was analyzed using the SIMNRA simulation program. The ratio of the backscattered

yield (counts) between the channeled and random directions is the yield ratio χ_{\min} , which is an indication of the crystal quality.

$$\chi_{\min} = \text{Channel Yield/Random Yield} \quad (2.10)$$

From the channeled and the random spectra, χ_{\min} was calculated for both the host and the impurity atoms. In this work, RBS measurements were done on Ge_{1-x}Sn_x alloys where Ge was the host atom and Sn was the impurity atom. The RBS channeling scattering yield was used to determine the lattice position of the impurity atoms. If the reduction in scattering yield of the impurity during channeling is equal to that of the host crystal, then the impurity is considered to be present on a lattice site (substitutionally). If the impurity is present interstitially, or if the atoms are displaced by more than 0.1 Å from the lattice sites, then the scattering yield of the impurity atom is much higher (does not show same decrease as host crystal) due to being exposed to the channeling ions[83-85]. The reduction in scattering yield is described by the parameter χ_{\min} . The fraction of Sn atoms (S) that are located on substitutional lattice sites was calculated using the equation [85];

$$S = \frac{(1-\chi_{\min-\text{impurity/Sn}})}{(1-\chi_{\min-\text{host/Ge}})} \times 100\% \quad (2.11)$$

2.12 Secondary Ion Mass Spectrometry (SIMS)

Secondary ion mass spectrometry (SIMS) uses a focused ion beam to sputter the surface of the sample and analyzes the ejected ions from the sample to determine the composition. These ejected (secondary) ions are detected by a quadrupole mass spectrometer which uses the mass/charge ratio to determine the elemental or molecular composition of the sputtered sample. Using known reference standards, SIMS can quantify the amount of different materials in the sample [86].

Chapter 3

GeSn HETEROJUNCTION DIODE

3.1 Introduction

Recently there has been interest in the development of $\text{Ge}_{1-x}\text{Sn}_x$ alloys due to their predicted properties of indirect-to-direct band gap crossover at Sn contents near 6% [4], and their compatibility with silicon technology [1,4]. Non-equilibrium growth methods such as molecular beam epitaxy (MBE) and chemical vapor deposition (CVD) are required to obtain Sn contents in excess of the thermodynamic equilibrium values, due to the low solubility of Sn in Ge [38] and the nearly 15% lattice mismatch between α -Sn and Ge [39].

Recent interest in GeSn has motivated studies of electrical and optical devices. The properties of p-i-n photodetectors as well as the infrared emission from GeSn diodes have been reported with up to 4% Sn content [19-20, 44, 22]. The electrical characteristics of GeSn diodes need further investigation, however, with increasing Sn content. In this chapter, the electrical measurements of heterojunction diodes fabricated from epitaxial layers of boron doped p-type $\text{Ge}_{1-x}\text{Sn}_x$ grown by MBE on n-type Ge-substrates with up to 9% Sn, and some of their characteristics and limitations are reported

3.2 GeSn Alloy Growth and Device Fabrication

The p-doped GeSn alloys were grown by solid source MBE (Fig. 3.1.) on three inch diameter Ge (001) wafer substrates that were n-type doped and also undoped. The n-type Ge (001) substrates had resistivities in the range of 0.005 – 0.02 Ω -cm, and the undoped Ge (001)

wafer substrates had room temperature resistivities of 40 Ω -cm. The Ge substrates were prepared for growth by degreasing with solvents (TCE, Acetone and Methanol), cleaning with detergent (FL-70) to remove particles, etching in dilute hydrofluoric acid $\text{H}_2\text{O}:\text{HF}$ (10:1) and finally dipping in a solution of dilute hydrogen peroxide $\text{H}_2\text{O}:\text{H}_2\text{O}_2$ (10:1) to obtain smooth surfaces as previously reported [40]. The substrate was then immediately (within a minute) loaded into the MBE intro chamber, and once the pressure had reduced to 10^{-6} Pa, it was transferred to growth chamber where it was degassed in ultrahigh vacuum at 150 $^{\circ}\text{C}$ for 15 minutes to remove any residual water, followed by degassing for 15 minutes at 200 $^{\circ}\text{C}$. The substrate was then heated to 350 $^{\circ}\text{C}$ for 30 minutes, to desorb surface contaminations and then to 520 $^{\circ}\text{C}$ for 30 minutes to desorb the surface oxide. This procedure was found to clean the Ge wafer and provide a growth surface with minimal impurities.

As performed by Dr. Nupur Bhargava from our group, Ultra high purity sources of Ge (triple zone refined) and Sn (6N purity) were evaporated from thermal effusion cells with pyrolytic boron nitride (pBN) crucibles.

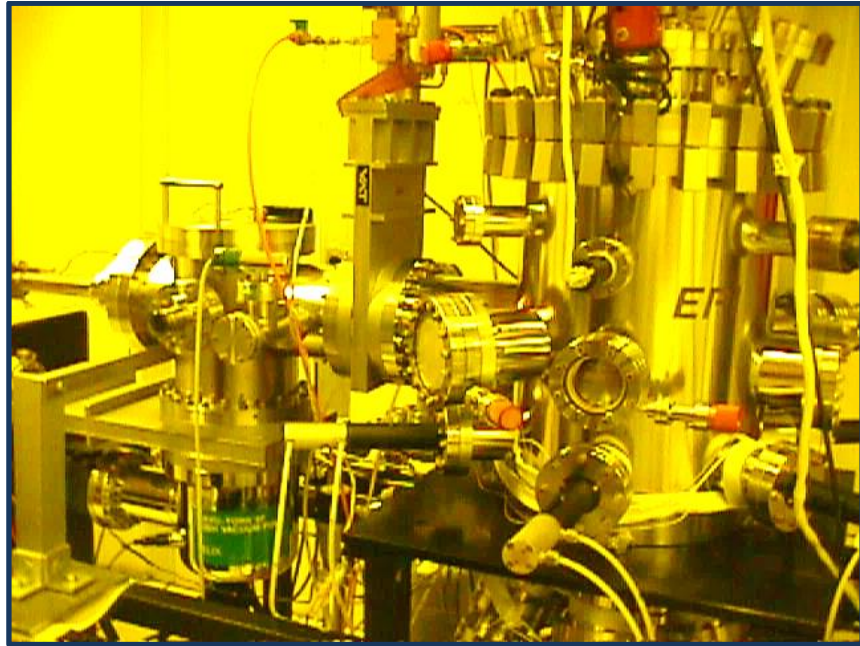


Figure 3.1: Image of the MBE system at University of Delaware (DuPont 242) used to grow GeSn p-n junction diodes. The MBE system is located inside a Class 1000 clean room to avoid any external contamination and for maintaining good quality growth environment

Prior to the GeSn alloy growth, n-doped Ge buffer layers were typically grown at substrate temperatures of 420°C with phosphorus doping to concentrations of $3 \times 10^{18} \text{ cm}^{-3}$. A p-doped Ge layer (~800 nm) on n-Ge substrate was fabricated as a Sn-free reference (Sample D). The growth parameters for these samples are summarized in Table 3.1.

In order to understand the concentration of GeSn alloy grown in this dissertation, RBS and SIMS measurement were conducted as explained in Chapter 2, and the measurement were arranged by Dr. Nupur Bhargava [82]. First, SIMS measurements were done to verify the dopant concentration in GeSn devices. Fig. 3.2 shows the Secondary ion mass spectrometry (SIMS) measurement for the 600 nm p-doped $\text{Ge}_{0.946}\text{Sn}_{0.054}$ /n-Ge (SGC 613:B). Sn composition from SIMS was found to be 5.2% from the SIMS measurement. It was found that the Sn composition was uniform within the doped layer. It was also found that the boron doping in the Sn layer was $2.5 \times 10^{18} \text{ cm}^{-3}$, which closely matched the doping expected from the growth conditions. This doping was found to be uniform. A spike in Boron and Carbon is found beneath the Sn-doped layer which is probably due to an air-exposed surface. Other impurity concentrations were negligible. Similar SIMS measurements on the other p-n junction samples confirmed boron doping $\sim 10^{18} \text{ cm}^{-3}$ in the $\text{p-Ge}_{1-x}\text{Sn}_x$ layers and a phosphorous doping $\sim 10^{18} \text{ cm}^{-3}$ in the Ge buffer layers [82].

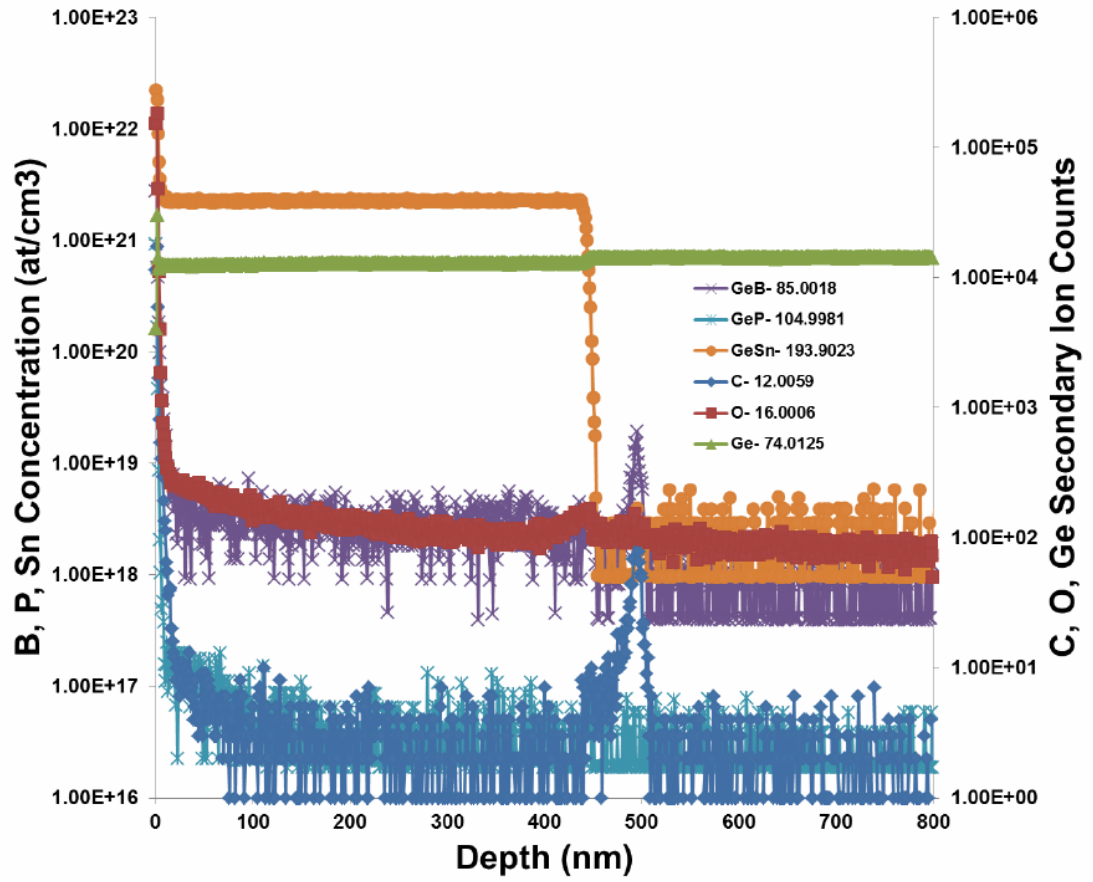


Figure 3.2: SIMS measurement of 600 nm p-doped $\text{Ge}_{0.946}\text{Sn}_{0.054}$ /n-Ge [Courtesy Dr. T. Adams] showing profiles of B, P, Sn, Ge, C and O.

The composition of Sn was confirmed by the technique of Rutherford back scattering spectrometry (RBS). The RBS channeling measurement indicated that greater than 95% of the Sn atoms were located on substitutional lattice sites [82]. Fig. 3.3 shows RBS data for $\text{Ge}_{0.946}\text{Sn}_{0.054}$ /n-Ge showing high amount of substitutional Sn

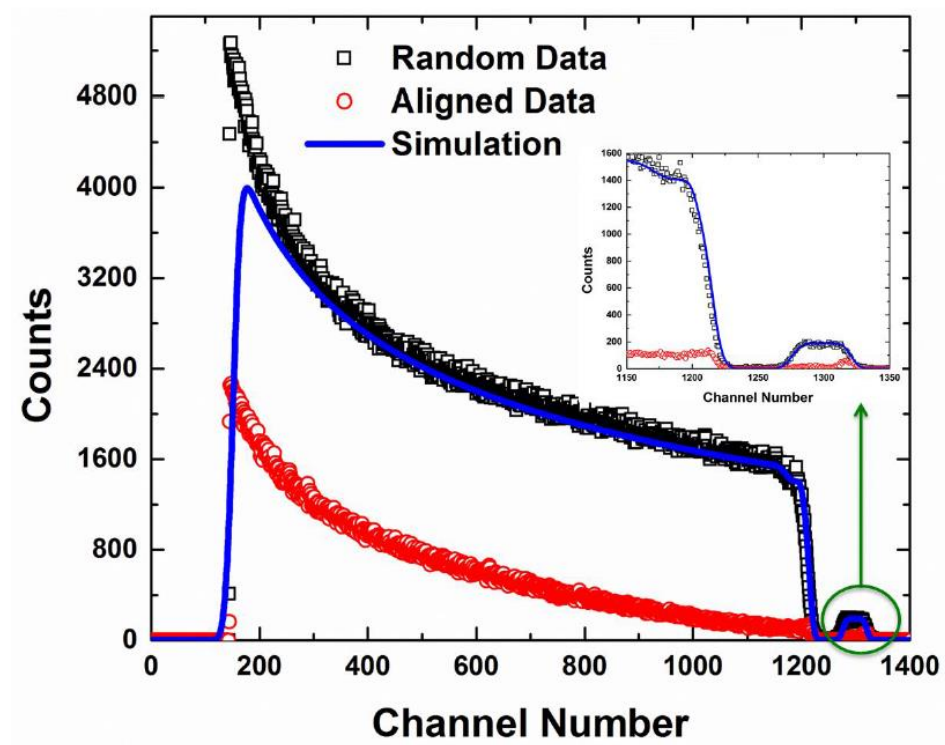


Figure 3.3: RBS random, aligned data along with the simulation of the random data that gave the Sn composition of 5.4%, showing good reduction in scattering yield for both Sn and Ge, which is an indication of high amount(>90%) of substitutional Sn [82].

The amount of substitutional Sn in the p-doped $\text{Ge}_{1-x}\text{Sn}_x$ /n-Ge junctions was calculated using RBS random and channeling measurements as discussed in Chapter 2, Figure 3.3 shows the RBS random, channeling and simulation. From the simulation, using SIMNRA software, of the RBS random data, the Sn composition of the p-n junctions was determined. It can be seen from Fig.3.3, that the Ge and Sn peak both shows good reduced channeling. The χ_{\min} ($\chi_{\min} = \text{Channel Yield}/\text{Random Yield}$) of Ge and Sn are used to calculate the amount of substitutional Sn atoms in the lattice. It was found that χ_{\min} for Ge was 0.083 and χ_{\min} for Sn was 0.144 which gave the amount of substitutional Sn in the Ge lattice to be 93.3% [82]. Similar RBS measurements were done for 2.5% and 8% Sn p-doped $\text{Ge}_{1-x}\text{Sn}_x$ /n-Ge junctions and amount of substitutional Sn was above 90% in all p-n junctions. But when compared with an undoped alloy, the amount of substitutional Sn, as found by RBS, was ~99% in un-doped alloys where as it was ~ 92% in doped alloys (both were ~ 350 nm thick $\text{Ge}_{0.975}\text{Sn}_{0.025}$ layers). The difference in Sn % could be due to the effects of substitutional boron on the RBS yield, or to the presence of boron atoms in interstitial sites.

X-ray Diffraction (XRD) measurements of intensity versus diffraction angle were used to characterize the GeSn epitaxial layers. As in Fig. 3.4, the sharp narrow XRD data showed good, coherent GeSn crystals, and the XRD fringe pattern yielded the thickness of the GeSn layers given in Table 3.1. The GeSn layer thickness from stylus profilometry agreed reasonably with the XRD results.

TABLE 3.1 MBE Growth parameters of GeSn samples

SAMPLE	Sn CONTENT	SUBSTRATE TEMP. (°C) GeSn/Ge	Layer THICKNESS (nm) GeSn/Ge	GeSn Layer - B Doping Conc. (atom/cm ³)
SGC 612: A	9%	225/420	270/30	2×10^{19}
SGC 613: B	5.4%	250/420	600/30	2×10^{18}
SGC 614: C	2.4%	250/420	900/30	5×10^{18}
SGC 554: D	0%	420	800	2×10^{19}

3.2.1 Device Fabrication

As illustrated in Fig. 3.5, standard photolithography and metal evaporation were used to fabricate topside electrical contacts of rectangular meshes with an area filling factor of 50% of Al (300nm) on the p-doped GeSn, and full wafer coverage of Ti/Ag (30/300nm) for the substrate bottom contact. As shown in Fig. 3.6, The width of individual metal mesh stripes was 80 μm . The metalized sample was diced into chips with top surface areas of 2 x 2 mm² and 1 x 1mm² prior to electrical measurements.

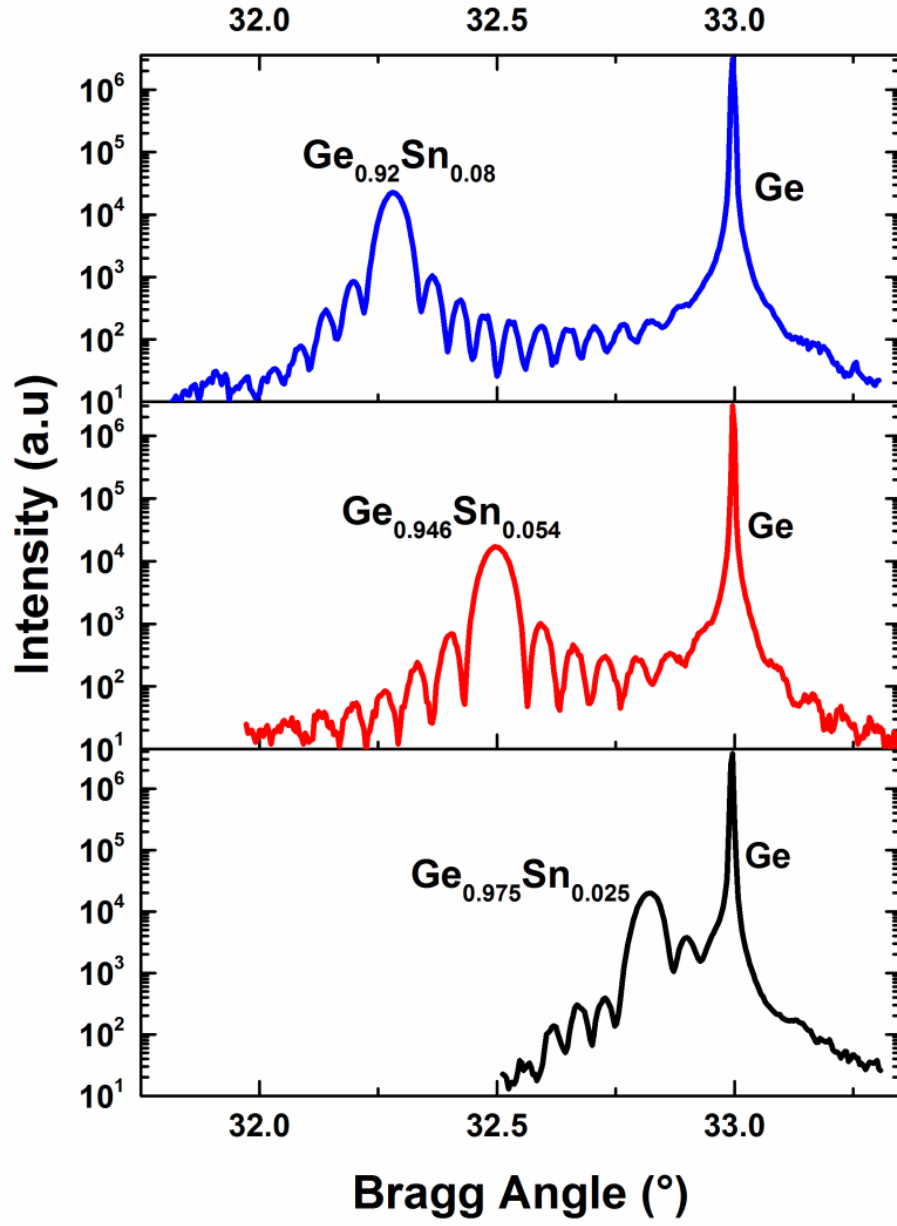


Figure 3.4: ω -2 θ XRD measurements of p-doped $\text{Ge}_{1-x}\text{Sn}_x/\text{n-Ge}$ with x varying from as 2.5%, 5.4% and 8% [82].

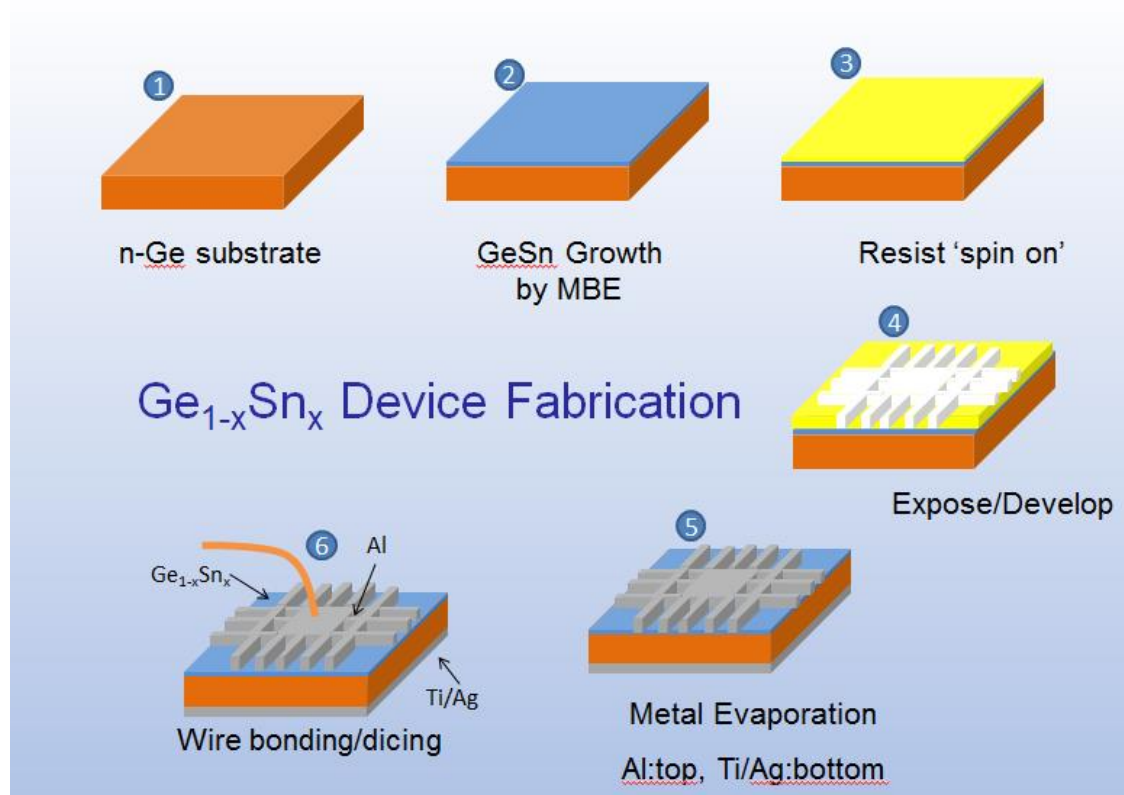


Figure 3.5 : An illustration of the individual steps involved in the photolithography process used to deposit the topside contacts. In numerical order, the steps involved: p-GeSn/n-Ge layer growth (step 2), photoresist spin (step 3), UV exposure (step 4) using the device mask (step 4), photoresist development (step 5).



Figure 3.6: Top view of the device showing the Al meshes with two Au wire bonded

3.3 Device Characterization

The electrical current versus voltage (I-V) characteristics were measured with a Keithley 2400 Source Meter under no illumination. As shown in Fig. 3.7, the diodes showed rectifying I-V characteristics, with a “turn-on” voltage of about 0.4 volt for significant current flow. These I-V characteristics were similar to those reported by Oehme et al. [15], but with a lower dark current density, $\sim 0.25 \text{ A/cm}^2$ at -0.6 V for 9% Sn. This dark current density is similar to that reported by Mathews et al. [20], but higher than reported by Su et al [44]. A low dark current typically indicates high material quality. At a given forward voltage, the current increased with increasing Sn content, suggesting higher conductivity and/or greater injection of charge carriers, as discussed below.

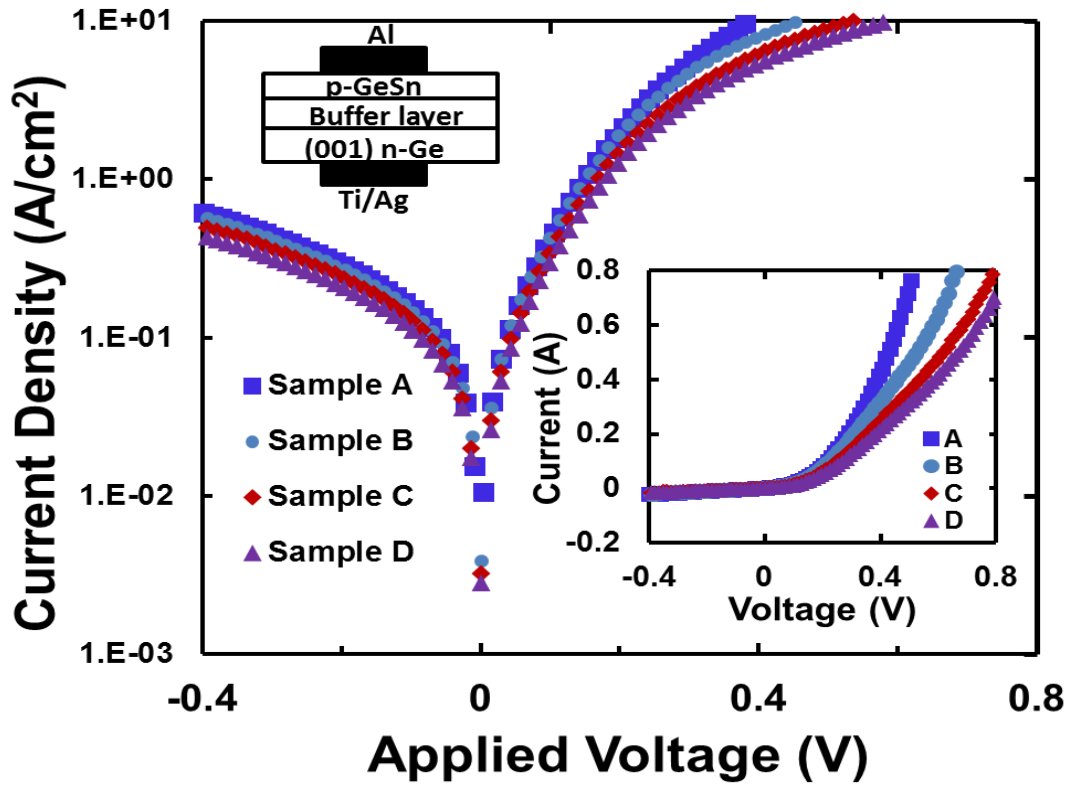


Figure 3.7: Dark current measurements of p-GeSn/n-Ge heterojunction diodes at room temperature, showing current density versus applied voltage. The inset shows I-V measurements of Samples with different Sn contents (A [9%], B [5.4%], C [2.4%], and D [0 %]).

The I-V characteristics were evaluated as follows to extract the diode parameters including: reverse saturation current I_0 , ideality factor η , series resistance R_s , and shunt conductance G .

The diode current equation can be written as:

$$I = I_0 \exp [q/\eta kT (V_a - R_s I_{\text{corr}})] + G V_a, \quad (3-1)$$

with reverse saturation current $I_0 = qA n_i^2 (D_n/N_A L_n + D_p/N_D L_p)$, q the electronic charge, n_i the intrinsic carrier concentration, A the cross-sectional area, $D_{n,p}$ the diffusion constants of electrons and holes, $N_{D,A}$ the donor and acceptor concentrations on the n and p side, $L_{n,p}$ the diffusion lengths of electrons and holes, V_a the externally applied voltage, and I_{corr} the corrected diode current as explained below.

Equation (3-1) was manipulated [41,42] to extract the diode parameters, as shown for Sample A in Fig.3.8 based on the device I-V data. Fig. 3.8(a) displays the derivative dI/dV_a against V_a to obtain $G \approx dI/dV_a$ near 0 volt where it dominated other terms. The extracted $G V_a$ product was subtracted from the current I in Eqn. (3-1) to yield the corrected current $I_{\text{corr}} = I - G V_a$, which was then used to derive the remaining parameters. For R_s , the reciprocal derivative $dV_a/dI_{\text{corr}} = \eta kT/q I_{\text{corr}} + R_s$, was plotted versus $(I_{\text{corr}})^{-1}$ in Fig. 3.8(b). The y-intercept of Fig. 3.8(b) represents R_s , and η was obtained from the slope ($\eta kT/q$). The effect of the variation in B doping ($>1 \times 10^{18} \text{ cm}^{-3}$) in GeSn layers of different samples is accounted for a change in the extracted series resistance, and saturation current density. The I_0 was evaluated from the y-axis intercept by the extrapolation on a semi-logarithmic plot (not shown) of I_{corr} versus $V_a - R_s I_{\text{corr}}$.

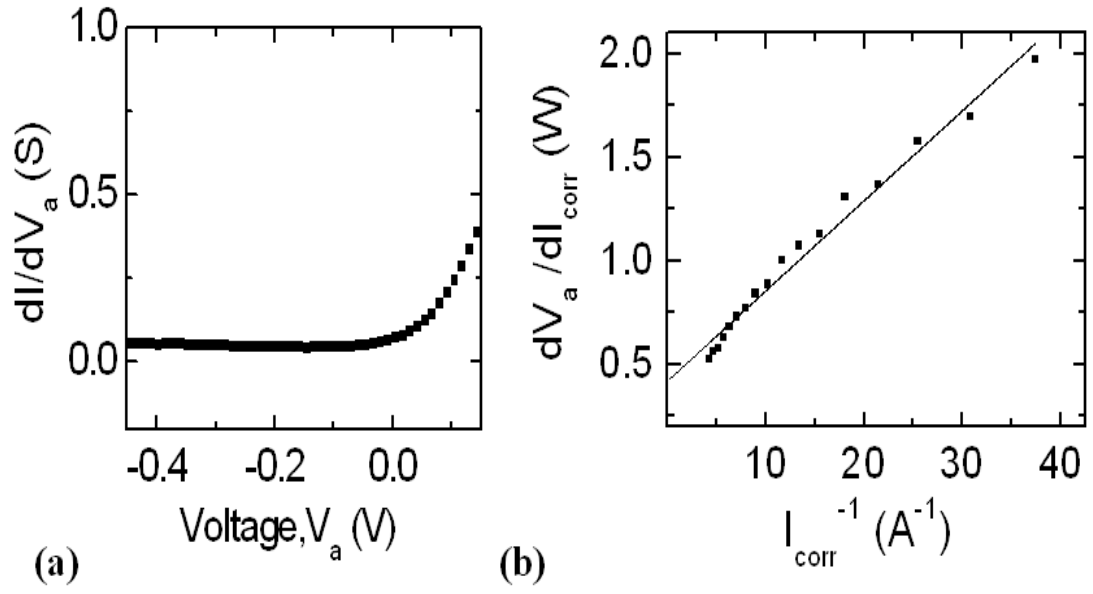


Figure 3.8: The manipulated dark I-V characteristics for the p-GeSn/n-Ge

heterojunction diodes (Sample A). (a) plot of the derivative dI/dV_a against V_a to obtain G ; (b) plot of dV_a/dI_{corr} against $1/I_{corr}$ to obtain η and R_s .

TABLE 3.2: Extracted diodes parameters as derived

Sample No.	Ideality factor(η)	Series Resistance (Ω)	Conductance (S)	Saturation current density, $J_0(\text{A/cm}^2)$
A	1.65	0.42	0.045	$4.8 \cdot 10^{-3}$
B	1.07	0.60	0.078	$3.0 \cdot 10^{-3}$
C	1.20	0.75	0.066	$2.3 \cdot 10^{-4}$
D	1.23	1.05	0.064	$5.5 \cdot 10^{-5}$

Table 3.2 summarizes the extracted diodes parameters. The reverse saturation current increased and the series resistance decreased with increasing Sn content, but no clear trend was found for the ideality factors and the conductance. An ideality factor between 1 and 2 is expected for current contributions from diffusion current and from defect-mediated recombination. For samples with our resistivity and size, a series resistance of about 0.28 Ohm was expected, in reasonable agreement with the observed values. Whereas the diode incremental resistance is about 1 Ohm, the parallel shunt resistance ($1/G$) ranges from about 13 to 22 Ohms and may be due to surface leakage. Based on Equation (3-1), the increase in I_0 with Sn content can be caused by increases in the intrinsic concentration n_i and/or the diffusivities $D_{n,p}$, and to decreases in the doping $N_{D,A}$ and/or to the diffusion length $L_{n,p}$, and also can be influenced by point defects, extended defects, and precipitations. The relative contributions of these parameters to I_0 can be explained by the following analysis. Since higher doping *decreases* I_0 , it is unlikely that the higher doping was responsible for the increased I_0 with Sn. The diffusivity and diffusion length are proportional to the carrier

lifetime $L_{n,p}^2 = D_{n,p} \tau$, and usually all three parameters are affected by the material quality. It is unlikely that one would increase and the others decrease, which would be necessary if these parameters caused I_0 to change. The most likely contributor is the increased intrinsic concentration, which varies exponentially with the bandgap E_g : $n_i^2 \sim T^3 \exp(-E_g/kT)$. An increase in n_i with Sn is consistent with a decreasing bandgap and the observed higher I_0 . The required change in E_g to support the observed change in I_0 is ~ 140 meV for 9% Sn, which is reasonable based on published calculations of E_g versus Sn [49].

From the temperature dependence of the reverse saturation current of Sample A, the Arrhenius activation energy $E_A = 0.29$ eV was found from a fit to $I_0 = I_{\text{Const}} \exp(-E_A/kT)$, with constant pre-exponential factor I_{Const} , as shown in the inset of Fig.3.9. This activation energy is slightly less than $E_g/2$ of Ge ($E_g = 0.67$ eV), and may suggest a process of generation/recombination current. If the observed change in I_0 with temperature were fully attributed to the change in bandgap based on the influence of n_i^2 , then the change would be about 1.8 meV/K, which is larger than the 0.39 meV/K of the Ge bandgap in this temperature range (300K-370K) [45]. If the change in bandgap of GeSn with temperature is assumed to be same as for Ge, then the temperature dependence of parameters such as diffusion coefficient and diffusion length may be responsible for the additional temperature changes. It was not possible, however, to extract the relative contributions from the available data.

The reverse breakdown voltage was extracted from the intersecting tangent lines of the two current branches (below and above the breakdown “knee”) as shown in Fig.3.10. The breakdown voltage decreased with increasing temperature, with a temperature coefficient of -

0.011 V-K^{-1} , consistent with a mechanism of Zener tunneling, which is enhanced in lower bandgap materials.

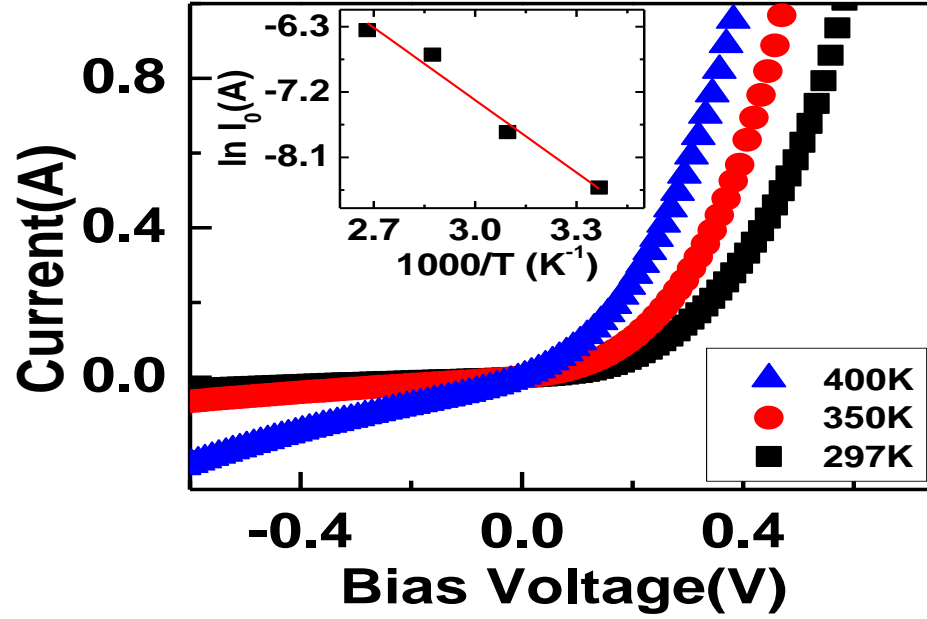


Figure 3.9: Current-voltage characteristics of the n-Ge/p-GeSn heterojunction at different temperatures for Sample A. Inset shows the Arrhenius Plot for the calculation of activation energy of the reverse saturation current (extracted from the diode equation).

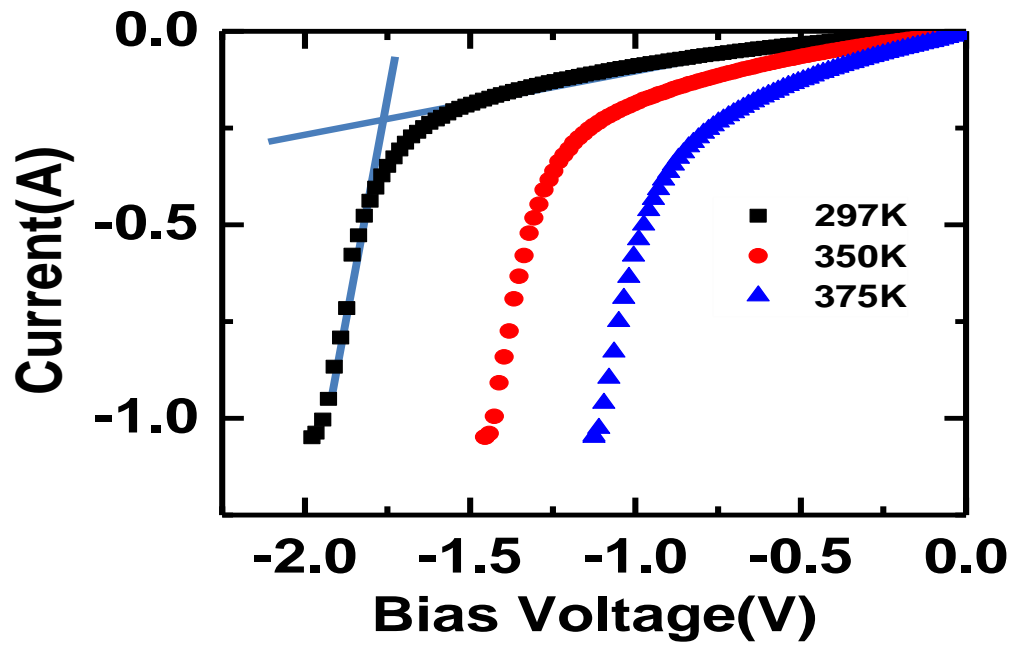


Figure 3.10: Dark reverse biased current-voltage characteristics at various temperatures

for Sample A. The breakdown voltage was about 1.75V at 297K, as indicated by the straight lines along the current branches.

3.4 Conclusion

The electrical properties of GeSn heterojunction diodes were investigated under various conditions, along with the extraction of diode parameters. The magnitude of the reverse saturation current increased with increasing Sn content, suggesting that the addition of Sn reduced the bandgap. These findings indicated that GeSn/Ge p-n diodes have reasonable characteristics and could be useful for the fabrication of future Ge-Sn heterojunction electronic and optoelectronic devices.

Chapter 4

GeSn PHOTODETECTOR RESPONSE

4.1 Introduction

With recent research efforts to understand the properties of GeSn alloys, the characteristics of optoelectronic devices such as infrared detectors and emitters are becoming better understood [52-55]. This report examines the properties of $\text{Ge}_{1-x}\text{Sn}_x$ / n-Ge heterojunction devices as infrared light detectors at various compositions and bias conditions.

4.2 Experimental Details

The undoped $\text{Ge}_{1-x}\text{Sn}_x$ alloys were grown in an EPI (Veeco) 620 molecular beam epitaxy (MBE) system on 76-mm diameter (100) oriented n-type Ge substrates with resistivities of 0.005 – 0.02 $\Omega\text{-cm}$. Ultra high purity Ge (triple zone refined) and Sn (6N purity) were thermally evaporated from effusion cells having pyrolytic boron nitride (pBN) crucibles. The n-type doping used a custom effusion cell having a pBN baffle for preferential phosphorus evaporation from solid GaP pellets. Prior to the undoped $\text{Ge}_{1-x}\text{Sn}_x$ alloy growths, n-type Ge buffer layers were grown and doped to P concentrations of about $3 \times 10^{18} \text{ cm}^{-3}$ at substrate temperatures of 420 °C that produced coherent epitaxy. Three different samples of undoped $\text{Ge}_{1-x}\text{Sn}_x$ alloys with different Sn compositions (sample E: 4%, sample F: 9.8%, and sample G: 12%) and pure Ge (sample H) without Sn were prepared.

All $\text{Ge}_{1-x}\text{Sn}_x$ alloys samples were grown using the identical Sn deposition rate of $\sim 0.80 \text{ \AA/min}$ while varying the Ge deposition rate by adjusting the Ge effusion cell temperature, to change the composition. The compositions of Sn were obtained through Rutherford back-scattering spectrometry (RBS). Channeling RBS measurements indicated that most of the Sn(>95%) was substitutional in the Ge lattice [53]. The thickness of the $\text{Ge}_{1-x}\text{Sn}_x$ layers were measured by stylus profilometry to be ~ 150 , 80 , and 55 nm for samples E (SGC 591), F (SGC 599), and G (SGC 609), respectively and the thickness of epitaxial undoped Ge was $\sim 150 \text{ nm}$ for sample H.

Standard optical photolithography was used to fabricate the $\text{Ge}_{1-x}\text{Sn}_x$ / n-Ge heterojunction devices with structure as shown in Fig. 4.1(b). The evaporated metals of Al (300 nm thick) for the $\text{Ge}_{1-x}\text{Sn}_x$ topside, and Ti/Ag ($30/300 \text{ nm}$ thick) for the bottom n-Ge substrate side were used as electrical contacts. To prepare devices for measurements, the metalized samples were diced using a diamond saw into several chips with a top surface area of either $2\text{mm} \times 2\text{mm}$ or $1\text{mm} \times 1\text{mm}$.

After device fabrication, current-voltage measurements were carried out with a Keithley 2400 Source Meter, with the results described below. Photocurrent (PC) measurements were carried out using Fourier transform infrared (FTIR) spectroscopy in the step-scan mode using a Thermo Nicolet Nexus 870 FTIR spectrometer equipped with a Globar IR light source, as shown in Fig. 4.1(a). After mechanical light chopping (Thorlabs MC 1000) of the optical beam, the light was directed onto the $\text{Ge}_{1-x}\text{Sn}_x$ devices, which were mounted in the cryostat and cooled by a closed loop cooling system. An n-Ge wafer filter was placed in front of the samples (except Sample H) to reduce the current contribution from the Ge

substrate absorption. The generated PC signal was delivered to the FTIR electronics from a lock-in amplifier.

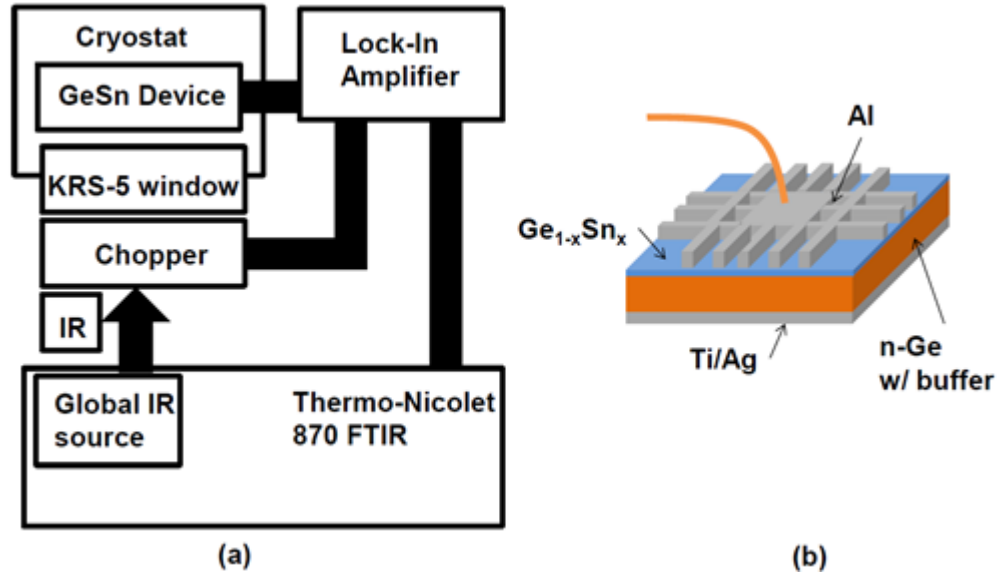


Figure 4.1: (a) Schematic of the experimental setup for photocurrent spectroscopy using an IR source (Globar) and optical chopper. The $\text{Ge}_{1-x}\text{Sn}_x$ device is held at temperature T on a cryostat. A lock-in amplifier and Thermo-Nicolet 870 FTIR were used to measure the spectral response. (b) Diagram of the $\text{Ge}_{1-x}\text{Sn}_x$ / n-Ge heterojunction device structure showing top and bottom metal contacts.

4.3 Results and Discussion

The inset in Fig. 4.2 shows the dark current-voltage characteristics of typical $\text{Ge}_{1-x}\text{Sn}_x$ / n-Ge heterojunction devices at room temperature. The large variation in the magnitude of the dark current between forward and reverse bias indicated good rectifying behavior. At a given forward voltage, the dark current increased with increasing Sn composition, suggesting higher conductivity of the materials and/or greater injection of charge carriers, perhaps caused by a smaller energy bandgap. [54]

Fig.4.2 shows the spectral response of the photocurrent of a typical device of sample F (9.8% Sn) for several different biases at a temperature of 100 K. The spectral photocurrent showed a narrow peak at photon energies below 0.8 eV. The reduced photocurrent above 0.8 eV was attributed to the absorbing n-Ge wafer filter inserted in front of the devices, which effectively removed the photon energies higher than 0.8 eV. The photocurrent increased slightly as the reverse bias voltage increased. At reverse voltages above 0.5 Volts, however, the photocurrent started to saturate, which suggested that all the photo-generated carriers were swept out to the electrodes. The photocurrent decreased with forward bias, because the forward current opposes the collection of photo-generated carriers. The total current through the device is the sum of the dark current and the photocurrent.

Fig. 4.3 shows the spectral photoresponse of $\text{Ge}_{1-x}\text{Sn}_x$ / n-Ge heterojunction devices with different Sn compositions at a temperature of 100 K, and reverse bias of 0.5 Volts. The peak output current from the devices varied from 3 μA (sample G 12%) to 18 μA (sample E 4%), using the n-Ge filter in the FTIR beam path as described above. The photon energies of the peak spectral photocurrents were shifted from 0.849 eV (1.46 μm) for pure Ge (sample H

0% Sn) to 0.596 eV (2.08 μm) for 12% Sn (sample G) at 100 K. The lower energy progression of the spectral peaks was due to the bandgap narrowing as the Sn composition increased, which is consistent with previously reported models [10, 5], and observations [56].

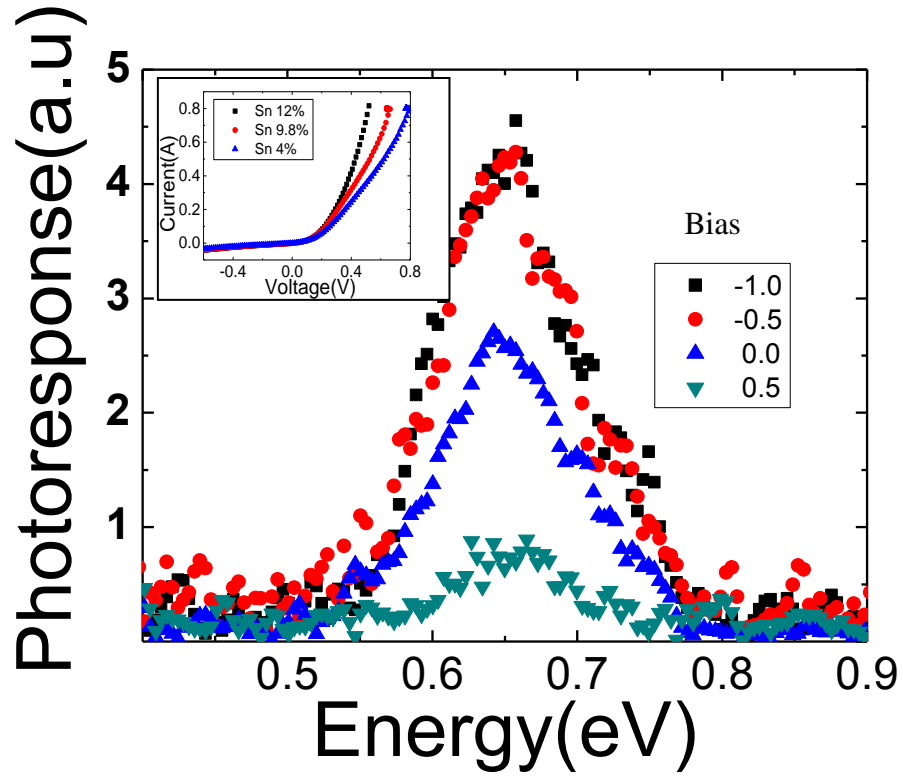


Figure 4.2: Photocurrent response of a $\text{Ge}_{0.902}\text{Sn}_{0.098}/\text{n-Ge}$ heterojunction device at

100K (sample F, with 9.8% Sn): Increasing reverse-biased voltage resulted in larger amplitude of photocurrent that saturated at higher reverse voltages. The inset shows the dark current-voltage characteristics of several $\text{Ge}_{1-x}\text{Sn}_x$ devices with different Sn compositions.

The photon energies of the peak spectral photocurrents were shifted from 0.872 eV (1.42 μm) for pure Ge (sample D 0% Sn) to 0.619 eV (2.0 μm) for 12% Sn (sample C) at 100 K. The lower energy progression of the spectral peaks was due to the bandgap narrowing as the Sn composition increased, which is consistent with previously reported models [59, 5], and observations [56].

The photocurrents of the $\text{Ge}_{1-x}\text{Sn}_x$ / n-Ge heterojunction devices generated from the Globar IR source were compared to the photocurrent of a calibrated Newport 818 Ge detector (responsivity 0.81 A/W at peak wavelength) for calibration. The responsivities at the peak response for samples E (4% Sn), F (9.8% Sn), and G (12% Sn) were calculated to be 0.17 A/W, 0.13 A/W, and 0.03 A/W, respectively, at the temperature of 100K with 0.5V reverse bias. The relatively lower responsivity of the higher Sn composition device (sample G) was possibly due to the much thinner $\text{Ge}_{1-x}\text{Sn}_x$ layer compared to other samples. The relatively low responsivities of all $\text{Ge}_{1-x}\text{Sn}_x$ devices compared to the Ge reference detector were attributed to the: a) relatively thin absorbing layer of the $\text{Ge}_{1-x}\text{Sn}_x$, b) attenuated photons through the Ge filter wafer reaching the absorption layer of the devices, c) relatively large area of Al metal on the surface that blocked the active region (the metal covered ~64% of the surface), and d) some surface reflection from $\text{Ge}_{1-x}\text{Sn}_x$ layer.

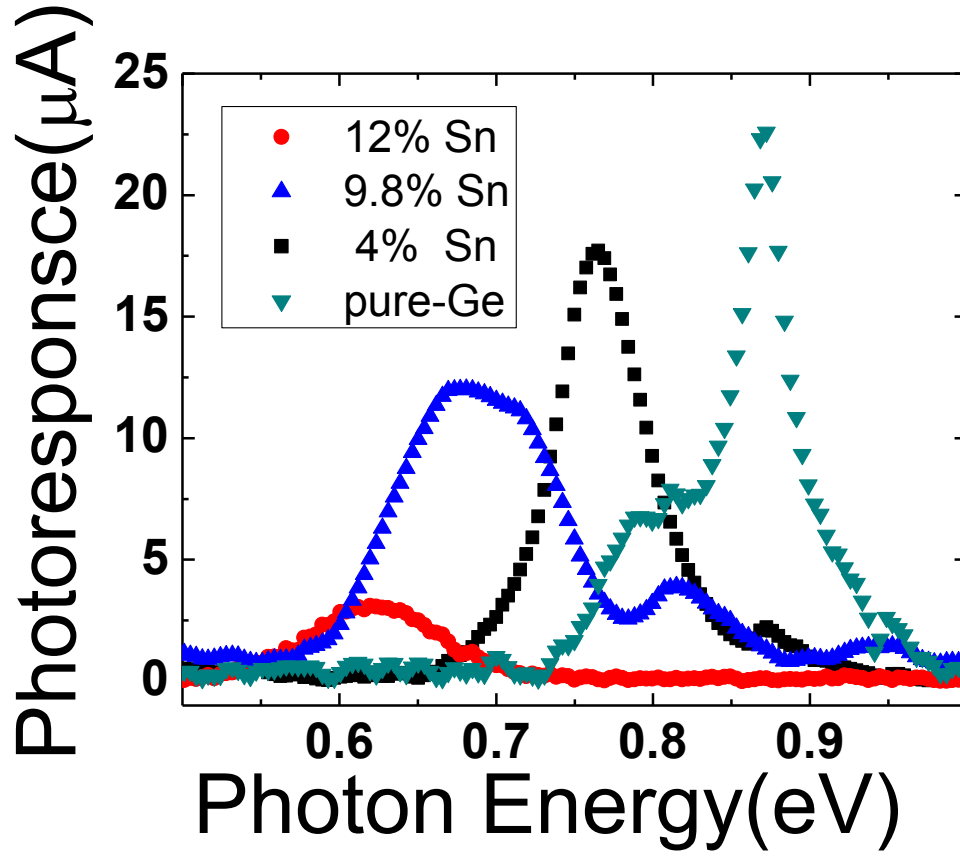


Figure 4.3: Spectral photoresponse in mid-IR regime of $\text{Ge}_{1-x}\text{Sn}_x/\text{n-Ge}$ heterojunction

devices, with different Sn compositions, at 100K. The response peaks lie at 0.619eV (sample G 12% Sn), 0.681eV (sample F 9.8% Sn), 0.765eV (sample E 4% Sn), and 0.872eV (pure Ge sample H, 0% Sn) respectively.

4.4 Conclusions

In summary, the properties of $\text{Ge}_{1-x}\text{Sn}_x$ / n-Ge heterojunction devices grown by MBE were investigated using electrical and photocurrent measurements. The 12% Sn sample (G) showed a photoresponse peak at a wavelength of 2.0 μm . The shift in wavelength in 12% Sn sample (G) from pure Ge was attributed to the bandgap decrease with Sn in the $\text{Ge}_{1-x}\text{Sn}_x$ alloys, which can be very useful for extending the response of the devices into the mid-IR. The bias dependences indicated that the photoresponse saturated with a reverse bias of 0.5 volts, which means all the carriers were swept out to the electrodes at this bias. The $\text{Ge}_{1-x}\text{Sn}_x$ alloys with lower Sn composition showed more photocurrent (higher responsivity) possibly due to the thicker absorption layer.

Chapter 5

NOVEL METHOD OF REACTIVE ION ETCHING

5.1 Introduction

Over the past decades, deep dry etching has become invaluable for fabricating complex electrical, mechanical and optical structures. For instance, a crucial component of any laser is the resonator that provides optical feedback. Microstructures such as resonant cavities are typically fabricated by a time consuming and complex combination of dry and wet etching, cleaving, and polishing [57]. Either by eliminating the need for wet etching steps, or by acquiring selectivity by doping or composition to achieve undercutting, the all-dry reactive-ion etching method described in this chapter greatly simplifies the micro-fabrication of silicon structures. Besides its simpler and lower cost processing, the method described here also enables the fabrication of suspended structures for materials that: a) are not readily etched using wet chemicals, and b) may not provide sufficient selectivity between the supporting and suspended materials. Applications for undercut structures include optical micro-components such as waveguides, resonators, photonic crystals, and MEMS structures such as membranes, cantilevers, micro-springs, acoustic spectral filters[58], and microdisks

For micro-electromechanical systems (MEMS) applications, the etching of silicon is required to relatively large depths (tens of microns) with high aspect ratios (depth of trench versus lateral opening). Conventional wet etchants, such as hydrofluoric acid mixed with nitric

acid [59], result in isotropic undercutting below the masking material. Crystal orientation-dependent etchants, such as potassium hydroxide [60], sodium hydroxide [61], ethylene diamine pyrochatechol [62], and tetramethyl-ammonium hydroxide [63], produce sidewalls that are straight, but that are inclined along preferred crystal planes. For most of these chemicals, the wet etching rate differs for the plane orientations, resulting in shapes that are restricted to rectangular and pyramidal forms. The wet etching rates of silicon also depend on doping concentration and conductivity type [64]. In contrast, ‘dry’ ion etching is somewhat independent of crystal orientation, produces nearly vertical sidewalls, and only weakly depends on doping. Typical dry reactive ion etching (RIE) inside a vacuum chamber occurs due to surface erosion of the desired sample by reactive species and/or ion bombardment.

5.2 Plasma Etching

The basis of plasma-assisted etching is simple; use a gas glow discharge to dissociate and ionize relatively stable molecules forming chemically reactive and ionic species and choose the chemistry such that these species react with the solid to be etched to form volatile products. A basic reactive ion etch (RIE) system, currently the most important plasma configuration, is illustrated in Fig. 5.1 with a list of typical parameters [81]

In this work, we report a simple fabrication method to achieve deep undercutting by employing dry-only reactive-ion etching (RIE), and report the effects of key RIE parameters such as chamber pressure, and radio frequency (RF) power. Although we used this technique for silicon microdisks, it should work with other materials such as Ge, and GaAs, which would require different gas chemistries; however the details of etching these other materials is beyond the scope of this paper.

5.3 System Description: Plasma-Therm 790

As shown in Fig. 5.2, the Plasma-Therm 790 system is configured for Reactive Ion Etching (RIE) of oxides, nitrides, and other semiconductor materials such as Silicon, Germanium. Samples up to 8 inches in diameter can be loaded into the process chamber. The process chamber is pumped by a turbo molecular pump backed by a mechanical rotary pump. The process gases enter the reaction chamber and are ionized by the application of RF(maximum power 500Watt at 13.57MHz). Maximum 7 different processing gases are provided into the chamber. The current system has following gases available for processing: N₂, O₂, CF₄, Ar, H₂, SF₆ and He. The whole process is computer controlled by the graphic display interface as shown in Fig. 5.3.



Figure 5.2: Plasma-Therm 790 system used in this dissertation

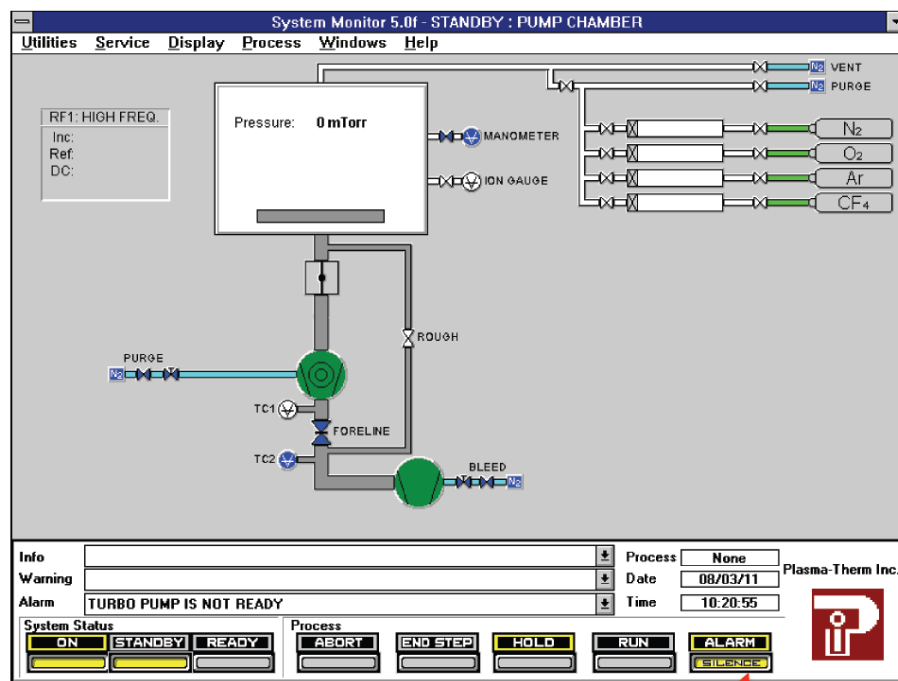


Figure 5.3: Graphic User Interface (GUI) of Plasma-Therm 790 to control a process, showing a process chamber with pressure (here, less than 1mTorr), two green disks for two pumps of turbo, and mechanical rotary, and pumping lines of roughing, and foreline.

5.4 Novel Reactive Ion Etching

The deep etching undercutting method will be described in the context of microdisk fabrication using the semiconductor material of Silicon in this chapter, but could be used for other cantilevered structures and semiconductor materials as well. The fabrication began with uniformly phosphorous-doped ($\rho = 1 - 10\Omega\text{cm}$) silicon (100) oriented wafers. Even though we selected the above mentioned doped silicon as a process material, the process is not confined to a specific doping type, and should work with other dopants as well. The wafers were cleaned with an RCA2-etch [65] for 10 minutes and subsequently rinsed in Buffered Oxide Etch solution (BOE) for 10 seconds.

Our deep undercutting process employed a combination of anisotropic and isotropic etching to remove the native oxide prior to any processing in order to fabricate microdisks those are attached to the underlying substrate by pedestals. Fig. 5.4 shows the two major steps of the undercutting etching processes: Step 1 and Step 2. In Step 1, the perimeter of the upper disk structure was formed by vertical (anisotropic) etching into the masked silicon substrate. In Step 2, a supporting pedestal was created by isotropic etching that removed substrate material under the disk. To our knowledge, previous techniques [66, 67] for the undercutting pedestal formation required selective etching that depended on compositional or doping variations, or on wet etching for the selectivity. In this paper, we present a novel method of forming disks on undercut pedestals with dry-only reactive ion etching. For the reactive-ion etching, we used a Plasma-Therm 790 system [68] with fluoride-based process gases.

5.4.1 Anisotropic Vertical Etching: Step 1

To produce a microdisk, first a cylinder is etched with the desired diameter of the disk, to a depth that corresponds to the disk thickness plus final pedestal height. The sequence of steps is shown in Fig. 5.5. The purpose of Step 1 is to produce this cylinder using the anisotropic etching procedure described below. The microdisk patterns were transferred from a Chrome mask on quartz plate onto the silicon wafer using photolithography with negative photoresist (NR7-1500PY) that was applied with spinner conditions of 3000rpm and 40 seconds (thickness:1.5 μ m). The resist was subsequently soft baked at 120°C for 60 seconds to remove the solvent and improve adhesion. Contact-exposure UV photolithography was employed to expose the resist through the Chrome mask using a Karl Suss MJB-3 mask aligner (40 seconds, 273 Watts). Finally, the resist was hard-baked at 130°C for 60 seconds and developed in resist developer (RD6 [69]) for 25 seconds.

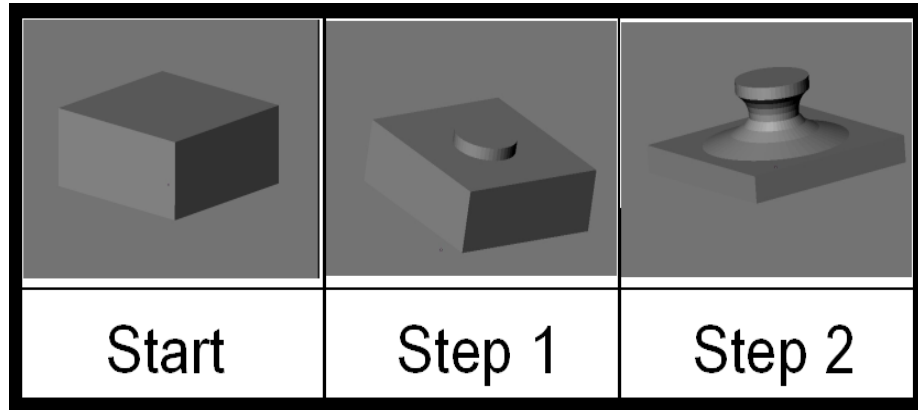


Figure 5.4: A depiction of the result of two major steps of all-dry undercutting etching process. Step 1(anisotropic vertical etching) and Step 2(isotropic undercutting) to fabricate a microdisk. In Step 1, the perimeter of the upper disk structure was formed. A supporting pedestal was created by isotropic etching that removed substrate material under the disk in Step 2.

In order to produce the vertical structures shown in Fig. 5.5(b), a conventional Bosch[70] process would require the use of inductively-coupled plasma (ICP) etching with repeating cycles of two steps: (i) isotropic vertical etching of the desired surface, and (ii) replenishment of a protective polymer masking layer, which is later removed at the etch front during step(i). However, we previously developed a similar cyclic process [71] that employed three sub steps that can be performed on conventional parallel plate reactive ion etchers, and does not require the precise balance between etching and mask replenishment that is characteristic of a two-step process. The anisotropic cyclic process was employed in our present Step 1 to fabricate silicon microcylinders by repeating sequences of: (1) polymer formation, (2) anisotropic removal of the polymer on the bottom trench and (3) isotropic etching. Sulfur-hexafluoride (SF_6), tetrafluoromethane (CF_4), oxygen, hydrogen, argon, and helium were used as process gases.

In Step 1 of our present all-dry undercut process, first, a protective polymer layer that prevented sidewall etching in subsequent sub steps was deposited by a mixture of CF_4 and H_2 , and will be designated as sub-step (1.1). For the subsequent removal of the polymer on the etch-front at the bottom of the structure where the silicon surface needed to be

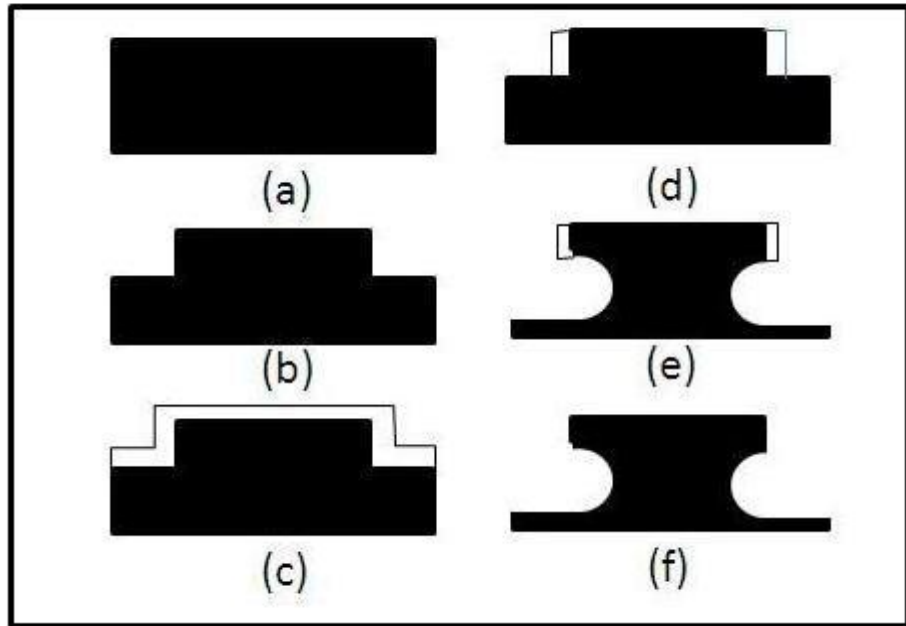


Figure 5.5: A detailed depiction of cyclic dry reactive ion etching process to form a microdisk:

(a) phosphorus doped bulk silicon (001) starting wafer, (b) A microcylinder formed in Step 1 using the three cyclic sub-steps of anisotropic, (c) In preparation for etching Step2, SiO_2 was grown, (d) SiO_2 is removed on bottom, and top by reactive ion etching (e) A supporting structure of pedestal was fabricated in Step 2. using isotropic undercutting etch. (f) A microdisk was formed.

exposed, a second sub-step (1.2) of reactive ion etching was conducted in a gas mixture of 10sccm of SF_6 and 20sccm of He at a low chamber pressure ($\sim 5\text{mTorr}$) which resulted in nearly perpendicular (anisotropic) etching with high ion-directionality. As the third and final sub-step (1.3) of Step 1, the exposed silicon surface was isotropically etched using a gas mixture of SF_6 and He at a higher chamber pressure ($\sim 200\text{mTorr}$). The chamber pressure, gas flows, and duration of this isotropic silicon etch were optimized to minimize soft-mask and sidewall polymer erosion, while maintaining a high silicon etch rate. Those three cyclic sub-steps operate sequentially with each cycle producing a depth of about $0.4\mu\text{m}$. Forty cycles of this three cyclic sub-steps produced etching to a total depth of $16\mu\text{m}$.

5.4.2 Isotropic Undercutting: Step 2

The three cyclic sub-steps (step 1.1 – 1.3) of anisotropic etching in Step 1 produced a disk of the desired width and height. Following Step 1, the silicon was wet oxidized at 950°C for 30 minutes to a thickness of $0.5\mu\text{m}$ to protect the top and sidewall of the cylinder during Step 2 of isotropic etching, which undercut the microdisk and formed a pedestal. SiO_2 was selected as a masking material owing to its high tolerance to SF_6 -based RIE that selectively etches silicon preferentially over SiO_2 (selectivity of 10:1 of Si: SiO_2 for a process of 10sccm SF_6 , 20sccm He at 50Watts RF power and 200mTorr of the chamber pressure). During Step 2 of the isotropic undercutting etching process, the SiO_2 layer on the horizontal plateau was removed during dry etching by the reactive ions delivered vertically due to the electrical potential difference between the bottom electrode and the shower head of the chamber.

Step 2 was designed to etch both the bottom of the trench surrounding the cylinder, and underneath the cylinder simultaneously, forming the shape of a pedestal as shown in Fig. 5.5(f). A processing gas mixture of SF_6 and He was selected for its inherently large silicon etch rate, as compared to other etch gases (C_3HF , CF_4 , etc). Parameters such as chamber pressure, radio frequency (RF) power, exposed area of the silicon and ratios of gas mixtures all influence the net etch rate, selectivity, and sidewall profiles. As described below, the effects of RF power and chamber pressure versus vertical and lateral etch rates were studied for the fixed flow rate ratio of SF_6/He ; 10sccm/20sccm. This particular flow rate ratio was chosen because we found that it produced the highest etch rates, compared to other ratios.

This Step 2 process consisted of two cyclic sub-steps: (2.1) 4 minutes of isotropic etching with SF_6/He chemistry, and (2.2) 10 seconds of purging for pumping out the residuals from the chamber. Fig. 5.6 shows the variation of isotropic etch rate with RF power at constant chamber pressure of 200 mTorr, where the etch depth was measured with a stylus profilometer. The chamber pressure of 200 mTorr was selected for a higher etch rate. The silicon isotropic etch rate increased linearly with RF power.

Fig. 5.7 depicts the amount of etched silicon per cycle versus chamber pressure during the undercutting isotropic etching, based on 10 cycles of the two cyclic sub-steps in Step 2. The amount of undercutting was measured by cross-section SEM on the cleaved wafer. With increasing pressure, the undercut increased due to the greater density of chemical reactants, and we were able to achieve an undercutting of up to 30 μm easily.

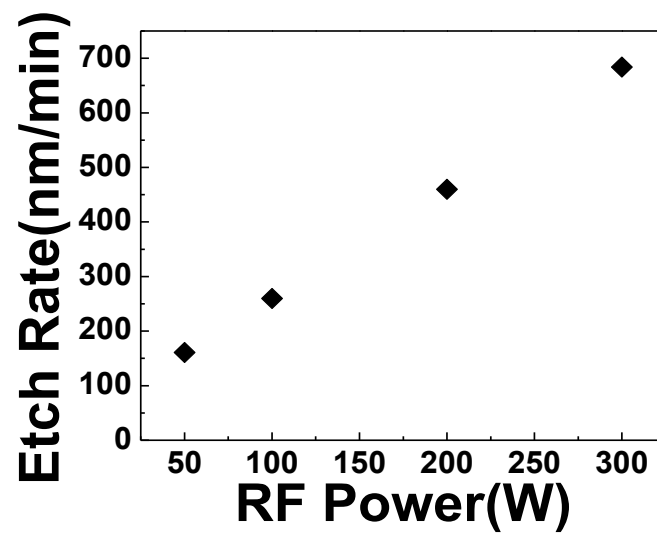


Figure 5.6 : Isotropic silicon etch rate versus RF power for a gas mixture of 10sccm/20sccm; SF_6/He at a chamber pressure of 200mTorr. This condition was used during Step 2 of the undercutting process.

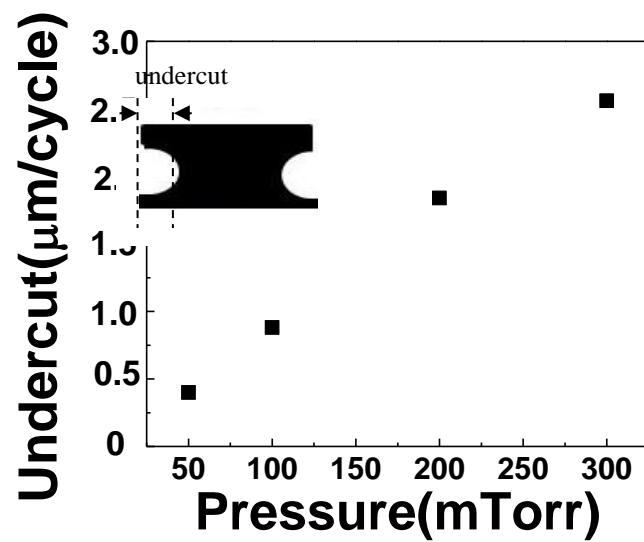
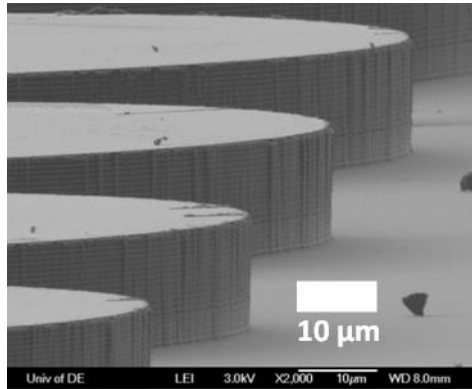
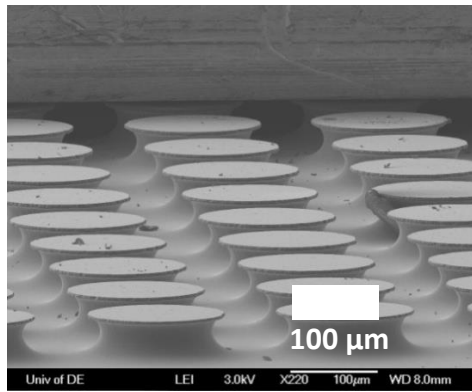


Figure 5.7: Silicon isotropic etch rate ($\mu\text{m}/\text{cycle}$), measured by the extent of undercutting versus pressure for a 10sccm/20sccm; SF_6/He with RF power of 50 Watts.

Fig. 5.8 shows structures made with our dry undercutting process. The microcylinders in Fig. 5.8(a) were formed after the anisotropic etching process of Step 1. The microdisks shown in Fig. 5.8(b) and 5.8(c) were undercut using the dry isotropic etching process described in Step 2 of Fig. 5.5 (f). For finally fabricated microdisk in Fig. 5.8, we cleaned the structure with Hydrofluoric acid to remove any residual oxide. As shown in Fig. 5.8(b), the etched surface on the edge of the disks showed nanometer-scale surface roughness. The process parameters used for fabrication of the microdisks in Fig. 5.8 are summarized in Table 5.1.



(a)



(b)

Figure 5.8: SEM micrographs of microdisks fabricated using novel method of reactive-ion etching process reported here. (a) shows cylinders: diameter: $150\mu\text{m}$, and height: $15\mu\text{m}$. In (b), the cylinders from (a) were undercut showing microdisk arrays

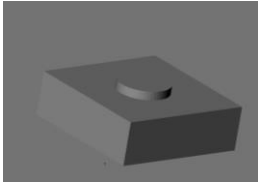
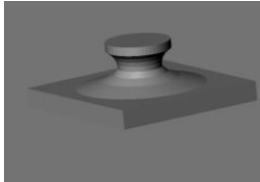
Cyclic All Dry Reactive Ion Etching for a microdisk	
Step 1: Anisotropic	Step 2: Isotropic
Three cyclic sub-steps (8 minutes/cycle)	Two cyclic sub-steps (4 min.10 sec /cycle)
<p>1.1 Polymer formation (4 minutes)</p> <ul style="list-style-type: none"> -chamber pressure: 200mTorr -gas ratio of H_2/CF_4:15 / 25 sccm -RF power: 40 Watts <p>1.2 Polymer removal (30 seconds)</p> <ul style="list-style-type: none"> -chamber pressure: 5mTorr - gas ratio of H_2/CF_4:10 / 20 sccm -RF power: 100 Watts <p>1.3 Etching(3 minutes and 30 seconds)</p> <ul style="list-style-type: none"> -chamber pressure: 200mTorr - gas ratio of SF_6/He:10 / 20 sccm -RF power: 50 Watts 	<p>2.1 Etching(4 minutes)</p> <ul style="list-style-type: none"> -chamber pressure: 200mTorr -gas ratio of SF_6/He :10 / 20 sccm -RF power: 40 Watts <p>2.2 Residual removal (10 seconds)</p> <ul style="list-style-type: none"> -pumping chamber -chamber pressure: < 1 mTorr
	

Table 5.1: Reactive ion etching parameters used to fabricate the microdisks in Figure 5.8. The anisotropic etching process of the left column produces vertical cylinders. The isotropic etching of the right column produces undercutting of the cylinders to create a microdisk. The insets show two subsequent processes(Step 1, and Step 2) to form the microcylinder and microdisk respectively.

5.5 Conclusions

A novel method of RIE for the fabrication of cantilevered silicon micro-structures based on reactive ion etching is presented. This method was developed as an alternative to the combined dry, wet, and selective etching that was often used for undercutting structures such as cylinders to form microdisk resonators on pedestals.

It was found that the extent of under-cutting was controllable by the chamber pressure and RF power. Furthermore, we have investigated the dependency of etch rates on the gas mixture ratio and RF power, and we showed that a large undercut is possible with this technique. The two-step anisotropic and isotropic dry etching of all silicon is a promising for the fabrication of suspended micro-structures in silicon based photonics, due to its simplicity and low cost.

Chapter 6

MAGNETIC TUNNEL JUNCTIONS

6.1 Introduction

In 1988 the discovery of giant magnetoresistance (GMR) effect by Albert Fert and Peter Grunberg has opened the new era of spintronics (spin + electronics). Magnetoresistance (MR) is the change of resistance when a conductor is placed in an external magnetic field. For some conductors such as cobalt, iron and nickel, this magnetoresistance will change depending on the direction of the external magnetic field with respect to the direction of the current through the ferromagnets. In 1988 both Albert Fert and Peter Grunberg's groups independently discovered that some materials show a very large MR, currently known as GMR. These materials consist of multilayers, where ferromagnetic and non-magnetic metals are stacked on each other. Figure 6.1 shows the measurement results of the MR reported from Albert Fert's group (Fig. 6.1 (a)), and from Peter Grunberg's group (Fig. 6.1 (b)), both showing the resistance change of the stacked materials to the external magnetic field. This new finding of GMR was hugely influential on the area of magnetic sensors and data storage. A hard disk storing binary information can use the difference in resistance between parallel and antiparallel layer alignment to store binary 1s and 0s.

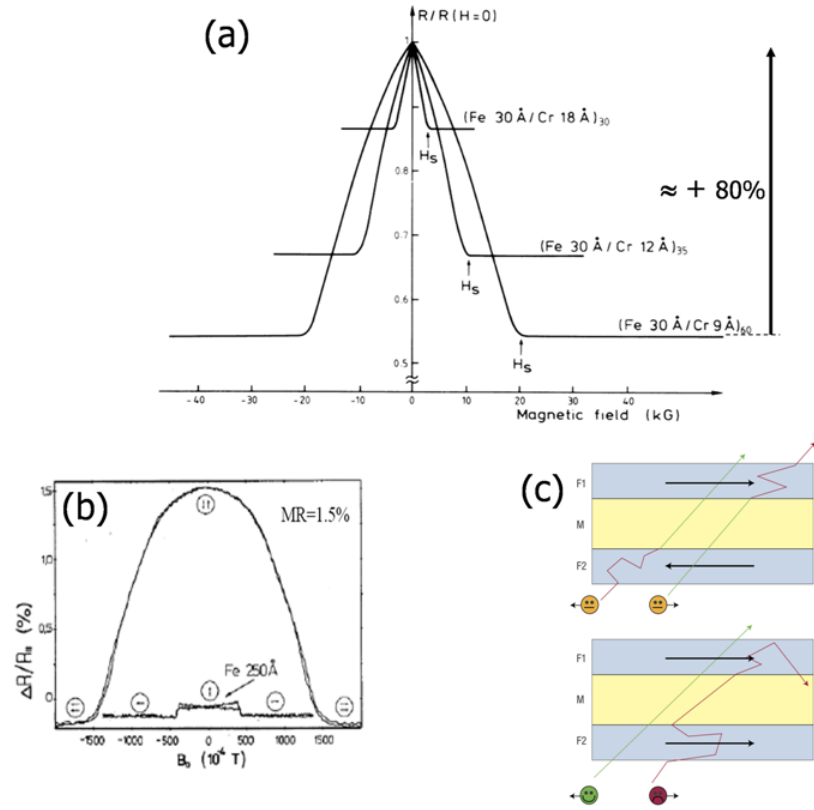


Figure 6.1: First observations of giant magnetoresistance. (a) On Fe/Cr(001) multilayers (Baibich 1988). (b) On Fe/Cr/Fe trilayers (Binash 1989). (c) Schematic of the mechanism of the GMR. In the parallel magnetic configuration (bottom), the electrons of one of the spin channels can go easily through all the magnetic layers and the short-circuit through this channel leads to a small resistance. In the antiparallel configuration (top), the electrons of each channel are slowed down every second magnetic layer and the resistance is high. The current is horizontal on the figure and it is carried by electrons having velocities in all the possible directions with different proportion of rightward and leftward orientations [88].

The demand for even larger magnetoresistive effects for higher data storage densities motivated the development of magnetic tunnel junctions (MTJs) using aluminum oxide insulating tunnel barriers in 1991, and using magnesium oxide later for higher MR. As shown in Figure 6.2, the MTJ has a very thin insulating layer between ferromagnetic layers so that electrons can tunnel through quantum mechanically through the insulating barrier.

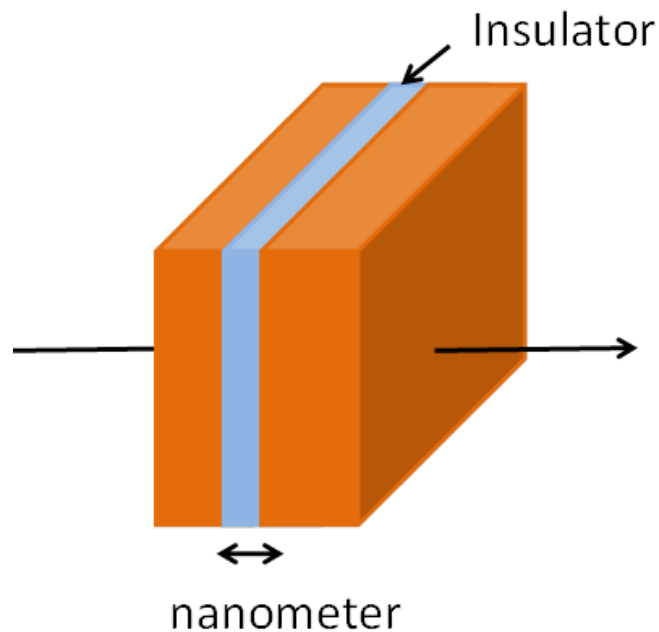


Figure 6.2: Schematic of MTJ, which has a very thin insulating layer between ferromagnetic layers so that electrons can quantum mechanically tunnel through the insulating barrier

In a typical MTJ structure, an insulating layer is sandwiched by two ferromagnetic electrodes as shown in Fig. 6.2. One of the magnetic electrodes is “pinned” such that its magnetization is oriented in the plane of the layer, but is fixed so as not to rotate in the

presence of an applied magnetic field. And a “free” ferromagnetic layer whose magnetization is able to be rotated in the plane of the layer relative to the fixed magnetization of the pinned layer, and an insulating tunnel barrier layer lies in between the ferromagnetic layers. When an electrical bias is applied across the MTJ, electrons that are spin polarized will traverse and tunnel through the thin insulating barrier. The tunneling conductance of the electrons depends on the magnetization of the two electrodes, M1 and M2, relative to the spin orientation of the electrons. The electrical conductance G can be described by the following relation when the relative magnetization orientations M1 and M2 are at an angle Θ ,

$$G(\theta) = \frac{1}{2}(G_P + G_{AP}) + \frac{1}{2}(G_P - G_{AP}) \cdot \cos\theta \quad (6-1)$$

where G_{AP} and G_P are the conductances for $\Theta=180$ and $\Theta=0$, respectively. The tunneling magnetoresistance(TMR) ratio is calculated as:

$$\text{TMR ratio} = \frac{G_P - G_{AP}}{G_P} = \frac{R_{AP} - R_P}{R_P} \quad (6-2)$$

where R_{AP} and R_P are the resistances in the antiparallel and parallel state, respectively.

The mechanism of TMR arises from the difference in the electronic density of states (DOS) at the Fermi level E_F between spin-up $N_{\uparrow}(E_F)$ and spin-down $N_{\downarrow}(E_F)$ electrons. Since electrons preserve their spin orientation during the tunneling process, electrons can only tunnel into the subband of the same spin orientation, as illustrated in Figure 6.3. Therefore, the tunneling conductance is proportional to the product of the Fermi level DOS values of the two electrode regions (M1 and M2) with the same spin orientation. Fig. 6.6 shows two different

configurations of parallel and antiparallel magnetization: parallel magnetization configuration (Figure 6.3 a), antiparallel magnetization configuration (Figure 6.3 b) of the two electrodes showing different tunneling conductance.

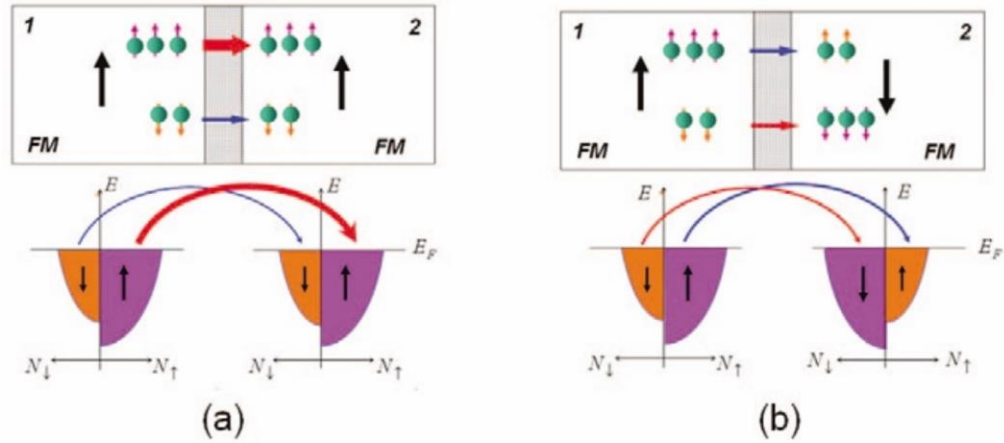


Figure 6.3: Schematic of the TMR effect in an MTJ. During tunneling, electron spin orientation is preserved, i.e. an electron can only tunnel to the spin subband of the same spin orientation, and the conductance is proportional to the product of the Fermi level DOS values of the two electrodes of the same spin orientation. (a) shows parallel magnetization configuration, which means more tunneling conductance of electron. (b) shows antiparallel configuration for less tunneling conductance [87].

Using the definition of the TMR ratio given by equation 6-2, the following relation was first obtained by Julliere[78]:

$$\text{TMR ratio} = \frac{2P_1P_2}{1-P_1P_2} \quad (6-3)$$

where P_1 and P_2 , defined below, are the polarization factors for the two electrodes, respectively. The polarization factors are defined as [79,80]:

$$P = \frac{N\uparrow(E_F) - N\downarrow(E_F)}{N\uparrow(E_F) + N\downarrow(E_F)} \quad (6-4)$$

where $N_\sigma(E)$ is the spin-dependent density of states. Julliere [78] first demonstrated the TMR effect experimentally in 1975, measuring a TMR ratio of 14% in a Fe/Ge/Co junction at 4 K. Over the following decade, extensive research on aluminum oxide barriers yielded a steady increase in the TMR ratio by finding electrodes with higher spin polarization factors and improving the quality of barrier through the introduction of various material processing procedures. In 2004, a TMR ratio of 70% was achieved using a CoFeB/AlO_x/CoFeB junction made with a standard sputtering technique and a CoFeB target composition of Co₆₀Fe₂₀B₂₀

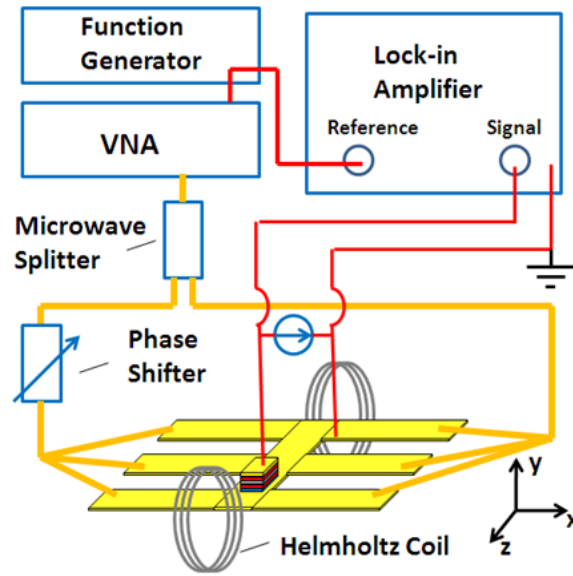
6.2 Motivation

Magnetic tunnel junctions (MTJs) for potential microwave applications have been extensively investigated in recent years [20-24]. Numerous prototype microwave devices have been demonstrated, such as microwave oscillators [27, 72], microwave detectors [26, 73], and microwave modulators [74]. To detect microwaves, one can use either the rectifying effect in

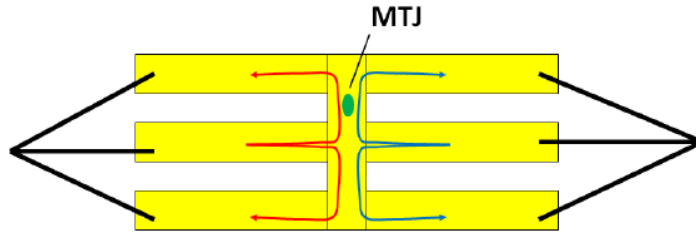
spin diodes [73] or the microwave photoresistance effect [28, 75]. Microwave detectors based on both effects have shown promising sensitivity and unique features such as frequency selectivity. However, the research has so far only focused on the detection of the microwave magnitude, rather than phase. In this dissertation, we will demonstrate microwave phase detection using an MTJ device, which is placed on a common short circuit region across two coplanar waveguides (CPWs).

6.3 Device Fabrication

As shown in Fig. 6.4, a MTJ is lithographically patterned on a common short line of two CPWs. The vertical structure of the MTJ is Cu 120 nm/CoFe 4 nm/ IrMn 15 nm/ CoFe 4 nm/ AlOx 2.3 nm/ NiFe (Py) 20 nm/ Au 50 nm. The magnetization in the CoFe layer is pinned in the x direction (along the CPW length axis) as defined in Fig. 6.4. The CPWs are made of the 120 nm copper. The whole structure is fabricated on a high resistive silicon wafer to reduce the microwave loss. Also shown in Fig. 6.4, microwave signal whose amplitude is modulated by a function generator at 430 Hz is output from a vector network analyzer (VNA). The microwave signal is split into two branches. The right branch is directly fed into the right coplanar waveguide. The microwave in the left branch passes through a tunable phase shifter before it is fed into the left coplanar waveguide. A pair of Helmholtz coils is used to adjust the external DC magnetic field for the ferromagnetic resonance frequency of the MTJ. The MTJ is biased with a constant current source and the modulate microwave induced voltage at 430 Hz is measured by a lock-in amplifier.



(a)



(b)

Figure 6.4: (a) Experiment setup of the MTJ based microwave relative phase detection, showing test equipments of VNA, microwave splitter, function generator, phase shifter, lock-in amplifier, and MTJ device under test on CPWs. (b) Circuit for

microwave phase detection. The MTJ is placed on the common short line of the two CPWs (left, and right CPW).

Microwaves from the two CPWs will be reflected at the short. The microwave currents generate microwave magnetic fields on top of the CPW lines. At the common short line, the microwave magnetic field h_t is the linear superposition of the two microwave currents from both CPWs, $h_t = h_1 e^{i\omega t} + h_2 e^{i(\omega t + \phi)}$, where h_1 and h_2 are the magnetic fields generated by the microwave currents from the left CPW and the right CPW, respectively; ω is the angular frequency of the microwave, and ϕ is the relative phase between h_1 and h_2 . The MTJ microwave detector placed on the common short line responds to the total microwave magnetic field due to the rectifying effect:

$$\Delta V \propto |h_t|^2 = h_1^2 + h_2^2 + 2h_1 h_2 \cos \phi. \quad (6-5)$$

In this experimental demonstration, the nominal power input was 1 mW and the frequency was 2 GHz. A 44 Oe external field is used to set the MTJ at its FMR at parallel configuration and a -39 Oe external field was used to reach FMR at antiparallel configuration. The MTJ was biased with a 10 μ A dc current. The isolation higher than 50dB is measured by a traditional transmission measurement, indicating that there is no cross talk between the two microwaves across the common short. The microwave induced voltage was measured by the lock-in amplifier and the voltage difference between the resonance at parallel and at antiparallel configurations was taken and averaged to cancel out the background signal. The experimental result of the phase detection is shown in Fig. 6.5(a). The microwave induced

voltage revealed a sinusoidal relationship with the phase change tuned by the microwave phase shifter as described in Eq. (6-5). A control experiment was also performed by placing one of the coplanar airprobes onto the identical but adjacent CPW waveguide pattern on the wafer, as illustrated in Fig. 6.5(c). It is worth pointing out that due to the strong isolation of the shorted line, the microwave propagation in these structures of Fig. 6.5(c) should be identical as the structure in Fig. 6.5(b). However, in this case, the MTJ is excited by only one branch of microwave. As a result, the voltage response of MTJ of Fig. 6.5(c) shows much weaker phase dependence. The periodicity of Fig. 6.5(c) is half of the case of Fig. 6.5(a), where two microwave currents are interfering. That periodicity dependence on phase is due to dimensional resonance, where the microwave is reflected from one shorted coplanar waveguide and transmitted into the other waveguide. The reflected microwave goes through the phase shifter twice, which explains the half periodicity in the control experiment

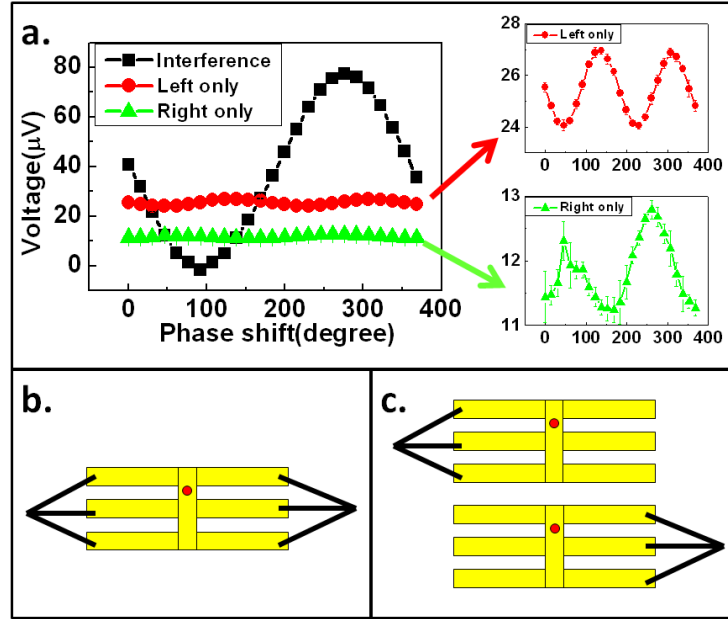


Figure 6.5: (a) Relative phase dependence of the microwave induced voltage. (b) Two microwaves are fed into one structure, producing a response corresponding to the black curve in (a). (c) One microwave is fed into detection structure, while the other microwave is fed into an identical adjacent structure. In this case the microwave in the circuit is the same with the ones in (b). But the induced voltage response is only due to one of the microwave input, corresponding to the red and green curves in (a).

The derivation of the voltage change versus microwave phase given by Eq. (6-5) is based on the assumption that the microwave magnetic field distribution on the short line is uniform. The microwave current tends to flow through a relatively narrow channel of the short line due to the skin effect, however, causing nonuniform field distribution on the short line. A numerical simulation on the circuit using the commercial software High Frequency Structural Simulator (HFSS) was performed. As shown in Fig. 6.6(a) a simulation of the microwave field distribution at the common short line reveals the nonuniformity,.

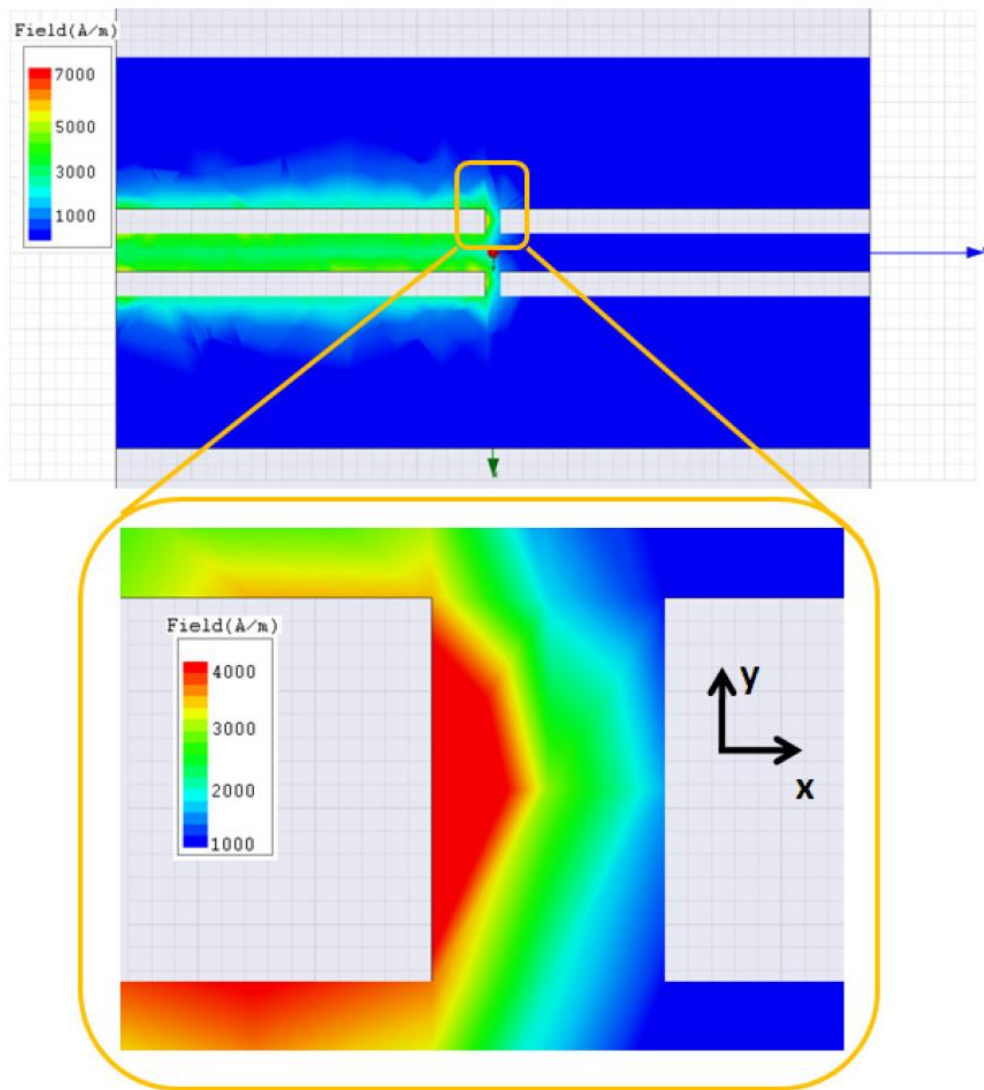


Figure 6.6: HFSS simulation of the surface magnetic field distribution of the structure used in the experiment. The microwave is fed in from the left side. At the common short, there is a non-uniform distribution of the microwave magnetic field.

Assuming the spatial distribution of the microwave is $f(x, y)$, the total microwave magnetic field can be expressed as $h_1 f(x, y) + h_2 f(w - x, y)$ due to symmetry, where h_1 and h_2 are the average microwave magnetic fields generated from each microwave inputs and w is the width of the common short line. Due to the non-uniform microwave magnetic field, the magnetization precession is no longer coherent and cannot be described by a constant magnetic susceptibility. Instead, the local magnetization precession should be calculated as

$$m(x, y) = \oint h_{tot}(x', y') \times \chi(x, y, x', y') \quad (6.6)$$

where $\chi(x, y, x', y')$ is a correlation function like susceptibility that indicates the magnetization precession at (x, y) due to the microwave magnetic field at (x', y') via spin wave coupling [76, 77]. This susceptibility carries a complex spatial term Σe^{-ikx} , where k is the wave number of spin wave.

The photoresistance of this MTJ can be modeled as a parallel circuit with local photoresistance corresponding to the local magnetization precession. Hence, the overall microwave-induced voltage can be modeled as

$$\begin{aligned} \Delta V \propto & \oint \left\{ \left| h_1 \oint f(x', y') \Gamma(x', y', x, y) dA \right|^2 + \left| h_2 \oint f(w - x', y') \Gamma(x', y', x, y) dA \right|^2 \right\} dA \\ & + 2h_1 h_2 \times \left\{ \iiint [f(x', y') f(w - x'', y'') \Gamma(x', y', x, y) \Gamma^*(x'', y'', x, y) e^{i\phi} + c.c.] dA dA' dA'' \right\} \end{aligned} \quad (6.7)$$

This complex expression has a mathematical form of $\eta_0(h_1^2 + h_2^2) + 2\eta h_1 h_2 \cos(\phi + \xi)$. Hence, the microwave phase response developed in this model will be similar to that developed in Eq. (6.5). The unknown parameters η_0 , η and ξ are all intrinsic to the MTJ and

geometry of the CPWs, which can be calibrated. Hence, the spatially non-uniform distribution of microwave magnetic field doesn't invalidate the application of microwave phase detection in this circuit.

6.4 Conclusions

In summary, we have successfully demonstrated that a pair of common shorted waveguides with MTJ mounted on the short line can function as a microwave phase detector. The common short line isolates the two microwave inputs and the microwave current flowing through the common short line is the linear superposition of the two microwaves. By detecting the total emitted magnetic field, the relative phase difference between the two microwaves can be determined. The non-uniform distribution of microwave magnetic field at the common short line may reduce the sensitivity of the phase detection by a geometric factor, which can be predetermined. With the ability to detect magnitude and phase of microwaves, this MTJ-based device may find many applications such as on-chip network analyzer and spectrum analyzer.

\

Chapter 7

DETERMINATION OF SPECTRAL RESPONSIVITY OF GESN PHOTO DETECTORS USING FACTORY CALIBRATED GE AND DTGS REFERENCE DETECTORS

7.1 Introduction

In this chapter, the method used to determine the spectral responsivity of the $\text{Ge}_{1-x}\text{Sn}_x$ / n-Ge heterojunction detector [89] using a factory calibrated Ge detector and a DTGS pyroelectric detector with a flat spectral response is presented.

7.2 Background

A DTGS detector is a pyroelectric device with a flat spectral response, and so can be used to calibrate the spectral responsivity of a device under test relative to a known calibrated detector that absorbs in a different wavelength region. Figure 7.1 shows the flat spectral response characteristic of the DTGS detector (labeled in the red box in the figure) among various infrared detectors. A factory calibrated Ge detector (Newport 818-IR/DB), which is shown in Figure 7.2, was used as the calibrated detector. The procedure to calibrate the measured responsivity of GeSn detectors is detailed below in Section 7.3.

7.3 Responsivity Calibration

In this section, the responsivity calibration procedure using a factory calibrated Ge detector and a DTGS detector with the Thermo Nicolet Nexus 870 FTIR spectrometer equipped with a Globar IR light source is explained.

7.3.1 FTIR set-up

The FTIR was set-up as shown in Figure 7.3 in order to measure the spectral photo-response of the different detectors, and a Ge wafer was placed in the beam path in front of the detectors. Measurements were done by taking current readings from the lock-in amplifier that is synchronized to a light chopper and connecting the output of the lock-in amplifier to the external input of the FTIR.

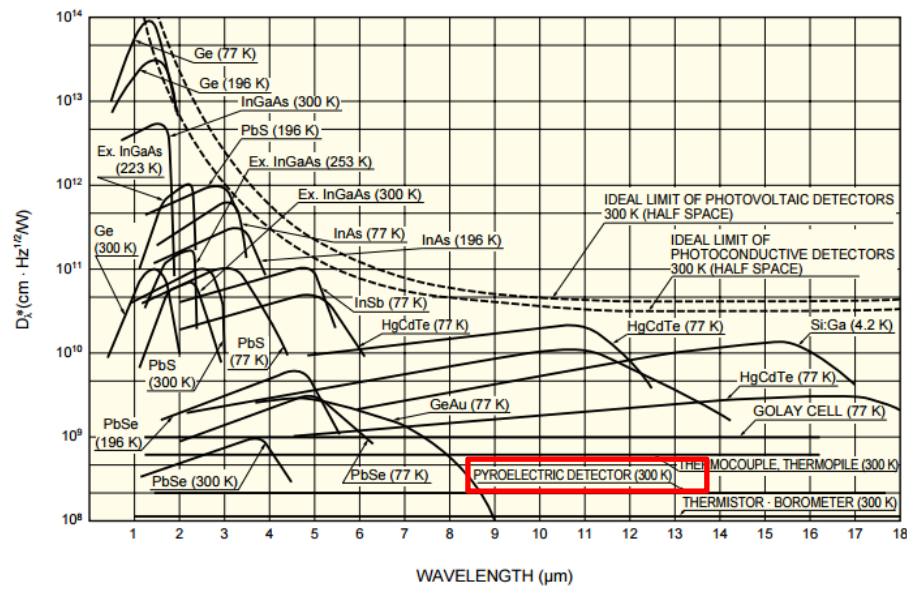


Figure 7.1: Spectral response characteristics of various infrared detectors, indicating that the Pyroelectric detector shows flat response over wavelength from 1.5 μm to 18 μm [90]

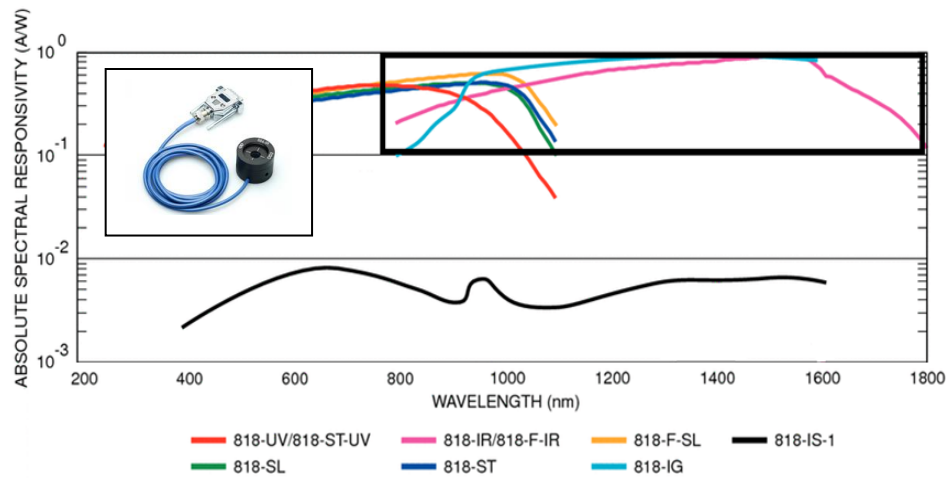


Figure 7.2: Absolute spectral responsivity (A/W) of various detectors from Newport [91]. The pink line shows the absolute spectral responsivity of the Ge detector 818-IR, which is used in this calibration procedure. The inset shows the photograph of Newport Ge detector assembly with the active detector mounted in a black cylindrical holder, and a cable with DB-15 type electrical connector.

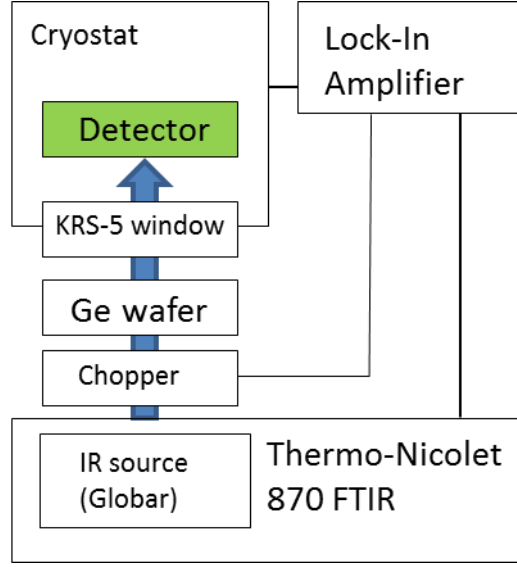


Figure 7.3: Schematic of the experimental setup for photocurrent spectroscopy using an infrared source (Globar) and an optical chopper. A lock-in amplifier and the Thermo-Nicolet 870 FTIR were used to measure the spectral response of the detector that is being tested.

The step by step calibration procedure to determine the responsivity of GeSn detector is outlined below. First, the responsivity of factory calibrated Ge detector, $M_{\text{Ge-Factory}}(\lambda)$, is measured with FTIR in the setup shown in Figure 7.3. Next the responsivity of the FTIR DTGS detector, $M_{\text{DTGS}}(\lambda)$, is also measured. The ratio $F_{\text{Ge-Factory}}(\lambda)$, defined as the responsivity of Ge detector being divided by that of DTGS detector, is calculated and gives the measured Ge detector response relative to the flat DTGS response, so that we can determine more accurate responsivity of the GeSn detector, as shown in Equation (1).

$$M_{\text{Ge-Factory}}(\lambda) / M_{\text{DTGS}}(\lambda) \equiv F_{\text{Ge-Factory}}(\lambda) \quad (1)$$

Since we know the absolute responsivity of factory calibrated Ge detector, $R_{\text{Ge-Factory}}(\lambda)$, we can extract a ratio of the *known calibrated* responsivity to the *measured* responsivity with our FTIR set-up as in Eqn (2). Namely, $T(\lambda)$ is the conversion factor of responsivity measured from our FTIR to the factory published responsivity of the same Ge detector

$$F_{\text{Ge-Factory}}(\lambda) \times T(\lambda) = R_{\text{Ge-Factory}}(\lambda) \quad (2)$$

Figure 7.4 shows the extracted $T(\lambda)$ ranging between 0.2 ~ 0.3 over the wavelength of 1,250nm to 1,850nm.

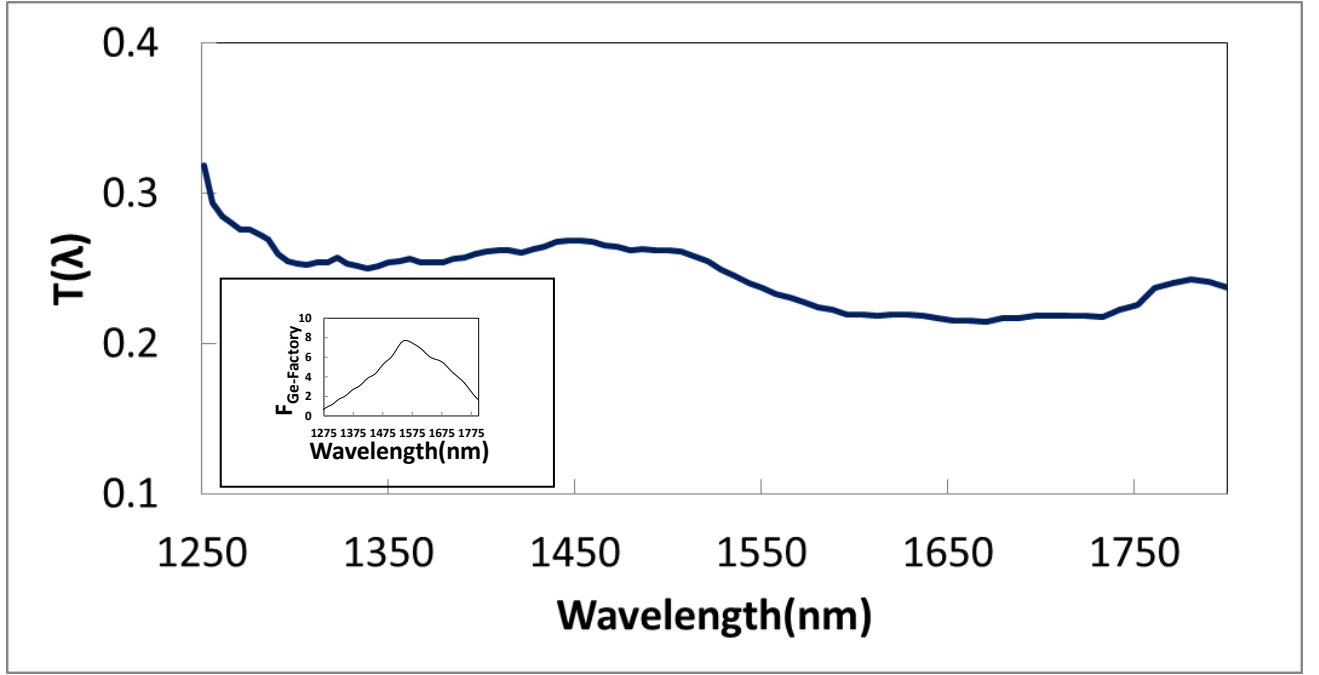


Figure 7.4: Extracted $T(\lambda)$ shows the range between 0.2~0.3. The inset shows $F_{\text{Ge-Factory}}(\lambda)$ in Eqn (1), which is the ratio of $M_{\text{Ge-Factory}}(\lambda)$ to $M_{\text{DTGS}}(\lambda)$.

With a similar method as we did in Eqn. (1), we can measure the responsivity of newly fabricated GeSn detector, and compare the responsivity to that of DTGS detector.

$$M_{\text{GeSn}}(\lambda) / M_{\text{DTGS}}(\lambda) \equiv F_{\text{GeSn}}(\lambda) \quad (3)$$

where $F_{\text{GeSn}}(\lambda)$ is the FTIR response of the GeSn detector under test, relative to the flat DTGS response. Now we can use the conversion factor of $T(\lambda)$, which is the FTIR spectral conversion factor calculated from the both the Ge detector and DTGS detector responses, to determine the absolute responsivity of GeSn detector, $R_{\text{GeSn}}(\lambda)$, which needs further correction for the relative active areas of the detectors. For the longer wavelength response of GeSn detector compared to Ge detector, we linearly extrapolate the conversion factor in Figure 7.5 beyond the original spectral range of 1,800nm of factory calibrated Ge detector in Eqn (4).

$$F_{\text{GeSn}}(\lambda) \times T(\lambda) = R_{\text{GeSn}}(\lambda) \quad (4)$$

Figure 7.5 shows the responsivity of GeSn detector determined from above mentioned procedure with further consideration of active areas of the detectors. GeSn detector tested here has 0.04cm^2 active area, and Newport Ge detector has 0.071cm^2 active area of the detector, which is ~ 1.78 time bigger detection area than GeSn detector. The Inset (a) showing $F_{\text{GeSn}}(\lambda)$ extracted from Eqn (3) from the ratio of $M_{\text{GeSn}}(\lambda)$ to $M_{\text{DTGS}}(\lambda)$. Finally determined responsivity of GeSn detector is ranging from ~ 0.13 to 1.28 A/W

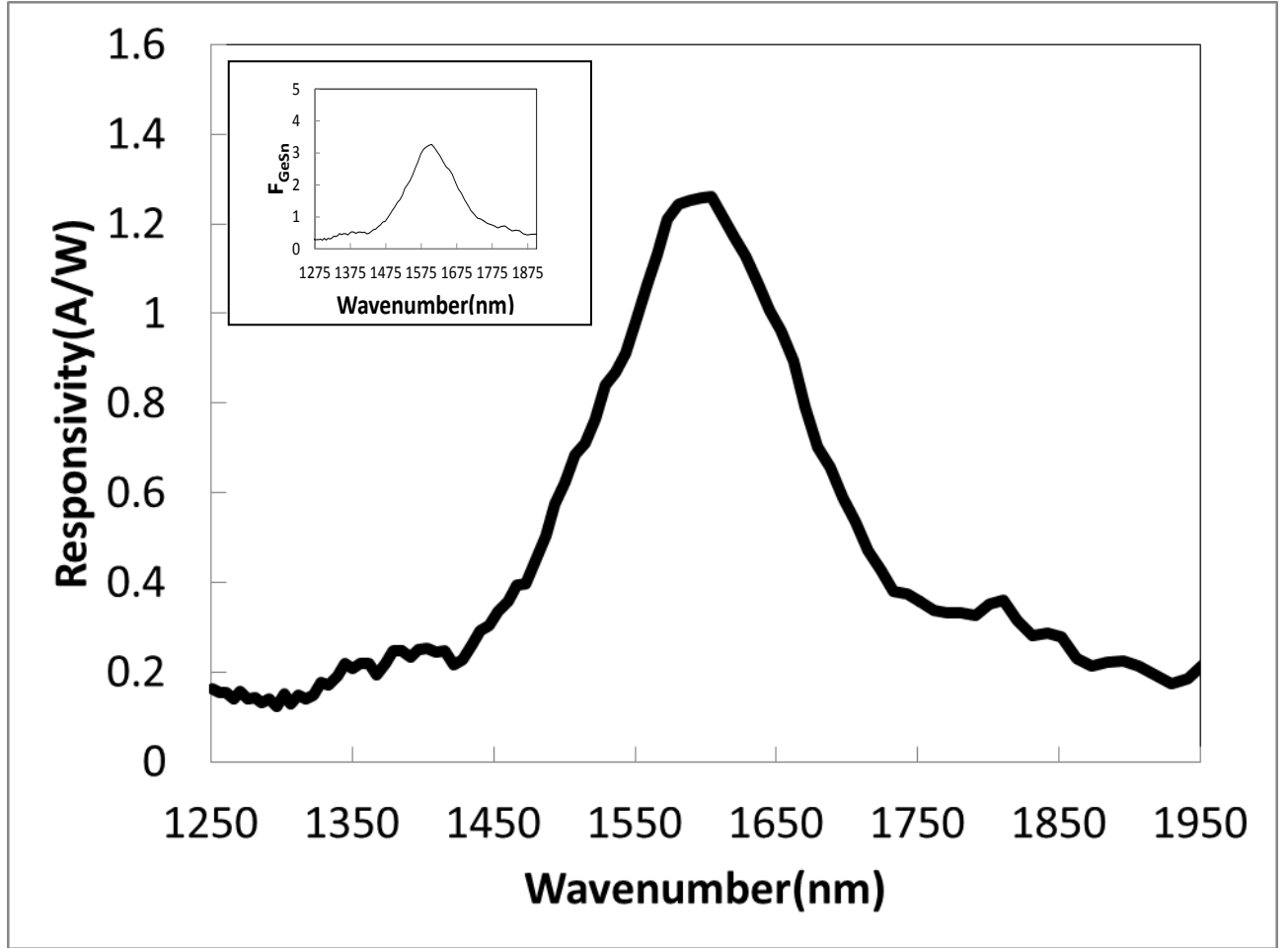


Figure 7.5: The responsivity of GeSn detector determined at the wavelength range of 1,250nm to 1,950nm. The inset (a) shows the ratio $M_{\text{GeSn}}(\lambda)$ to $M_{\text{DTGS}}(\lambda)$, and the inset (b) shows the responsivity of GeSn detector before considering the size of detector area.

7.4 Conclusion

The responsivity of newly fabricated GeSn heterojunction detector was determined using the factory calibrated responsivity of Newport Ge detector and flat response of DTGS detector. The determined responsivity range is from ~ 0.13 to 1.28 A/W.

Chapter 8

SUMMARY AND FUTURE WORK

8.1 Summary

This dissertation presents fabrication and characterization of GeSn alloys using epitaxial growth (MBE), and also presents a novel method of all dry silicon etching, and a microwave phase detection device using MTJ. The second chapter summarizes the method of GeSn alloy growth using MBE, and modification of FTIR for photocurrent measurement, and details of GeSn devices fabrication, and chapter 3, and 4 discuss about electrical and optical properties of GeSn heterojunction devices, and characterization of GeSn diodes, and photocurrent measurements. In Chapter 3, the electrical properties of GeSn heterojunction diodes were investigated under various conditions, along with the extraction of diode parameters. The magnitude of the reverse saturation current increased with increasing Sn content, suggesting that the addition of Sn reduced the bandgap. These findings indicated that GeSn/Ge p-n diodes have reasonable characteristics and could be useful for the fabrication of future Ge-Sn heterojunction electronic and optoelectronic devices, In chapter 4, the properties of $\text{Ge}_{1-x}\text{Sn}_x$ / n-Ge heterojunction devices grown by MBE were investigated using electrical and photocurrent measurements. A redshift in the photon energy of peak absorption of 0.146 eV with increasing Sn composition from 4% to 12% was observed in the photoresponse spectra. The redshift was attributed to the bandgap decrease with Sn in the $\text{Ge}_{1-x}\text{Sn}_x$ alloys, which can be very useful for extending the response of the devices into the mid-IR. The bias dependences of the photodetector indicated that the photoresponse saturated with a reverse bias of 0.5 volts. The $\text{Ge}_{1-x}\text{Sn}_x$ alloys with lower Sn composition showed more photocurrent

(higher responsivity) possibly due to the thicker absorption layer. Chapter 5 presents a new all-dry processing method for the fabrication of suspended silicon micro-structures based on reactive ion etching. This method was developed as an alternative to the combined dry, wet, and selective etching that was often used for undercutting structures. Chapter 6 demonstrated that a pair of common shorted waveguides with MTJ mounted on the short line can function as a phase detector. The common short line isolates the two microwave inputs and the microwave current flowing through the common short line is the linear superposition of the two microwaves. By detecting the total emitted magnetic field, the relative phase difference between the two microwaves can be determined. The non-uniform distribution of microwave magnetic field at the common short line may reduce the sensitivity of the phase detection by a geometric factor, which can be predetermined. With the ability to detect magnitude and phase of microwaves, this MTJ-based device may find many applications such as on-chip network analyzer and spectrum analyzer.

8.2 Future Work

The dissertation has investigated various GeSn diode properties with varying Sn content. However, study on GeSn heterojunction diodes with more Sn concentration and with various doping levels is required. Even though we have demonstrated photoresponse with up to 12% Sn GeSn alloy, more investigation with higher operating temperature, and more Sn incorporation to expand its commercial applications. With incorporation of novel technique of undercutting dry etching, more focus on resonating device such as LASER can be made

REFERENCES

1. R. Soref, "Mid-infrared photonics in silicon and germanium," *Nature Photonics*, vol. 4, no. 8, pp. 495-497, 2010.
2. Y.-Y. Fang, J. Tolle, R. Roucka et al., "Perfectly tetragonal, tensile-strained Ge on Ge_{1-y}Sn_y buffered Si(100)," *Applied Physics Letters*, vol. 90, no. 6, pp. 061915-061915-3, 2007.
3. S. A. Campbell, *The Science and Engineering of Microelectronics Fabrication*, Second ed., New York: Oxford University Press, 2001.
4. J. Kouvetakis, J. Menendez, and A.V.G. Chizmeshya, "Tin-based group IV semiconductors: new platforms for opto- and microelectronics on silicon," *Ann. Rev. of Mater. Res.* 36, 497, 2006.
5. P. Moontragoon, Z. Ikonic and P. Harrison, "Band structure calculations of Si-Ge-Sn alloys: achieving direct band gap materials," *Journal Semiconductor Science and Technology*, 22, 7, 2007.
6. J. D. Sau, and M. L. Cohen, "Possibility of increased mobility in Ge-Sn alloy system", *Physical Review B* 75, 045208, 2007.

7. S. G. Cloutier, P. A. Kossyrev, and J. Xu, "Optical gain and stimulated emission in periodic nanopatterned crystalline silicon," *Nature Materials*, vol. 4, no. 12, pp. 887-891, 2005.
8. B. Min, T. J. Kippenberg, L. Yang et al., "Erbium-implanted high-Q silica toroidal microcavity laser on a silicon chip," *Physical Review A*, vol. 70, no. 3, pp. 033803, 2004.
9. L. Pavesi, L. Dal Negro, C. Mazzoleni et al., "Optical gain in silicon nanocrystals," *Nature*, vol. 408, no. 6811, pp. 440-444, Nov, 2000.
10. J. Michel, J. Liu, and L. C. Kimerling, "High-performance Ge-on-Si photodetectors," *Nature Photonics*, vol. 4, no. 8, pp. 527-534, 2010.
11. M. Oehme, M. Kaschel, J. Werner et al., "Germanium on silicon photodetectors with broad spectral range," *Journal of the Electrochemical Society*, vol. 157, no. 2, pp. H144-H148, 2010.
12. J. Liu, X. Sun, D. Pan et al., "Tensile-strained, n-type Ge as a gain medium for monolithic laser integration on Si," *Opt. Express*, vol. 15, no. 18, pp. 11272-11277, 2007.

13. L. Nataraj, N. Sustersic, M. Coppinger et al., “Structural and optoelectronic properties of germanium-rich islands grown on silicon using molecular beam epitaxy,” *Applied Physics Letters*, vol. 96, no. 12, pp. 121911-121911-3, 2010.
14. X. Sun, J. Liu, L. C. Kimerling et al., “Toward a germanium laser for integrated silicon photonics,” *Selected Topics in Quantum Electronics, IEEE Journal of*, vol. 16, no. 1, pp. 124-131, 2010.
15. M. Oehme, M. Schmid, M. Kaschel et al., “GeSn pin detectors integrated on Si with up to 4% Sn,” *Applied Physics Letters*, vol. 101, no. 14, pp. 141110-141110-4, 2012.
16. R. Roucka, J. Mathews, C. Weng et al., “High-Performance Near-IR Photodiodes: A Novel Chemistry-Based Approach to Ge and Ge–Sn Devices Integrated on Silicon,” *Quantum Electronics, IEEE Journal of*, vol. 47, no. 2, pp. 213-222, 2011.
17. S. Su, B. Cheng, C. Xue et al., “GeSn pin photodetector for all telecommunication bands detection,” *Optics Express*, vol. 19, no. 7, pp. 6400-6405, 2011.
18. R. Roucka, J. Mathews, R. Beeler et al., “Direct gap electroluminescence from Si/Ge_{1–y}Sn_y pin heterostructure diodes,” *Applied Physics Letters*, vol. 98, pp. 061109, 2011.

19. T. Miyazaki, T. Yaoi and S. Ishio, "Large magnetoresistance effect in NiFe/Al- Al_2O_3 /Co magnetic tunneling junction", J. Magn. Magn. Mater. 98, L7-L9,1991.
20. F. B. Mancoff, N. D. Rizzo, B. N. Engel, and S. Tehrani, "Phase-locking in double-point-contact spin-transfer devices", Nature 437, 393-395,2005.
21. T. Moriyama, R. Cao, X. Fan, G. Xuan, B. K. Nikolic, Y. Tserkovnyak, J. Kolodzey, and J. Q. Xiao "Tunnel barrier enhanced voltage signal generated by magnetization precession of a single ferromagnetic layer", Physical Review Letters 100,2008.
22. A. A. Tulapurkar, Y. Suzuki, A. Fukushima, H. Kubota, H. Maehara, K. Tsunekawa, D. D. Djayaprawira, N. Watanabe, and S. Yuasa, "Spin-torque diode effect in magnetic tunnel junctions", Nature 438, 339-342, 2005.
23. S. I. Kiselev, J. C. Sankey, I. N. Krivorotov, N. C. Emley, R. J. Schoelkopf, R. A. Buhrman, and D. C. Ralph, "Microwave oscillations of a nanomagnet driven by a spin-polarized current", Nature 425, 380-383,2003.
24. X. Fan, R. Cao, T. Moriyama, W. Wang, H. W. Zhang, and J. Q. Xiao, "Magnetic tunnel junction based microwave detector", Applied Physics Letters 95, 122501 2009.
25. Thermo Fisher Scientific, "1400 Northpoint Parkway, Suite 50, West Palm Beach, FL 33407, U.S.A."
26. P. R. Griffiths and J. A. De Haseth, Fourier transform infrared spectrometry (Wiley-Interscience), 2007.
27. E. J. Santanu Debnath, John Coffin, "Performance Characteristics of the Advanced ETC EverGlo IR Source."

28. E. Y. Jiang, Advanced FT-IR Spectroscopy Principles, Experiments, and Applications (Thermo Electron Scientific Instruments LLC), 2007.
29. A.S. Brown, "Molecular Beam Epitaxy of III-V Materials including Migration-enhanced Epitaxy," The Encyclopedia of Advanced Materials, ed. R.Cahn, New York, New York: Pergamon Press, 1623-1629,1990.
30. Herman, M. A. "Optical techniques used for in-situ studies of MBE growth processes." *OPTOELECTRONICS REVIEW* : 181-196,1999.
31. Brown, Terence, April Brown, and Gary May. "Anion exchange at the interfaces of mixed anion III–V heterostructures grown by molecular beam epitaxy." *Journal of Vacuum Science & Technology B: Microelectronics and Nanometer Structures* 20.4: 1771-1776,2002.
32. M. A. Herman, and H. Sitter, *Molecular Beam Epitaxy: Fundamentals and Current Status*, Germany: Springer-Verlag, 1989.
33. M. W. Dashiell, "Molecular beam epitaxy of silicon-germanium-carbon heterostructures and silicon based tunnel diodes: Their growth, thermal stability, and characteristics," Ph.D., University of Delaware, United States -- Delaware, 2000.
34. B. A. Orner, "Growth and optical studies of group IV semiconductor alloys and group IV heterostructure devices," Ph.D., University of Delaware, United States -- Delaware, 1997.

35. Oxford Instrument, <http://www.omicron.de/en/our-company>
36. M. W. Dashiell, J. Kolodzey, P. Boucaud et al., “Heterostructures of pseudomorphic Ge_{1-y}Cy and Ge_{1-x-y}Si_xCy alloys grown on Ge (001) substrates,” *Journal of Vacuum Science & Technology B*, vol. 18, no. 3, pp. 1728-1731, May-Jun, 2000.
37. M. J. Coppinger, “Characteristics of germanium-tin photodetectors and terahertz microbolometers,” Ph.D., University of Delaware, United States -- Delaware, 2011.
38. J. Taraci, J. Tolle, J. Kouvetakis, M. McCartney, D. Smith, J. Menendez, and M. Santana, “Simple chemical routes to diamond-cubic germanium–tin alloys,” *Appl. Phys. Lett.*, vol. 78, no. 23, pp. 3607-3609, 2001.
39. C. Thurmond, F. Trumbore, and M. Kowalchik, “Germanium Solidus Curves,” *J. Chem. Phys.*, vol. 25, no. 4, pp. 799-800, 1956.
40. M. Coppinger, J. Hart, N. Bhargava, S. Kim, and J. Kolodzey, “Photoconductivity of germanium tin alloys grown by molecular beam epitaxy,” *Appl. Phys. Lett.*, vol. 102, no.14, pp.141101-1- 141101-3, Apr. 2013.
41. S. S. Hegedus, and W. N. Shafarman, “Thin-film solar cells: device measurements and analysis,” *Progress in Photovoltaics: Research and Applications*, vol. 12, no. 2-3, pp. 155-176, 2004.

42. J. Sites, and P. Mauk, "Diode quality factor determination for thin-film solar cells," *Solar Cells*, vol. 27, no. 1, pp. 411-417, 1989.
43. G. E. Chang, S. W. Chang, and S. L. Chuang, "Strain-balanced $\text{Ge}_z\text{Sn}_{1-z}\text{SixGe}_{1-x-y}\text{Sn}_{1-x-y}$ Multiple quantum-well lasers," *IEEE J. Quantum Electronics*, vol. 46, no. 11-12, pp. 1813-1820, 2010.
44. S. Su, B. Cheng, C. Xue, W. Wang, Q. Cao, H. Xue, W. Hu, G. Zhang, Y. Zuo, Q. Wang, "GeSn p-i-n photodetector for all telecommunication bands detection," *Optics Express*, vol. 19, no.7, pp. 6400-6405, 2011.
45. Y. P. Varshni, "Temperature dependence of the energy gap in semiconductors," *Physica*, vol. 34, no.1, pp.149-154, 1967.
46. J. Werner, M. Oehme, M. Schmid, M. Kaschel, A. Schirmer, E. Kasper, and J. Schulze, "Germanium-tin p-i-n photodetectors integrated on silicon grown by molecular beam epitaxy," *Applied Physics Letter*, 98, 061108, 2011.
47. S. Takeuchi, A. Sakai, K. Yamamoto, O. Nakatsuka, M. Ogawa, and S. Zaima, "Growth and structure evaluation of strain-relaxed $\text{Ge}_{1-x}\text{Sn}_x$ buffer layers grown on various types of substrates," *Semicond. Sci. Tech.* 22, 231, 2007.
48. D. Jenkins, and J. Dow, "Electronic properties of metastable $\text{Ge}_x\text{Sn}_{1-x}$ alloys," *Phys. Rev. B* 36, 7994, 1987.

49. R. Roucka, J. Mathews, C. Weng, R. Beeler, J. Tolle, J. Menéndez, and J. Kouvetakis, "Development of high performance near IR photodiodes: A novel chemistry based approach to Ge-Sn devices integrated on silicon," *IEEE J. Quantum Electron.* 47(2), pp. 213-222, 2011.
50. G. Chang, S. Chang, and S. Chuang, "Strain-Balanced $\text{Ge}_z\text{Sn}_{1-z}\text{-Si}_x\text{Ge}_{1-x-y}\text{Sn}_{1-x-y}$ Multiple-Quantum-Well Lasers," *IEEE J. Quantum Electron.* 46, 12, 2010.
51. H. Tseng, K. Wu, H. Li, V. Mashanov, H. Cheng, G. Sun, and R. Soref, "Mid-infrared electroluminescence from a $\text{Ge}/\text{Ge}_{0.922}\text{Sn}_{0.078}/\text{Ge}$ double heterostructure p-i-n diode on a Si substrate," *Applied Physics Letter*, Vol. 102, 182106, 2013.
52. J. Gupta, N. Bhargava, S. Kim, T. Adam, and J. Kolodzey, "Infrared electroluminescence from GeSn heterojunction diodes grown by molecular beam epitaxy," *Applied Physics Letter*, Vol. 102, 251117, 2013.
53. N. Bhargava, M. Coppinger, J. Gupta, L. Wielunski, and J. Kolodzey, "Lattice constant and substitutional composition of GeSn alloys grown by Molecular Beam Epitaxy," *Applied Physics Letter*, Vol. 103, 041908, 2013.
54. S. Kim, J. Gupta, N. Bhargava, M. Coppinger, and J. Kolodzey, "Current-Voltage Characteristics of Ge/Sn Heterojunction Diodes Grown by Molecular Beam Epitaxy," *IEEE Electr. Device Lett.* 34, Issue 10, pp. 1217-1219, 2013.

55. N. Bhargava, J. Gupta, T. Adam, and J. Kolodzey, "Structural Properties of Boron-Doped Germanium-Tin Alloys Grown by Molecular Beam Epitaxy," *Journal of Electronic Materials*, Vol. 43, Issue 4, pp 931-937, 2014.
56. M. Coppinger, J. Hart, N. Bhargava, S. Kim, and J. Kolodzey, "Photoconductivity of Germanium Tin Alloys grown by Molecular Beam Epitaxy," *Applied Physics Letters*, Vol. 102, 141101, 2013.
57. R.G. Hunsperger, "Integrated *Optics* (New York: Springer)", pp 207, 2001.
58. J.E. Ford, K.W. Goossen, J.A. Walker, D.T. Neilson, D.M. Tennant, S.Y. Park, and J.W. "Interference-Based Micromechanical Spectral Equalizers" *IEEE Journal Of Selected Topics In Quantum Electronics*, vol. 10, NO. 3, pp. 579 -587, 2004
59. S. K. Ghandi, "*VLSI Fabrication Principles*", J. Wiley, New York, 1994
60. Q. B. Vu, D. A. Stricker, P. M. Zavracky, "Surface Characteristics of (100) Silicon Anisotropically Etched in Aqueous KOH", *Journal of the Electrochemical Society*, Volume 143, Issue 3, pp. 1372, 1996.
61. J. G. Smits, "Methods for anisotropic etching of (100) silicon", US. Patent Issue 5,441,600, 15 August, 1995
62. A. K. Chu, K. M. Lee, I. J. Lan, "*Silicon V grooves fabricated using Ta₂O₅ etch mask prepared by room-temperature magnetron sputtering*", *Journal of Vacuum Science and Technology B*, Volume 19, Issue 4, pp. 1169, 2001.

63. M. Paranjape, A. Pandey, S. Brida, L. Landsberger, M. Kahrizi, M. Zen, "Dual-doped TMAH silicon etchant for microelectromechanical structures and systems applications", Journal of Vacuum Science and Technology A, Volume 18, Issue 2, pp. 738, 2000.
64. I. L. Berry, A. L. Caviglia, "High resolution patterning of silicon by selective gallium doping", Journal of Vacuum Science and Technology B, Volume 1, Issue 4, pp. 1059, 1983.
65. RCA cleaning has two steps. The famous RCA clean; $\text{H}_2\text{O}_2\text{-NH}_4\text{OH-H}_2\text{O}$ developed by Werner Kern at RCA laboratory in the 1960's removes organic residue from Si wafers. The second RCA2, $\text{H}_2\text{O}_2\text{-HCl-H}_2\text{O}$ clean is often used to remove metals and other inorganic materials from the surface of Si wafer
66. S. Vicknesh, S. Tripathy, Vivian K. X. Lin, L. S. Wang, and S. J. Chua, "Fabrication of deeply undercut GaN-Based microdisk structures on silicon platforms." , Applied Physics Letters Vol. 90, 071906, 2007.
67. A. N. Cleland and M. L. Roukes, "Fabrication of high frequency nanometer scale mechanical resonators from bulk Si crystals," by Applied Physics Letter Vol. 69, 2653, 1996.
68. Plasma-Therm, LLC., 10050 16th Street North, St. Petersburg, FL 33716, USA
69. RD6: negative photoresist developer manufactured by Futurrex, Inc.

70. Robert Bosch GmbH, US Pat. 5501893,6127273,6214161,6284148
71. T.N. Adam, S. Kim, P-C Lv, G. Xuan, R.T. Troeger, D. Prather and J. Kolodzey, "Cyclic deep reactive ion etching with mask replenishment" J. of Micromechanics and Microengineering, v. 17, pp. 1773-1780, 2007
72. A. Mourachkine, O. V. Yazyev, C. Ducati, and J. P. Ansermet, "nanomagnet microwave resonators functioning in zero applied magnetic field", Nano Letters 8, 3683-3687, 2008.
73. C. Wang, Y. T. Cui, J. Z. Sun, J. A. Katine, R. A. Buhrman, and D. C. Ralph, "Sensitivity of spin-torque diodes for frequency-tunable resonant microwave detection", Journal of Applied Physics 106, 053905, 2009.
74. M. R. Pufall, W. H. Rippard, S. Kaka, T. J. Silva, and S. E. Russek, "Frequency modulation of spin-transfer oscillators", Applied Physics Letters 86, 082506, 2005.
75. N. Mecking, Y. S. Gui, and C. M. Hu, "Microwave photovoltage and photoresistance effects in ferromagnetic microstrips", Physical Review B 76, 224430, 2007.
76. V. E. Demidov, S. Urazhdin, and S. O. Demokritov, "Control of spin-wave phase ,and wavelength by electric current on the microscopic scale, "Applied Physics Letters 95, 262509, 2009.
77. A. Khitun and K. L. Wang, "Nano scale computational architectures with Spin

Wave Bus", Superlattices and Microstructures 38, 184-200, 2005.

78. M. Julliere, "Tunneling between ferromagnetic films", Phys. Lett. A, 54, 225, 1975.
79. R.J. Soulen, Jr., J. Byers, M. Osofsky, B. Nadgorny, et al., "*Measuring the Spin Polarization of a Metal with a Superconducting Point Contact*", Science 282, 85, 1998.
80. D.J. Monsma, S.S.P. Parkin, "Spin polarization of tunneling current from ferromagnet/ Al_2O_3 interfaces using copper-doped aluminum superconducting films", Applied. Physics. Letters, **77**, 720, 2000.
81. H.Janseny, H. Gardeniers, M. Boer, M. Elwenspoek, and J. Fluitman, "A survey on the reactive ion etching of silicon in microtechnology", Journal of Micromechanics and Microengineering V. 6, pp 14–28, 1996.
82. N. Bhargava, "Growth of Silicon-Germanium-Tin Alloys and Fabrication of Magnetic Tunnel Junction Biosensors", Ph.D., University of Delaware, United States -- Delaware, 2013.
83. J. W. M. W.- K. Chu, and M.- A. Nicolet, *Backscattering Spectrometry*, New York: Academic Press, 1978.
84. S. K. Sinha, and P. K. Barhai, "Interface defects in GaN/sapphire studied using Rutherford backscattering spectroscopy and channeling," *Pramana-Journal of Physics*, vol. 62, no. 6, pp. 1293-1298, Jun, 2004.
85. C. Feldman, J. W. Mayer, and S. T. Picraux, *Materials Analysis by Ion Channeling: Submicron Crystallography*, New York: Academic Press, 1982.

86. W.-t. f. encyclopedia. "Secondary Ion Mass Spectrometry,"
https://en.wikipedia.org/wiki/Secondary_ion_mass_spectrometry.
87. J. Zhu, and C. Park, "Magnetic tunnel junctions", Materials Today, Vol.9 (11), pp.36-45, 2006.
88. F. Albert, "Giant Magnetoresistance", Scholarpedia, 6(2), pp.6982, 2011.
89. S. Kim, N. Bhargava, J. Gupta, M. Coppinger, and J. Kolodzey, Optics Express, 22, 11029 -11034, 2014.
90. A. Rogalski, Infrared detectors CRC Press, Boca Raton, FL, 2011.
91. <http://www.newport.com/818-Series-Low-Power-Calibrated-Photodiode-Sensors/827082/1033/info.aspx>

Appendix

PERMISSION LETTERS

Dr. Nupur Bhargava



Sangcheol Kim <cycle87@gmail.com>

Permission required for my disseratation

Nupur Bhargava <bhargava.nupur@gmail.com>
To: Kenny S Kim <cycle87@gmail.com>

Wed, Oct 14, 2015 at 3:05 PM

Hi Kenny,

You have my permission for publishing our work in your dissertation.

Thank you
Nupur

On Tuesday, October 13, 2015, Kenny S Kim <cycle87@gmail.com> wrote:

> Hi Jay, and Nupur,
> I am submitting my dissertation to Grad. Office, and it requires your permission for me to publish the dissertation. Please let me know if it's ok with you. I will just need your email response attached to the end of my dissertation as an appendix.
> Thank you.
> Kenny

Dr. Jay Gupta



Sangcheol Kim <cycle87@gmail.com>

Permission required for my disseratation

Jay Gupta <jayps2005@gmail.com>
To: Kenny S Kim <cycle87@gmail.com>

Wed, Oct 14, 2015 at 9:39 AM

Hi Kenny,

I am fine with you publishing your dissertation. Best of luck.

Thanks,

Jay

On Tue, Oct 13, 2015 at 12:02 PM, Kenny S Kim <cycle87@gmail.com> wrote:

Hi Jay, and Nupur,

I am submitting my dissertation to Grad. Office, and it requires your permission for me to publish the dissertation. Please let me know if it's ok with you. I will just need your email response attached to the end of my dissertation as an appendix.

Thank you.

Kenny